

"APPLICATION OF MULTIOBJECTIVE OPTIMIZATION TO DETERMINING AN  
OPTIMAL LEFT VENTRICULAR ASSIST DEVICE (LVAD) PUMP SPEED"

by

Douglas C. McConahy

BS, Pennsylvania State University, 2005

Submitted to the Graduate Faculty of  
The School of Engineering in partial fulfillment  
of the requirements for the degree of  
Master of Science in Electrical Engineering

University of Pittsburgh

2007

UNIVERSITY OF PITTSBURGH

SCHOOL OF ENGINEERING

This thesis was presented

by

Douglas C. McConahy

It was defended on

May 16, 2007

and approved by

Ching-Chung Li, Ph.D., Professor

Zhi-Hong Mao, Ph.D., Assistant Professor

Thesis Advisor: J. Robert Boston, Ph.D., Associate Chairman

## "APPLICATION OF MULTIOBJECTIVE OPTIMIZATION TO DETERMINING AN OPTIMAL LEFT VENTRICULAR ASSIST DEVICE (LVAD) PUMP SPEED"

Douglas C. McConahy, M.S.

University of Pittsburgh, 2007

A Left Ventricular Assist Device (LVAD) is a mechanical pump used to assist the weakened left ventricle to pump blood to the entire body. One method of controlling pump speed is using a closed-loop controller that changes the pump speed based on the patient's level of activity and demand for cardiac output. An important aspect of the development of a closed-loop controller is the selection of the desired pump speed. Pump speed must be chosen such that the patient receives adequate cardiac output for his/her level of activity. The pump must also operate in a safe physiological operating region, placing constraints on other hemodynamic parameters.

This work presents the pump speed selection problem as a multiobjective optimization problem, considering constraints on cardiac output, left atrial pressure, and arterial pressure. A penalty function is assigned to each hemodynamic variable and a mathematical model of the LVAD and cardiovascular system is used to map the penalty functions as functions of the hemodynamic parameters to penalty functions as functions of pump speed. The penalties for the different variables are combined by forming a weighted sum, and the best set of pump speeds is determined by minimizing the combined penalty functions using different sets of weights. The resulting set of best pump speeds forms the noninferior set (Zadeh, *IEEE Trans. On Auto. Control*, 1967). It was discovered that the noninferior set contains discontinuities, so the concept of a modified noninferior set known as the Clinician's noninferior set is introduced.

A decision support system (DSS) is presented that allows clinicians to determine a single pump speed from the noninferior set by investigating the effects of different speeds on the hemodynamic variables. The DSS is also a tool that can be utilized to help clinicians develop a better understanding of how to assign weights to the different hemodynamic variables.

## TABLE OF CONTENTS

PREFACE.....	x
1.0 INTRODUCTION.....	1
2.0 BACKGROUND.....	4
2.1 ANATOMY OF THE HEART.....	4
2.2 THE CARDIAC CYCLE.....	8
2.3 PROPERTIES OF BLOOD VESSELS.....	12
2.4 MODELS OF THE CARDIOVASCULAR SYSTEM.....	14
2.5 TYPES OF VENTRICULAR ASSIST DEVICES.....	22
2.6 CONTROL OF A VENTRICULAR ASSIST DEVICE.....	26
2.7 SPEED SELECTION OF LVAD.....	30
3.0 MULTIOBJECTIVE OPTIMIZATION.....	38
3.1 NONINFERIOR SET THEORY.....	39
3.2 INVESTIGATION OF PENALTY FUNCTIONS.....	40
3.2.1 Introduction to the NIS.....	41
3.2.2 Simulations of convex penalty functions.....	44
3.2.3 Simulations with a non-convex penalty function.....	49
4.0 RESULTS OF APPLICATION TO PUMP SPEED SELECTION.....	53
4.1 PENALTY FUNCTION ACQUISITION.....	53
4.2 NONINFERIOR SET.....	60
4.3 EFFECTS OF SHIFTING PENALTY FUNCTIONS.....	66
5.0 CLINICIAN DECISION SUPPORT SYSTEM.....	69
6.0 DISCUSSION.....	74
6.1 PENALTY FUNCTION AND NIS SIMULATIONS.....	74
6.2 HEMODYNAMIC AND $J(\omega)$ PENALTY FUNCTIONS.....	75

6.3 NONINFERIOR SET.....	76
6.4 CLINICIAN DECISION SUPPORT SYSTEM.....	78
6.5 SUMMARY.....	79
APPENDIX A: EFFECTS OF NON-CONVEXITIES ON NIS.....	81
APPENDIX B: ANALYTICAL HIERARCHY PROCESS (AHP).....	83
B.1 OVERVIEW OF AHP.....	83
B.2 RESULTS OF AHP.....	88
B.3 DISCUSSION OF AHP RESULTS.....	92
BIBLIOGRAPHY.....	93

## LIST OF TABLES

Table 1: Parameter and variable names for model in Fig. 9.....	18
Table 2: Diode configuration for cardiac cycle phases.....	19
Table 3: Assist device model parameters for Fig. 13 model.....	21
Table 4: Equations and measurements to determine model parameters [8].....	32
Table 5: Comparison of different suction indices [3].....	35
Table 6: Ranges of $\mu_{CO}$ tested and their respective step sizes.....	64
Table 7: Speed range alternatives.....	83
Table 8: Ranking system used in pairwise comparison matrices [31].....	84
Table 9: Values of RI for a given n [31, 32].....	87
Table 10: Data used to create pairwise comparison matrices.....	89
Table 11: Hemodynamic variable comparison matrix.....	89
Table 12: CO comparison matrix.....	90
Table 13: AP comparison matrix.....	90
Table 14: CR for each pairwise comparison matrix.....	91
Table 15: CRs for using linear AP penalty function.....	92

## LIST OF FIGURES

Figure 1: Diagram of the heart [31].....	5
Figure 2: Diagram of systemic and pulmonary circulation systems [2].....	7
Figure 3: Pulsatile waveforms of the heart [4].....	8
Figure 4: Changes in volume and pressure in a complete cardiac cycle [6].....	9
Figure 5: PV loop for left ventricle [7].....	11
Figure 6: Electric analog for blood flow.....	13
Figure 7: Arbitrary blood vessel.....	13
Figure 8: Diode model of the heart valves.....	16
Figure 9: Three (a), four (b), and five (c) element windkessel models [12, 17].....	16
Figure 10: Windkessel model using a pressure-dependent capacitor [14].....	17
Figure 11: Model of cardiovascular system [4].....	18
Figure 12: McInnis model of heart, including assist device [15].....	20
Figure 13: University of Pittsburgh Model include assist device [28].....	21
Figure 14: Diagram of different VADs.....	23
Figure 15: EVAD mechanism diagram [19].....	24
Figure 16: Four brands of centrifugal pumps [19] .....	25
Figure 17: Implanted Nimbus/Pitt device [3].....	25
Figure 18: Nimbus/Pitt axial flow pump [19].....	25
Figure 19: Axial flow pump waveforms in calf. C indicates suction [3].....	27
Figure 20: Block diagram for TAH controller [20].....	28
Figure 21: Pump flow (top) and inflow pressure (bottom) at varying speeds [21].....	29
Figure 22: Block diagram for suction detector controller [21].....	29

Figure 23: Cardiovascular system model including pump [23].....	30
Figure 24: Model of LVAS pump [23].....	31
Figure 25: Estimation algorithm presented by Yu [23].....	31
Figure 26: Control model using a supervisor [3].....	33
Figure 27: Extended certainty-weighted decision system block diagram [27].....	36
Figure 28: Normal (gray) and unsafe (outside gray) physiologic operating regions.....	37
Figure 29: Illustration of inferior and noninferior points.....	42
Figure 30: a) Penalty functions and combined penalty function, $\mu_1 = 0.6$ .....	43
Figure 31: All $NIS_{\mu_3}$ using penalty functions in eqns. 11-13, $a = 8$ .....	46
Figure 32: All $NIS_{\mu_3}$ using penalty functions in eqns. 11-13, $a = 4$ .....	47
Figure 33: All $NIS_{\mu_3}$ using penalty functions in eqns. 11-13, $a = 1.75$ .....	48
Figure 34: All $NIS_{\mu_3}$ using penalty functions in eqns. 11-13, $a = 3$ .....	49
Figure 35: All $NIS_{\mu_3}$ using penalty functions in eqns 11, 12, and 14.....	51
Figure 36: One continuous, non-convex penalty function .....	52
Figure 37: Hemodynamic penalty functions [3].....	54
Figure 38: Process to obtain penalty functions as functions of speed.....	55
Figure 39: Speed input used to determine speed penalty functions .....	56
Figure 40: Hemodynamic data before sorting and smoothing.....	57
Figure 41: Hemodynamic data after sorting and smoothing.....	58
Figure 42: Penalty for each hemodynamic variable with respect to speed.....	58
Figure 43: Penalty for LAP at varying speeds.....	59
Figure 44: Penalty functions resulting from polynomial fit.....	60
Figure 45: Penalty functions and NIS .....	62
Figure 46: Regions of interest for discontinuity test.....	63
Figure 47: Combined penalty functions before and after $NIS_0$ speed jump.....	65
Figure 48: Example of finite size of speed values for $NIS_{0.2}$ .....	66
Figure 49: Penalty functions, $CO = 13L/min$ , $AP = 115mmHg$ , and $LAP = 7mmHg$ .....	67
Figure 50: Original (top) and shifted (bottom) speed penalty functions and CNIS.....	68
Figure 51: GUI upon startup.....	70
Figure 52: GUI after changing set points and plotting penalty functions.....	71
Figure 53: GUI example from Fig. 52 after selecting a speed and choosing weights.....	73



Figure 54: NIS of pump speeds using unsmooth penalty functions .....80  
Figure 55: Example of a hierarchy with n criteria and m decision alternatives.....83

## ACKNOWLEDGEMENTS

I would like to thank Dr. Boston for his assistance and insightful input throughout the course of my graduate career, and Dr. Antaki for his helpful input regarding medical aspects of the project. I was also very fortunate to have the opportunity to work with Antonio Ferreira, who was always available to provide assistance.

Most importantly I want to thank my parents and friends for their unending support, encouragement, and prayers. This work could not have happened without them.

## 1.0 INTRODUCTION

According to the National Kidney Foundation approximately 40,000 people under the age of 65 could benefit from a heart transplant, with 3,591 people in 2003 on the waiting list for a transplant [38]. Many people die each year waiting for a transplant due to a lack of available heart donors. If pharmacological treatments are unsuccessful, an alternative means of assisting the patient is a mechanical assist device [3]. A specific type of mechanical assist device, a left ventricular assist device (LVAD), is used to assist a weakened left ventricle by providing adequate cardiac output. The primary purpose of the device is to improve the quality of life of the patient by providing him/her with the assistance to return to a normal lifestyle.

LVADs are usually used in critical care settings, but devices have been developed that allow the patient to leave the hospital with the implanted LVAD. In the critical care setting, patients are in the immediate care of a physician and the device can be adjusted to provide more or less cardiac output depending on the status of the patient. When the patient leaves the critical care setting a clinician is no longer readily available, and the device must provide adequate cardiac output to sustain the patient's level of activity without clinical supervision. However, as the patient recovers and his/her level of activity increases, the body's demand for cardiac output increases and a change in device settings may be required.

A solution to this problem is an LVAD that utilizes a closed-loop control scheme to make adjustments based on the patient's level of activity. The controller should monitor the patient's demand for cardiac output as well as monitor the device's status to determine the best operating speed for the LVAD's pump. Care must be taken to ensure that the speed is not set too fast or too slow. A speed that is too fast can create negative pressure in the ventricle, a condition known as suction. Suction is a condition where the pump tries to draw more blood than is available in the

ventricle, causing the ventricle wall to be forced against the cannulae attached to the ventricle. This condition can be damaging to the heart. If the speed is too slow blood may flow back into the pump.

Cardiac output can be increased by increasing pump speed. However, the suction condition presents an upper limit on pump speed. A solution to maximize cardiac output while operating the pump at a safe speed is to operate the pump at a speed just below suction [3]. The drawback to this solution is that a pump speed that does not cause suction may still have adverse effects on other physiological parameters. Therefore avoiding suction is not the only constraint when determining an optimal pump speed.

The potential negative effect on other hemodynamic variables is the motivation for formulating the pump speed selection problem as a multiobjective optimization problem. The goal of this work is to provide a method that determines an optimal pump speed that meets constraints placed on cardiac output, arterial pressure, and left atrial pressure.

The constraints were placed on the hemodynamic variables using penalty functions created through the assistance of a team of physicians at the University of Pittsburgh [3]. Using the penalty functions, the noninferior set (NIS) [30] of pump speeds was determined that maintains a safe physiological operating point while providing adequate cardiac output for the patient to maintain his/her current level of activity.

The NIS is not a complete solution to the problem; it presents the best set of pump speeds. The NIS provides clinicians with a starting point for selecting a pump speed but does not indicate the specific pump speed to choose. At this point, the clinician is required to provide more information regarding the importance of each of the constraints.

One approach investigated to choose the optimal pump speed is the Analytical Hierarchy Process (AHP). The original hemodynamic penalty functions were used as an “expert” to set up a series of comparison matrices that considers the trade-offs (penalties) of the three hemodynamic variables and different speed ranges. It was determined that AHP is not a suitable process for this particular problem due to inconsistency issues with the comparisons. Evidence is presented that these inconsistencies are caused by convexity of the penalty functions. A review of the AHP procedure along with the results of its application is in the Appendix.

As an alternative to help the clinician select a specific speed, a computer simulation was developed that allows exploration of the effects of using different speeds in the NIS. The software is presented to the clinician as a GUI, allowing the clinician to alter the penalty functions and observe the effects a pump speed has on the three constraints.

This thesis is organized in the following manner. In Chapter Two a review of necessary cardiovascular system and hemodynamic concepts is provided. Chapter Two also covers models of the cardiovascular system and LVAD along with different types of LVADs and control schemes. Chapter Three presents the multiobjective optimization theory, followed by simulation results that investigated the theory. Chapter Four explains acquisition of the necessary penalty functions and the NIS. Chapter Five describes the use of the clinician software package and its operation.

## **2.0 BACKGROUND**

When the heart is weakened through disease, it may no longer be strong enough to pump blood through the entire body. Pharmacological treatments are available, but success is not guaranteed. Another option for the patient is to get a heart transplant, but the patient may have to wait for an extended period of time before a suitable donor heart is found. An alternative option is a Left Ventricular Assist Device (LVAD), which is surgically attached to the heart to assist in pumping blood through the body. Before discussing design considerations of an LVAD, an understanding of several aspects of the heart's anatomy and physiology is required. Cardiovascular system models will also be presented, along with a review of actual LVADs and issues regarding closed-loop control.

### **2.1 ANATOMY OF THE HEART**

The main function of the cardiovascular system is to transport nutrients and oxygen to the entire body. The heart can be thought of as two pumps in series that send a fluid through a series of tubes that eventually return to the pump. One pump sends the blood to the lungs to pick up oxygen in the lungs, and the other sends the blood through the rest of the body. Eventually the blood returns to the heart and the process is repeated.

Each “pump” in the heart is made up of two chambers; an atrium and a ventricle, giving the heart a total of four chambers. The atria are the smallest of the four chambers. Due to their small size they provide a small contribution to blood circulation. Their primary purpose is to receive blood returning from the circulation and pass it to the ventricles. The ventricles make up most of the heart's volume, with the left ventricle being the larger of the two. The ventricles

receive blood from the atria and pump it through arteries to the rest of the body [1]. The four heart chambers can be seen in Fig. 1 [1]. The two atria are the top chambers, and the ventricles are on the bottom.

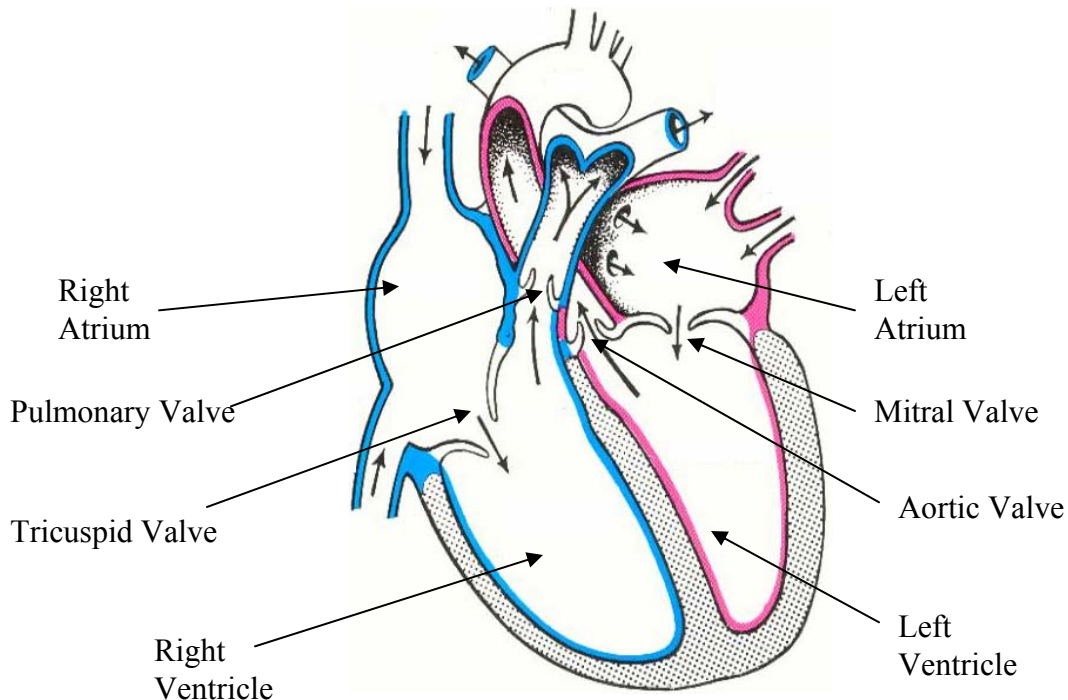


**Figure 1: Diagram of the heart [1]**

The heart uses a series of valves to ensure that blood flows in one direction into and out of the heart. Heart valves are made of tough, flexible tissue that is oriented in such a way that blood can only go through the valve in one direction. Blood flows in the direction of the arrows in Fig. 1 [1]. A valve only opens when the blood exerts enough pressure on it, forcing it open for blood to flow through. When this pressure drops, the valve returns to its originally closed position, preventing blood from flowing in the wrong direction. A pressure gradient is developed as blood flows through the body, and blood only flows from a high pressure to a lower one.

Like the heart chambers there are four heart valves, seen in the diagram in Fig. 1 [1]: two atrioventricular (AV) valves and two semilunar valves. An AV valve is located between each atrium and ventricle, with the tricuspid valve on the right and the mitral valve on the left. The

valve opens when the atrial pressure is greater than ventricular pressure. When ventricular pressure exceeds atrial pressure, the valve closes again. The area of the valve cusps are about twice that of the passageway they cover, creating a large overlap of the cusps when they close [5]. This overlap helps to prevent the backflow of blood into the atrium.

A semilunar valve is located between the right ventricle and pulmonary artery (pulmonary valve) and the left ventricle and aorta (aortic valve). Similar to the AV valves, when left or right ventricular pressure exceeds aortic or pulmonary artery pressure, the valve opens. When ventricular pressure decreases, the three cusps of the valves close, preventing blood from flowing back into the ventricle.

The heart has two atria and two ventricles because there are two different blood circulation paths. The circulation path controlled by the right side of the heart is a low-pressure system known as the pulmonary circulation. Oxygen depleted blood enters the right atrium through the venae cavae and is pumped to the lungs by the right ventricle through the pulmonary artery. The blood receives oxygen in the lungs and is sent back to the left side of the heart through the pulmonary veins. The blood travels only a short distance in this system. Therefore a high pressure is unnecessary.

After the blood picks up oxygen in the lungs it returns to the heart through the left atrium. The left ventricle pumps the oxygen-rich blood through the aorta to the rest of the body. The blood returns to the right atrium depleted of oxygen, completing the cycle. This circulation path is known as the systemic circulation [1]. Due to the large distance the blood travels, this is a high-pressure system. Upon entering the right atrium, the blood repeats the two circulatory paths.

The blood path through the heart and both circulation systems can be seen in Fig. 2 [2]. The upper portion of Fig. 2 (blood flowing to and from the lungs) is the pulmonary circulation, while the lower portion (blood flowing to and from the entire body) is the systemic circulation. Blood on the right side of the figure (pumped by left ventricle) is oxygen rich while the blood on the left (pumped by right ventricle) is oxygen-depleted. As the blood flows farther from the body, oxygen is lost. After exchanging oxygen through the body, the blood returns to the heart through the right atrium. At this point the blood will repeat the circulation path.



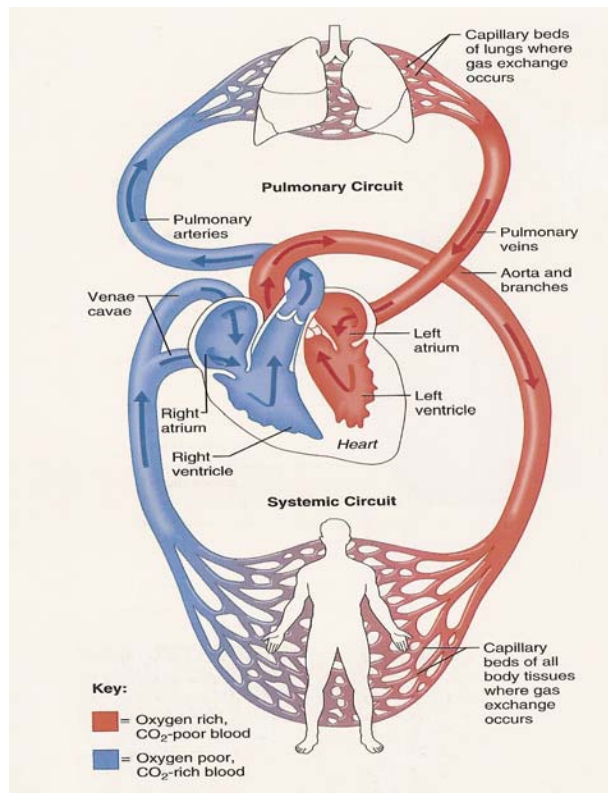


**Figure 2: Diagram of systemic and pulmonary circulation systems [2]**

Due to the different circulation paths, each side of the heart has a different workload. The systemic circulation is much longer than the pulmonary circulation and encounters five times more friction [1]. To handle the longer path, the left ventricle is larger than the right, giving it the strength to pump blood at a higher pressure. The pulmonary circulation only has to pump blood to the lungs, so the larger ventricle is unnecessary. Also, the pressure in the lungs must be lower to avoid damaging the alveoli, which are small air sacks with thin walls that exchange gas in the lungs. Systemic blood pressure is higher than the pressure in the pulmonary system to handle the longer circulation path. Pressure in the aorta is the point of highest blood pressure, while the lowest blood pressure is in the vena cavae.

Blood pressure in the systemic circulation is pulsatile due to contraction and relaxation of the heart. Pulsatility can be seen in the pressure and flow waveforms in Fig. 3 [4].

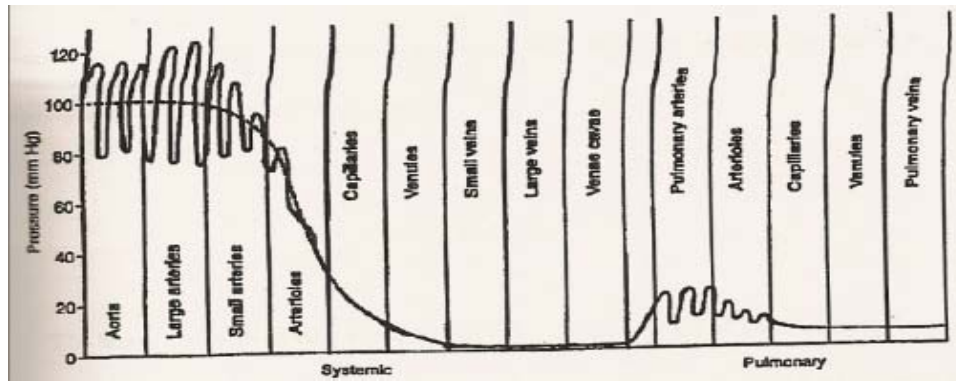
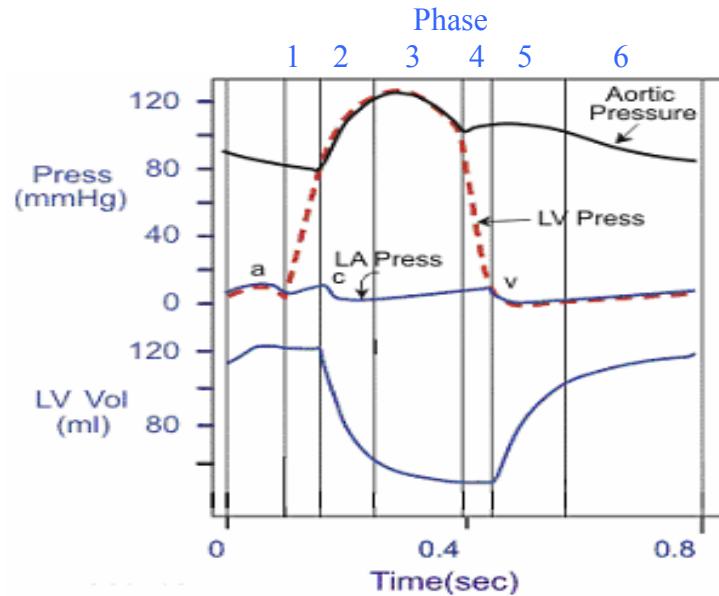


Figure 3: Pulsatile waveforms of the heart [4]

Aortic pressure also fluctuates when the heart beats. The aorta stretches as the ventricles pump blood into the aorta and the increased volume increases aortic pressure. Eventually the ventricle is emptied and the aorta contracts, causing a decrease in pressure. When ventricular pressure is lower than aortic pressure, the semilunar valve closes and the walls of the aorta constrict. The constricting action allows the aorta to maintain its pressure with the blood volume decreasing [1]. As the blood continues through the body, the mean pressure and pulsatility decrease due to a low pass filtering effect caused by the compliance of the arteries [4].

## 2.2 THE CARDIAC CYCLE

Pulsatility in the heart is caused by periodic contraction and relaxation, known as the cardiac cycle. The two main phases of the cardiac cycle are systole, or ventricular contraction (ejection) and diastole, or ventricular relaxation (filling). The entire cardiac cycle lasts approximately 800ms. Waveforms of Left Ventricular Pressure (LVP), Aortic Pressure (AoP), Left Atrial Pressure (LAP), and Left Ventricular Volume (LVV) are shown in Fig. 4 [6].



**Figure 4: Changes in volume and pressure in a complete cardiac cycle [6]**

The cardiac cycle begins with the systole stage, which is made up of three phases: isovolumic contraction, rapid ejection, and reduced ejection. In the isovolumic contraction phase, phase one in Fig. 4, all heart valves are closed. Ventricular pressure sees its largest increases, having a maximal positive slope. But ventricular pressure does not exceed the pressure in the aorta and pulmonary artery, so the semilunar valves remain closed. LVP is less than AoP, causing the aortic valve to also remain closed.

As ventricular pressure rapidly increases in the isovolumic contraction phase, it eventually exceeds the pressure in the aorta and pulmonary artery, forcing the semilunar valves open. This point marks the beginning of the next phase of the cardiac cycle, rapid ejection, indicated by phase two on Fig. 4. During this phase blood flows from the ventricles into the aorta and pulmonary artery. Blood flow is fastest in this phase, as indicated by the steep drop in left ventricular volume in Fig. 4. Also in this phase LVP and AoP reach their maximum values, with LVP always being slightly larger than AoP. There is a decrease in left atrial pressure (LAP) due to expanding of the atria. While the blood exits the ventricle, blood is entering the atria through the veins [5].

As the blood in the aorta and pulmonary artery begins to flow into peripheral arteries to the body and lungs, the heart enters the next phase of the cardiac cycle, reduced ejection,

indicated by phase three on Fig. 4. LVP and AoP increase to their maximum values then begin to decrease. The blood flow into peripheral arteries eventually exceeds the blood flow coming from the ventricles, which causes the decrease in AoP that begins to occur towards the end of the phase. The decreasing LVV causes the LVP to decrease. Notice in Fig. 4 that as AoP and LVP decrease through the reduced ejection phase, AoP becomes larger than LVP. The aortic valve remains open due to kinetic energy of the blood [6]. Also during this phase, atrial pressure is increasing (see LAP in Fig. 4) due to blood returning from the body and lungs.

At the end of ventricular systole (the reduced ejection phase), blood flow continues due to kinetic energy. When the energy of the blood in the ventricles is lower than that of the blood flowing through the aorta and pulmonary artery, the semilunar valves close due to the decreased ventricular pressure. Upon closure of the semilunar valve ventricular diastole begins. This stage is also made up of three phases: isovolumic relaxation, rapid filling, and reduced filling. During the isovolumic relaxation phase, phase four in Fig. 4, the pressure in the aorta and pulmonary artery exceed the pressure in the ventricles, causing both semilunar valves to close. However, the AV valves remain closed, causing a drop in ventricular pressure without changing the volume, which is shown in Fig. 4. Also notice in Fig. 4 that at the onset of isovolumic relaxation there is a jump in aortic pressure. This jump in aortic pressure indicates the time that the aortic valve closes.

Eventually ventricular pressure drops below atrial pressure, forcing the AV valves open. This phase of diastole is known as the rapid filling phase and is indicated by phase five on Fig. 4. Figure 4 shows that at the beginning of rapid filling, the contraction of the atria cause their pressure to increase, and consequently LVP begins to drop below LAP, forcing the mitral valve open. At the same time, LVV experiences its most abrupt increase due to the atria forcing blood into the ventricles, indicating that most ventricular filling occurs during this phase.

As the ventricle fills and expands its pressure rises. The increase in ventricular pressure causes the difference in pressure between the atria and ventricles to be smaller, reducing the rate of filling. The reduced filling phase is indicated by phase six on Fig. 4 [6].

Changes in LVP and LVV are generally summarized using the pressure-volume (PV) loop seen in Fig. 5 [7]. LVV is plotted on the x-axis against LVP. Point A on Fig. 5 corresponds to the onset of diastole. The ventricle fills from A to B. At point B, the mitral valve closes, and from point B to C the heart is in the isovolumic contraction phase. At point C, the aortic valve

opens, and the ventricle ejects blood into the aorta. This decrease in LVV is seen from points C to D, indicating the rapid ejection phase. The volume decreases at a lower rate from points D to E for the reduced ejection phase. At point E, the aortic valve closes, and the heart enters the isovolumic relaxation phase, completing the cardiac cycle.

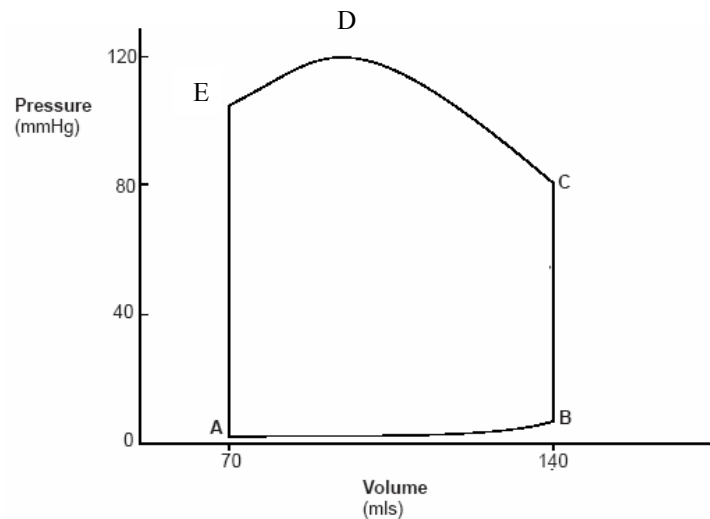


**Figure 5: PV loop for left ventricle [7]**

One of the main goals of an LVAD is to help the weakened heart provide Cardiac Output (CO). CO is defined as the blood pumped by each ventricle in one minute. The CO of the body depends on the patient's level of activity, emotion, and various physiological factors [3]. Providing adequate CO is the motivation behind designing improved LVADs. The volume of blood pumped by each ventricle in one heartbeat is the Stroke Volume (SV). CO is related to SV and heart rate (HR) by the Eq

$$CO = HR \times SV \quad (1)$$

The CO of the heart is related to preload, the venous blood returning to the heart. The volume of blood pumped out of the heart is directly related to the volume of blood returning to the heart, or the preload. This concept is known as the Frank-Starling law. The afterload of the

heart is the pressure that the ventricle must overcome to pump blood [1] and can be thought of as the load the heart see as it pumps blood through the body. If afterload is increased, the heart must produce higher pressure and less stroke volume, keeping the area of the PV loop constant [3]. The area of a PV loop is also the work per beat of the heart, so a constant area results in constant work. Contractility, a measure of the strength of the heart's contraction, is another factor affecting the heart's response to changes in CO. An increase in contractility allows the heart to pump more blood.

### **2.3 PROPERTIES OF BLOOD VESSELS**

Blood does not flow through the body unopposed; several forces act on the blood to hinder its flow. Resistance, the opposition to the blood flow, is the frictional force that acts on the blood as it flows through the body. One source of friction in blood flow is the force between the blood and blood vessel walls. Longer blood vessels increase friction due to the increased exposure of blood to vessel walls. The systemic circulation system produces more resistance than the pulmonary circulation because of its length. Another source of resistance is viscosity, which is the internal resistance to flow in liquid. This is caused by a velocity gradient across the blood vessels. Diameter of the blood vessel has a similar effect on resistance. As the diameter decreases, more blood will be in contact with its walls, increasing resistance. The arterioles, the system of arteries farthest from the heart, are the smallest vessels, and consequently have the highest resistance and a larger cross-sectional velocity gradient.

The flow of blood through the body is analogous to an electric circuit. Consider the resistor in Fig. 6, with current  $i_r$  and voltage drop  $V_r$ . It is commonly known that Ohm's Law,  $V = iR$ , describes the behavior of this resistor. As the resistance increases, the voltage drop increases and current decreases, and vice-versa. As current flows through the resistor, voltage is dropped across the resistor, and current flows from a higher to lower voltage. Just like voltage is a potential to create current flow, blood pressure is a potential to create blood flow.

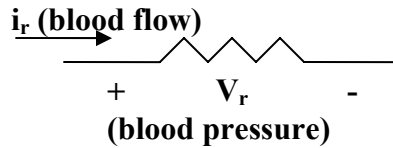


**Figure 6: Electric analog for blood flow**

Similarly, blood flow through a given blood vessel is governed by

$$Q = \frac{\Delta P}{R} \quad (2)$$

where  $Q$  is flow,  $\Delta P$  is the pressure difference from one end of the vessel to the other, and  $R$  is the vessel resistance. This equation is analogous to solving Ohm's Law for current ( $i = V/R$ ). Consider the arbitrary blood vessel in Fig. 7, with blood flow  $Q$ , vessel resistance  $R$ , and pressure gradient  $\Delta P = P_1 - P_2$ . As the resistance of the blood vessel is increased, the pressure required to force blood through the vessel increases, and the flow decreases, and vice-versa. As previously discussed, blood must flow in the direction of a higher to lower pressure, creating a pressure gradient.

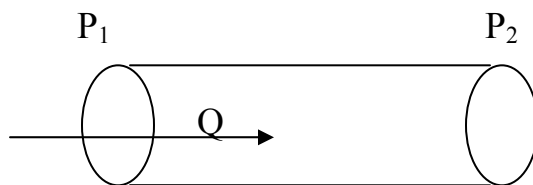


**Figure 7: Arbitrary blood vessel**

Another property of blood vessels modeled by an electric analog is compliance. Compliance is the ability of the blood vessel to stretch or distort to accommodate volume at a given pressure and is modeled by a capacitor. Consider a compliant blood vessel with a pressure difference  $p$  between two points. The volume of the vessel can be found by

$$v = Cp \quad (3)$$

where  $v$  is the volume and  $C$  is the compliance of the vessel. Blood flow  $Q$  is the derivative of volume, so differentiation of Eq 3 results in

$$Q = C \dot{p} \quad (4)$$

Equation 4 is analogous to the equation for current through a capacitor,  $i = C \frac{dv}{dt}$  [4].

## 2.4 MODELS OF THE CARDIOVASCULAR SYSTEM

Developing accurate models of the heart and circulatory system is of interest to both clinicians and engineers. Such a model allows clinicians to study the contributions of different cardiovascular properties to the heart's behavior and how changes in these properties affect hemodynamic variables such as blood pressure and flow. This is especially helpful in studying parameters that are difficult to measure or must be measured using invasive methods, such as aortic or arterial compliance.

An accurate model is also useful in the development of an LVAD control scheme. When the LVAD is implanted in the patient, it is desirable to keep hemodynamic variables such as LAP, Arterial Pressure (AP), and CO within clinician-defined limits [8, 9]. When the pump speed causes the LVAD to operate at a speed outside the clinician-defined limits, the patient may develop other medical problems such as pulmonary edema, hypertension, or suction [5, 8]. A model of the cardiovascular system and LVAD can allow clinicians to determine what speeds can be potentially dangerous to a patient.

The ideal LVAD controller for this project would utilize LAP, AP, and CO as control variables. In an Intensive Care Unit (ICU) where more pressure and flow measurements are available and implementation of this control scheme is simplified. However, as the patient



recovers and eventually leaves the ICU, and returns to their home or an extended care facility, few measurements are available, and among the unavailable measurements are LAP, AP, and CO.

Therefore, to develop a controller based on these variables, a model is needed to estimate the values of LAP, AP, and CO. The model uses information about the patient's heart and cardiovascular system, such as compliances and resistances, to estimate values of LAP, AP, and CO from a given pump speed input.

There are several methods used for modeling the heart and cardiovascular system, such as using a hydraulic filter circuit [10], a systems analysis approach [11], or an analog electric circuit [3, 8, 13-18]. In this work an analog electric circuit model is used, so only these models will be reviewed here.

An analog electric circuit model is composed of basic circuit elements. In general, resistors are used to represent the frictional force opposing blood flow in blood vessels. The inertance of the blood is modeled using an inductor, and the compliance of the heart and blood vessels, or ability to stretch or distort, is modeled using a capacitor [13].

Not all models use only linear elements; some models use diodes, a non-linear circuit element, to model the heart valves [3, 8, 17]. The valves are unidirectional, and only open when the pressure on one side exceeds the pressure on the other, forcing it open. For example, consider the aortic valve. When LVP exceeds AoP, the valve opens; when AoP exceeds LVP, the valve closes.

When modeling the heart valves using an ideal diode model, they are assumed to be totally open or closed, switching instantaneously. When the diode is in the "off" state, cathode voltage is greater than anode voltage. The diode switches to the "on" state when anode voltage exceeds cathode voltage. The voltage across the diode that controls the switching is analogous to the pressure gradient of the heart. The two-diode states, on and off, correspond to an open and closed heart valve, respectively. Similar to the diode model, the heart valve model also includes a series resistance to model the resistance of the heart valves.

An example of a heart valve model is seen in Fig. 8, where  $D_v$  is the valve, and  $R_v$  is the valve resistance.  $P_{v1}$  and  $P_{v2}$  are the pressure on each side of the valve, and  $i_v$  is the blood flow through the valve. When  $P_{v1} > P_{v2}$ ,  $D_v$  opens and blood is allowed to flow through. When the pressure gradient reverses,  $D_v$  closes and no blood flows.

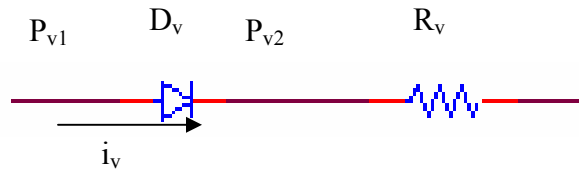


**Figure 8: Diode model of the heart valves**

A model commonly used to describe the circulatory system is the windkessel model [12, 13, 17]. The windkessel can be used to model the load seen by the heart as it pumps blood through the body, as well as pressure and flow in the aorta. The model is typically used to estimate arterial compliance, which is modeled by a capacitor.

Several variations of the windkessel model exist. The  $n$  element windkessel model contains  $n$  R, L, and C elements, where  $n = 2, 3, 4, 5$  [12, 13, 17]. The three, four, and five element windkessel models are seen in Figs. 9 a, b, and c [12, 17]. The windkessel models shown here are not the only available models; variations of the windkessel models exist. For example, Stergiopoulos et al modified the four-element windkessel (9b) by replacing the series combination of  $r$  and  $L$  with a parallel combination [13].

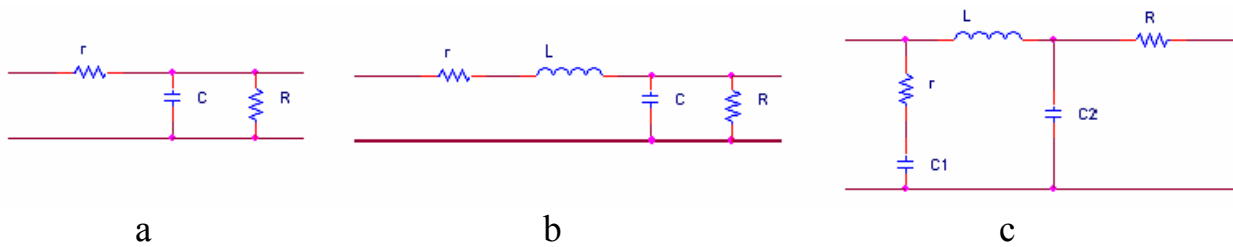


**Figure 9: Three (a), four (b), and five (c) element windkessel models [12, 17]**

In the three-element windkessel of figure 9a, the resistor  $R$  represents the resistance seen by the blood as it travels through the arteries throughout the body, also known as peripheral resistance. The characteristic resistance,  $r$ , is the resistance of the aorta. The capacitor represents the arterial compliance.

The three-element windkessel model sufficiently models the load seen by the heart, but it is not totally complete. The model does not account for aortic characteristic impedance or arterial inertance. To account for this error, an inductor was added to the three element windkessel to model blood inertance [12, 13], creating the four element windkessel in figure 9b. Similarly, a second capacitor was added to the four-element windkessel model to create the five-element windkessel model (figure 9c) [17].

Berger and Li [14] developed variations of the three-element windkessel models by using a time-varying capacitor instead of the constant capacitor. The time-varying capacitor is used to model a pressure-dependent compliance as opposed to the constant compliance of the three-element windkessel model. As blood pressure increases, arterial compliance also increases. It was determined by Berger and Li that compliance increases exponentially with pressure [14]. This model provides more accurate measurements for pressure, but determining the value of the pressure-dependent compliance is difficult; it requires compliance measurements over a range of blood pressures that can be harmful to the patient [4]. A three-element windkessel model with a pressure dependent compliance is shown in Fig. 10 [14]. The parameters  $r$  and  $R$  are the same as the models in Fig. 9, and  $C(P)$  is the pressure dependent compliance.

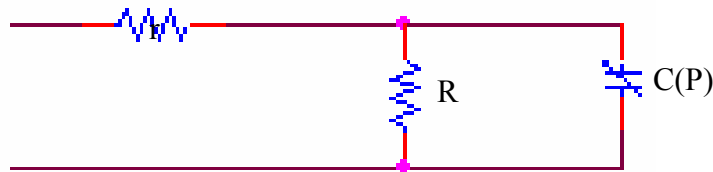


**Figure 10: Windkessel model using a pressure-dependent capacitor [14]**

A model for the cardiovascular system developed at the University of Pittsburgh is presented in Fig. 11 [14]. The two diodes,  $D_m$  and  $D_A$ , represent the mitral and aortic valves, respectively. The node voltages,  $P_r$ ,  $P_v$ ,  $P_s$ , and  $P_A$  represent different pressures in the cardiovascular system, while the currents  $f_A$  and  $f_R$  represent different blood flows.

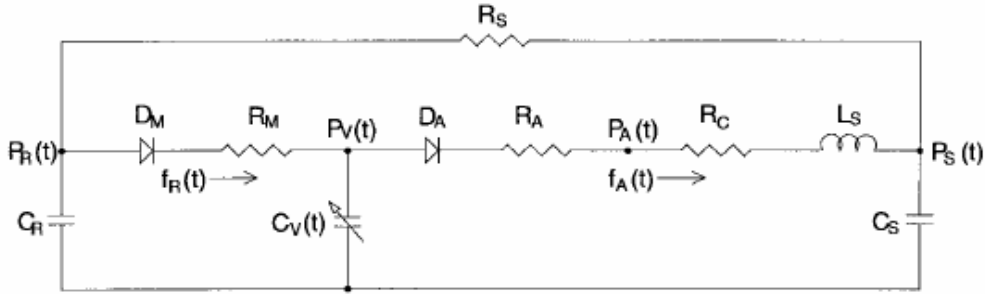


Figure 11: Model of cardiovascular system [4]

The circuit parameters all correspond to a characteristic of the cardiovascular system. If the parameters, such as resistance or compliance, of the patient can be determined, the model can predict the values of pressures and flows. Table 1 lists the names and descriptions for the model elements and variables.

Table 1: Parameter and variable names for model in Fig. 9

Model Element	Physiological Meaning	Variable	Physiological Meaning
$R_s$	Systemic Vascular Resistance	$P_v$	Ventricular Pressure
$D_m$ & $R_m$	Mitral Valve	$f_a$	Aortic Flow
$D_a$ & $R_a$	Aortic Valve	$P_a$	Aortic Pressure
$R_c$	Characteristic Resistance	Pump speed	Peripheral Pressure
$C_r$	Left Atrial Compliance	$f_r$	Venous Return Flow
$C_v(t)$	Left Ventricular Compliance	$P_r$	LAP
$C_s$	Systemic Compliance		
$L_s$	Inertance of Blood in Aorta		

The compliance of the left ventricle changes during the cardiac cycle. Compliance decreases during systole, reaching a minimum at the end of systole. Conversely, compliance

increases during diastole. To model the time-varying compliance, the left ventricle was modeled by the time-varying capacitor  $C_v(t)$  [14].

The mitral and aortic valves can be seen in Fig. 1 [1]. The presence of the heart valves (diodes) makes the heart model in Fig. 11 a non-linear system. The different combinations of on and off states of the diodes model the four phases of the cardiac cycle [4]. Table 2 describes the four phases and their corresponding diode configurations. Also note that the rapid and reduced ejection and filling are not explicitly included, but are generalized into the relaxation and contraction phases.

**Table 2: Diode configuration for cardiac cycle phases**

<b>Phase</b>	<b>D<sub>m</sub></b>	<b>D<sub>A</sub></b>
Ejection	Off	On
Isovolumic Relaxation	Off	Off
Passive filling	On	Off
Isovolumic contraction	Off	Off
Not Possible	On	On

Models including an assist device have also been developed. McInnis et al modeled the ventricles similar to the constant compliance windkessel model with the addition of the voltage source  $U_v$ , which represents the strength of the ventricle [15]. This model was used for each ventricle as well as the assist device. The voltage source  $U_A$  represents the driving force of the assist device, which is operating in parallel with the left ventricle [15]. Like the model in Fig. 10, the diodes and their series resistors are used to represent the inlet and outlet of the aortic, tricuspid, and mitral valves. Fig.12 [15] shows the model of each ventricle plus the assist device.

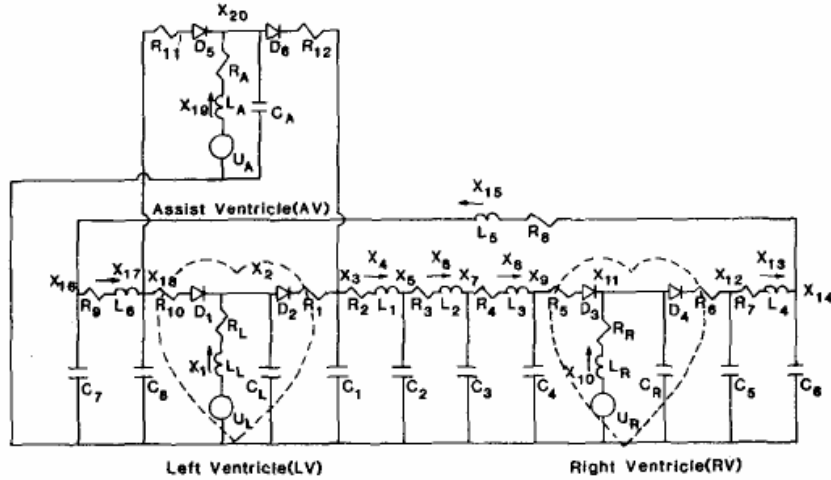


Figure 12: McInnis model of heart, including assist device [15]

A mock circulatory system to test an LVAD was developed based on the model in Fig. 12. McInnis et. al. were able to develop a working adaptive controller using this model [15]. However, a major drawback of this model is the fact that it uses 37 parameters.

The model in Fig. 11 can be modified to include the pump, and is seen in Fig. 13 [30]. Also note that this is the model that will be used in all experiments for the remainder of this work. The input and output cannulae, the suction characteristic resistor  $R_k$ , and the pressure difference between the inlet and outlet cannulae,  $H$ , model the assist device. The parameter  $H$  is not a physical component, but a dynamic model used by Choi to fit measured data [28] and is expressed as

$$H \equiv \beta_0 Q + \beta_1 \frac{dQ}{dt} + \beta_2 \omega^2 \quad (5)$$

where  $Q$  is the blood flow through the pump,  $\omega$  is the pump speed, and  $\beta_i$ ,  $i = 0, 1, 2$  are coefficients determined using a least-squares algorithm. The coefficient values determined by Choi [28] are shown in Table 3, along with the physical meanings and values of the assist device parameters.

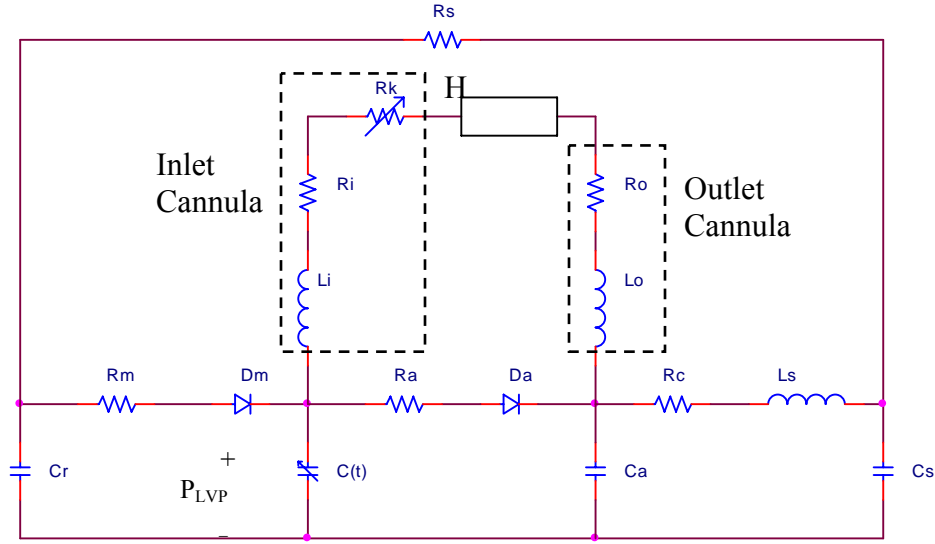


Figure 13: University of Pittsburgh Model include assist device [28]

Table 3: Assist device model parameters for Fig. 13 model

Model Element	Physical Meaning	Parameter value (units)
$R_i$	Cannulae inlet resistance	0.0677 mmHg.sec/ml
$L_i$	Cannulae inlet inertance	0.0127 mmHg.sec <sup>2</sup> /ml
$R_o$	Cannulae outlet resistance	0.0677 mmHg.sec/ml
$L_o$	Cannulae outlet inertance	0.0127 mmHg.sec <sup>2</sup> /ml
$R_k$	Suction characteristic resistor	
H	Pressure difference	
$\beta_0$		0.1707
$\beta_1$		0.02177
$\beta_2$		-0.0000903

The variable resistor  $R_k$  was originally developed by Schima et al [21] to model suction and was adapted by Choi to depend on LVP [28]. The resistance of  $R_k$  is expressed as

$$R_k = \begin{cases} 0, & P_{LVP} > P_{th} \\ -3.5P_{LVP} + 3.5P_{th}, & otherwise \end{cases} \quad (6)$$

where  $P_{LVP}$  is the left ventricular pressure and  $P_{th}$  is a pressure threshold for suction. When LVP is greater than the pressure threshold, suction does not occur, and the resistor has no effect on the model. However, when LVP drops below  $P_{th}$ ,  $R_k$  takes on a value determined by Eq 6 and affects blood flow through the pump [28].

With the exception of the parameters added for the assist device, the parameters for the model in Fig. 13 are the same as those in Fig. 10, and can be found in Table 1. The only other addition to the model is the capacitor  $C_a$ , which is used to model aortic compliance.

## 2.5 TYPES OF VENTRICULAR ASSIST DEVICES

Ventricular Assist Devices (VADs) come in a variety of styles, each with its own advantages and disadvantages. Each VAD has a different method of controlling CO, such as a pusher-plate or balloon, but one thing in common with all of them is the importance of controlling the speed (in the case of the rotary pump) or rate (in the case of a pulsatile pump) of the device. Changing pump speed as physiological demand changes may not be as critical for all of the pumps, but it is necessary to allow the pump to operate without frequent operator interaction.

Ventricular assist devices can be divided into two categories: pulsatile or dynamic pumps. A pulsatile pump operates similar to the natural heart; it produces pulsatile pressure and flows like those found in the natural heart. Conversely, dynamic pumps operate continuously and do not produce pulsatile waveforms like the pulsatile pumps. The diagram in Fig. 14 breaks down the different types of VADs.



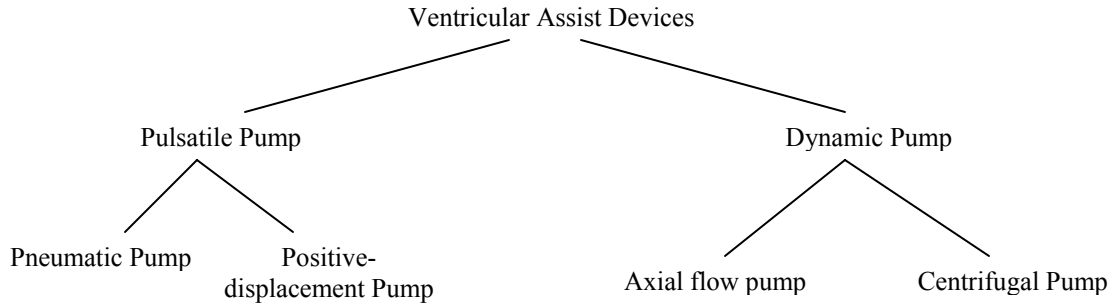


**Figure 14: Diagram of different VADs**

The first generation of pulsatile pumps used air to pump blood. A positive-displacement pump used by 100,000 patients annually is the intra-aortic balloon pump (IABP) [19]. The IABP is less invasive and less complicated than most pumps, but does not provide the level of support of other ventricular assist devices. The IABP works in series with the left ventricle by inserting an elongated balloon below the aortic arch that inflates during diastole and deflates during systole. The inflation during diastole increases ventricular pressure and provides an additional flow of blood to the body by pumping while the ventricle is normally filling [18].

The major goal of the IABP is to increase coronary perfusion and decrease ventricular afterload. Optimizing the device to produce the best results is based on several parameters: position of the balloon in the aorta, volume displacement, geometric size relative to the aorta, and most importantly timing of the inflation and deflation. Welkowitz and Li discuss the need for a closed-loop control scheme to provide dynamic timing adjustments for the balloon [18].

The next generation of pulsatile pumps utilized a positive displacement mechanism. Examples of positive displacement pumps include the Thoratec VAD, the TCI HeartMate LVAD (Thermo Cardiosystems, Inc), and the Penn State University (PSU) Arrow Lionheart-2000 LVAD (Arrow, Inc) [19]. The PSU pump is also referred to as an electric ventricular-assist device (EVAD), because the device utilizes a brushless DC motor to move a pusher plate back and forth. When the plate is pushed forward, it presses against a blood sac that sends blood into the circulatory system. The sac refills when the plate is moving back [20]. Figure 15 [19] presents a diagram of the roller screw and pusher-plate of the EVAD.

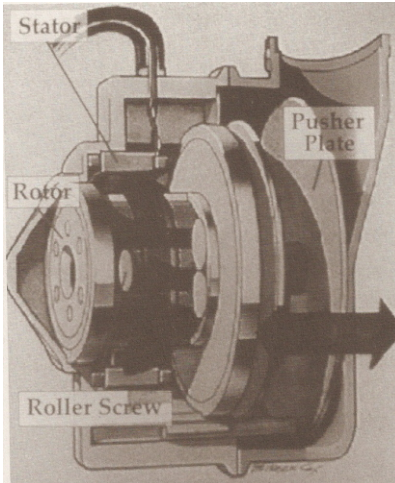


**Figure 15: EVAD mechanism diagram [19]**

The EVAD controller must drive the pusher plate and control the pumping rate. The pumping rate is controlled by the patient's CO demand and end diastolic volume. Motor speed and voltage are used as control signals [19].

An important requirement for the EVAD controller is to minimize electric energy consumption while performing the previously mentioned two tasks. Four sets of gain values, determined such that electric energy consumption is minimized, are used to keep the EVAD operating in the range of 50 – 150 beats per minute (bpm) [20]. The high-energy consumption of this pump is one of its main drawbacks, along with its bulky size and complexity [3].

Dynamic pumps, also referred to as rotary pumps, come in several different styles. One of the most commonly used rotary pumps is the centrifugal or radial-flow pump [19]. Blood enters the pump axially through a tube or pipe and is propelled out of the pump into the body using fast-moving blades or concentric cones. The big advantage to using a centrifugal pump is that it is simple to use and only has one moving part. Figure 16 [19] shows four different brands of centrifugal pumps (A-D): the Sarns, St. Jude Medical Lifestream, Bio-Medicus BIO-PUMP, and Nikkiso centrifugal pumps.

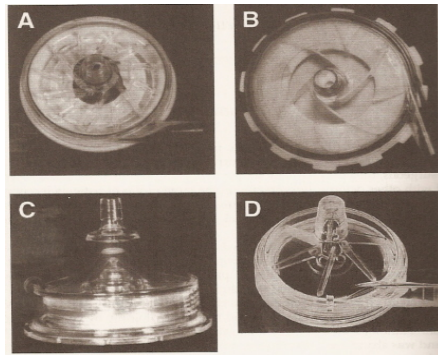


**Figure 16: Four brands of centrifugal pumps [19]**

Similar to the centrifugal pump in its mechanical simplicity is the axial flow pump. For example, the Nimbus/University of Pittsburgh axial flow pump has one moving part, the pump/rotor mechanism [19]. The speed of the pump is adjusted according to the physiological demand of the patient. A sketch of the implanted Nimbus/Pitt axial flow pump is presented in Fig. 17 [3], and the pump itself is shown in Fig. 18 [19].

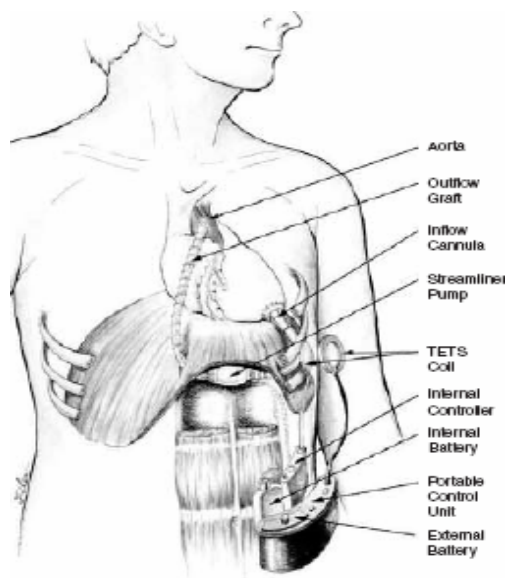


**Figure 17: Implanted Nimbus/Pitt device [3]**

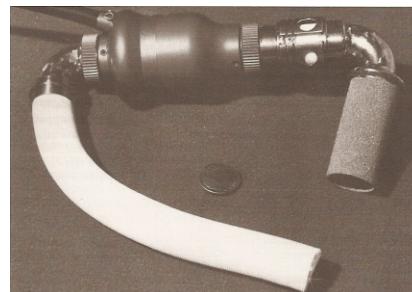


**Figure 18: Nimbus/Pitt axial flow pump [19]**

The simple mechanism of the rotary pumps gives it a large advantage over the bulkier pulsatile pumps. The smaller size makes the rotary pump easier to implant and if needed, remove from the patient. The simple design makes the pump easier to work with, cheaper to build, and more reliable. The increased reliability also makes rotary pumps more suitable for long-term use [19].

The rotary pump is not without its drawbacks. Rotary pumps are sensitive to mismatches between physiological demand and operating settings. They are also sensitive to changes in afterload. Boston et al explain in [3] that operating the pump at the correct speed is more critical in a rotary pump than a pulsatile pump, as explained below. This provides the motivation for developing a controller that can adjust pump speed based on changes in the patient's physiological demand.

## **2.6 CONTROL OF A VENTRICULAR ASSIST DEVICE**

The devices can be controlled with an open or closed loop scheme, or operated at a fixed speed. When the patient is in a critical care setting with more supervision, keeping the patient's CO at a desirable level is easier; a technician can adjust the device as needed, or have a clinician treat the patient if necessary [19]. Control becomes more difficult when the patient leaves the critical care setting and an operator is not available to constantly adjust the device.

A desirable feature of a VAD is to eliminate as much operator intervention as possible; the VAD should adjust itself as the patient changes his/her level of activity. Adaptive control is also necessary to allow the use of physiologically sensitive rotary pumps. The controller should also operate the pump at a speed that maximizes CO, but does not operate at speeds that are too high or low.

The control problem is different for pulsatile and dynamic pumps. Pulsatile pumps fill and eject blood through a valve into the circulatory system. The goal in controlling a pulsatile pump is to determine the volume per cycle or pump rate to control blood pressure [3, 18]. Axial pumps continuously try to draw blood from the ventricle and send it into the circulatory system without using a valve. This continuous operation provides an upper and lower bound on speed.

If the pump operates too slowly, the blood can flow backwards through the pump back into the heart because of the lack of a valve [3]. Pulsatile pumps do not have this problem because they have valves to ensure that blood flows in one direction.

An upper bound on motor speed in axial pumps caused by the pump's continuous operation also exists. If the pump is operating too fast it may try to pump blood that is not in the ventricle. This is a dangerous condition known as suction, and must be avoided; therefore the controller must detect its occurrence and immediately reduce motor speed. To see an example of suction, consider the pump data for a calf with an axial pump at three different speeds is shown in Fig. 19 [3]. Graph a is at 9,000 rpm, b at 10,000, and c at 11,000. As the speed is increased, the pulsatility begins to diminish until it is lost at 11,000 rpm. At 11,000 rpm the calf is in suction; pump flow oscillates randomly around its mean and ventricular pressure is less than zero. Therefore, the goal for controlling an axial pump is to set the motor speed fast enough to avoid backflow and slow enough to avoid suction [3].

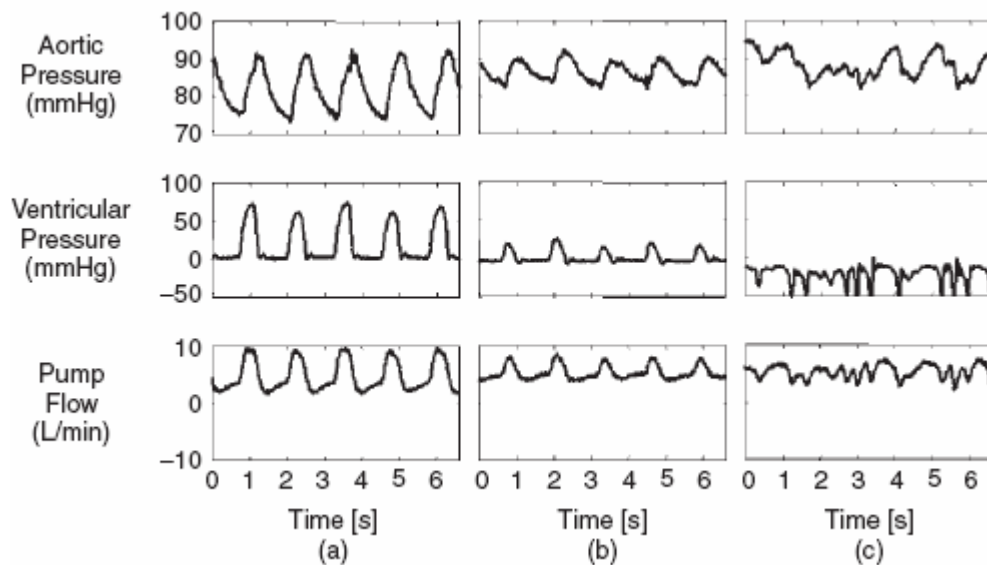


Figure 19: Axial flow pump waveforms in calf. C indicates suction [3].

An open loop control scheme provides a satisfactory performance in critical care settings. While in this setting, the patient is being constantly monitored, and an operator can adjust the VAD as needed. When the patient leaves this setting an adaptive controller is necessary to allow

the patient to live normally without an operator. The controller should recognize changes in CO demand and adjust the pump accordingly. However, it is undesirable to use pressure and flow transducers to monitor changes because of reliability issues [3].

McInnis et al discuss an auto-regressive-moving-average (ARMA) method for control [15]. The goal of this control scheme is to design the controller to imitate the Frank-Starling Law by responding to atrial pressure changes. The controller should cause the device to pump blood that the weakened ventricle cannot. McInnis et al found that when the left ventricle is weakened, as LAP approaches mean systemic pressure, CO drops proportionally. Therefore, the controller should respond to the drop in pressure by increasing CO [15]. The level of atrial pressure indicates the level of output the pump provides. The ARMA method was successfully implemented using a PID controller, and tested in a mock loop. The controlling signal for this system is mean LAP (LAP) because it is a measurable output.

Ahn et al controlled a Total Artificial Heart (TAH) pump using motor current [20]. The motor input current is used because it reflects the afterload and requirement of high pump output. Aortic Pressure (AoP) and pulmonary artery pressure (PAP) were kept within a predefined range by increasing and decreasing pump output. As the motor adjusts its speed to maintain acceptable levels of AoP and PAP, as well as meet demands for varying CO, the current changes, providing a control signal for the system. A block diagram for closed-loop feedback control of the TAH is shown in Fig. 20 [20].

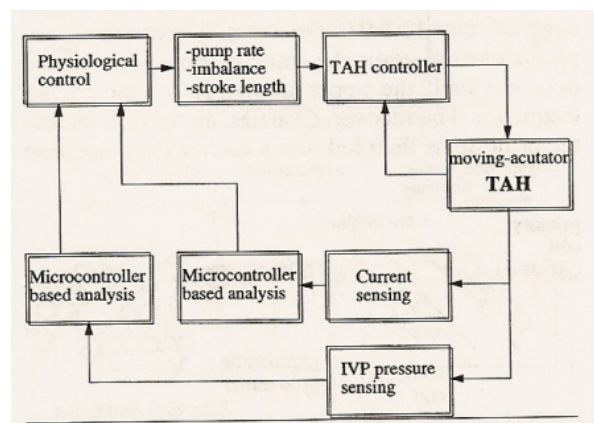


Figure 20: Block diagram for TAH controller [20]

Schima et al propose using suction detection as a parameter for rotary pump control [21]. When suction occurs, the atrium collapses, indicating limited filling of the atrium and low atrial pressure. Fig. 21 [21] shows waveforms for inflow pressure and pump flow gathered from *in vivo* tests. The device speed is initially operating at a safe rate, and is increased to a speed producing suction. The pump flow decreases at the far right of the waveform, indicating suction. This decrease is used as part of the control scheme described below.

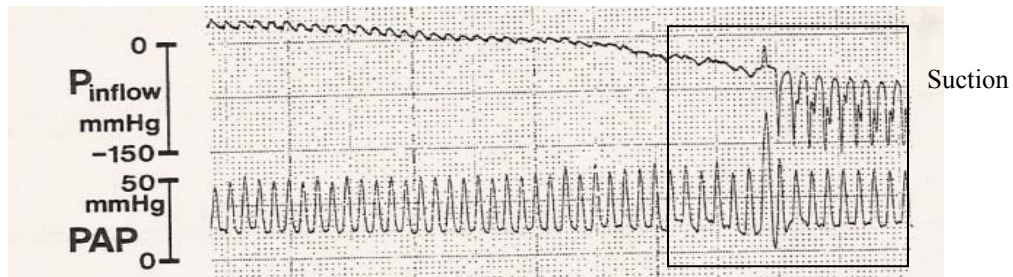


Figure 21: Pump flow (top) and inflow pressure (bottom) for varying pump speeds [21]

A block diagram for this approach is shown in Fig. 22 [21]. The initial pump speed,  $F_{nom}$ , is set by the operator and is the input to the adaptive attenuator. The flow signal is monitored by a peak detector, which watches for steep drops that occur in the flow signal when suction occurs. In this control scheme, the peak detector acts as a suction detector. If the peak detector sees a steep drop in flow, it can reduce the pump speed,  $F_{nom}$ . Schima et al claims that a more advanced controller could increase  $F_{nom}$  to the suction limit. This controller fulfills Starling's law [21].

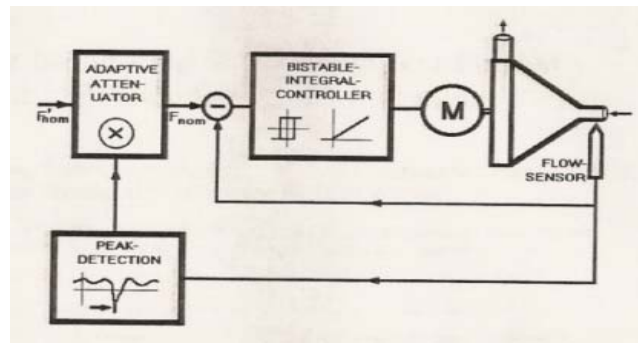


Figure 22: Block diagram for suction detector controller [21]

## 2.7 SPEED SELECTION OF LVAD

In the last section, the problem of controlling the speed of a rotary pump and several possible solutions were discussed, including the usefulness of using a closed-loop controller [3, 15, 20, 21]. Methods were also discussed that do not use pressure transducers [3, 21]. Without transducers, the only data readily available to the device is the pump current, speed, and sometimes flow. For the device to obtain the hemodynamic data required to operate at a desirable speed, the hemodynamic parameters must be estimated from a model.

One approach to this problem presented by Yu et al utilizes the model in Fig. 23 [3], which is the same model in Fig. 11 with the pump model connected in parallel with the aortic valve. Yu proposed using an Extended Kalman Filter (EKF), which is similar to a standard Kalman Filter, but is “extended” for use with nonlinear systems with added white noise. The EKF starts with a guess and updates a linearization around the previous state estimate [22].

The pump described by Yu in this example is the Novacor Left Ventricular Assist System (LVAS), which is a pulsatile pusher-plate pump. A model of the LVAS is shown in Fig. 24 [23]. The model predicts the pump chamber pressure,  $P_{cp}$  at a given instantaneous volume. The time-varying capacitor,  $C_{VAD}(t)$ , represents spring stiffness in the springs coupling the solenoid and pusher-plates in the actual device.

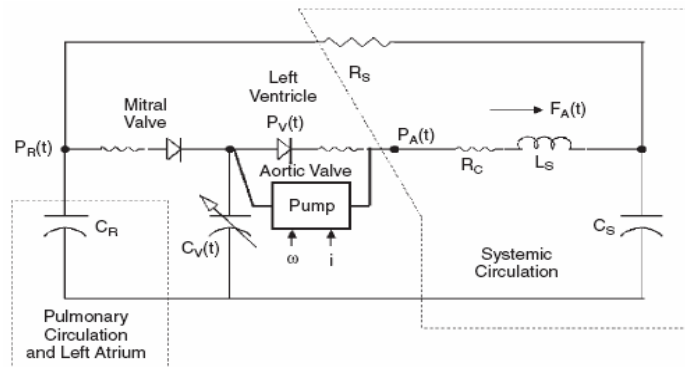


Figure 23: Cardiovascular system model including pump [23]



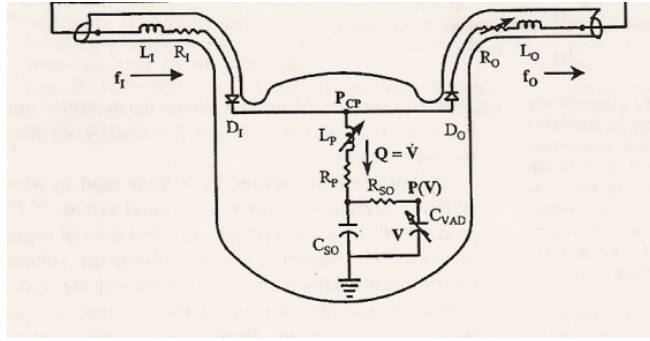


Figure 24: Model of LVAS pump [23]

A block diagram for Yu's estimation algorithm is shown in Fig. 25 [23]. The only input to the estimator is the pump volume,  $V$ . The volume measurement produces a quasistatic pump pressure signal  $P(V)$  that is determined by the pump's operation mode, which can be ejection or filling.  $P(V)$  is used to create an estimate for  $P_{fict}$ , which is the pump pressure ignoring the effects of fluid mechanics. The  $P_{fict}$  signal along with the first and second derivatives of the original volume input is used to compute an estimate for the  $P_{CP}$ .

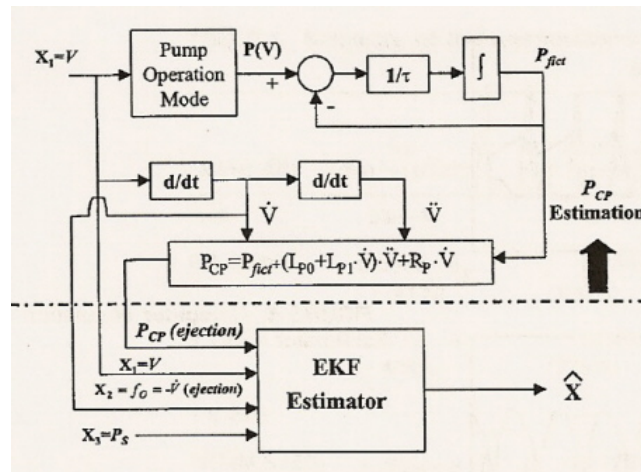


Figure 25: Estimation algorithm presented by Yu [23]

Yu [8] applied the EKF to the model in Fig. 11 [8]. A set of Eqs and parameters required to estimate the model for each stage of heart activity was developed and can be found in Table 4. The required model parameters can be included in the algorithm as state variables and estimated with other variables [8].

The measurement available to determine model parameters changes as the heart fills and ejects. A unique solution to the parameter values is available if they can be measured from the transfer function coefficients of each phase.  $P_A$ ,  $f_A$ , and  $P_R$  are the available measurements during the ejection phase. The names of these variables can be found in Table 1. The minimum measurements required for model estimation in the ejection phase are  $P_A$  and  $f_A$ ; without these two measurements, the model parameters cannot be determined by the transfer function coefficients. Similarly,  $P_R$ ,  $P_A$ ,  $P_V$ , and  $f_V$  are available during the filling phase. The minimum measurements required for the fill phase are  $f_R$  and  $P_V$  or  $P_R$ . The Eqs for each stage, as well as a summary of available parameters, are shown in Table 4 [8].

**Table 4: Eqs and measurements to determine model parameters [8]**

Heart Action	Aortic Valve	Mitral Valve	System Equations	Estimator (Measurement)	Estimated Parameters
Ejection	OPEN ( $D_A$ on)	CLOSED ( $D_M$ off)	$d(f_A)/dt = (P_A - R_C f_A - P_S)/L_S$ $d(P_S)/dt = [f_A - (P_S - P_R)/R_S]/C_S$ $d(P_R)/dt = (P_S - P_R)/(R_S C_R)$	EKF  ( $P_A$ , $f_A$ , $P_R$ )	$R_C$ , $L_S$ ,  $C_S$ ,  $R_S$ , $C_R$
Filling	CLOSED ( $D_A$ off)	OPEN ( $D_M$ on)	$d(P_R)/dt = [(P_A - P_R)/R_S - f_R]/C_R$ $d(P_A)/dt = (-P_A + P_R) / (R_S C_S)$	EKF  ( $f_V$ , $P_R$ , $P_A$ , $P_V$ )	$C_R$ , $C_S$ ,  $R_S$ , $R_M$
Iso-volumic	CLOSED ( $D_A$ off)	CLOSED ( $D_M$ off)	$d(P_R)/dt = (P_A - P_R)/(R_S C_R)$ $d(P_A)/dt = (-P_A + P_R) / (R_S C_S)$	Solving Linear Equations  ( $P_A$ , $P_R$ )	$R_S C_R$ ,  $R_S C_S$

Another approach to utilizing variable estimations to control pump speed described by Boston et al uses a supervisor that chooses a speed based on available data [3]. The supervisor uses data estimated from the model, reliability of the estimated data, and the patient's level of activity to decide which control algorithm will determine the reference speed for the pump. The supervisor can choose a default, heuristic, or optimal performance control algorithm. A diagram of the controller is shown in Fig. 26 [3].

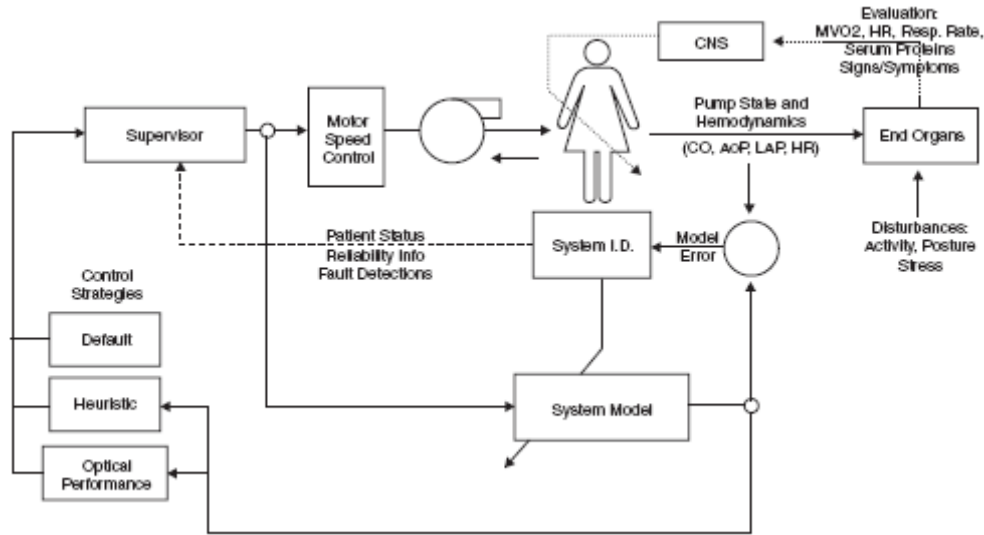


Figure 26: Control model using a supervisor [3]

Before the supervisor decides which algorithm will determine the reference speed, it must make several estimations of the patient's hemodynamic variables. To determine the total blood flow, the flow of the natural heart is added to the flow of the pump. The pump flow is estimated using Eq 7 [24], which is the ratio of the Fourier Transforms of AP and pump flow. The flow of the natural heart is estimated using contractility and flow pulsatility.

$$Q = \frac{1}{a_1 \omega^2} (1.5K_B I - B\omega - a_0 \omega^3) - j \frac{d\omega}{dt} \quad (7)$$

The supervisor must also determine pressure set points, which can be found using the systemic impedance. The AP set point is the sum of the pump pressure and end diastolic left ventricular pressure. Because end diastolic left ventricular pressure is small, the pump pressure provides an approximation to AP, which can be used to estimate systemic impedance [24].

Before the supervisor can select a control algorithm, it must determine if the estimates from the model are accurate. It makes its decision based on how reliable the model data is and the patient's history. If the supervisor determines that there is a system failure or reliability issue with the device, it operates in default mode. This causes the device to operate at a low constant speed that avoids suction and provides enough CO to sustain the patient. The system does not use any model estimates or sensory information, so it cannot respond to changes in CO demand [3].

If the supervisor determines that the model data are unreliable, a heuristic algorithm is chosen. This algorithm operates the pump at the highest possible speed that does not produce suction. No hemodynamic parameters are considered in determining the pump speed, only the pump characteristics. The assumption is made that LAP is low, and the ventricle is emptied without suction. The pump requires an indicator that detects when suction is occurring along with a control signal to maintain a safe speed [25].

One possible suction indicator is the pulsatility of the pump flow and motor current, which is caused by pulsatile load conditions. Fig. 19 [3] shows that as pump speed increases, ventricular unloading occurs and pulsatility decreases in each waveform. As seen in the far right waveforms in Fig. 19, pulsatility is at a minimum when suction occurs. Pulsatility can be used as a control signal by setting it to a reference value equivalent to a desired speed. The chosen speed must be safely above the minimum pulsatility that produces suction. A proportional integral fuzzy-logic controller was designed and tested in [3] that used pulsatility as a suction indicator.

Pulsatile waveforms may not always be available for use as a control signal. For example, a failing heart may not show pulsatility in the current waveform. Because the pump flow rate increases at an incrementally decreasing rate when pump speed is increased, the change in mean pump flow can be used as a control signal. When the pump matches venous return, the rate of change is approximately zero, creating a behavior called diminishing returns. The derivative of pump flow with respect to speed provides the diminishing returns index (DRI), which is an indicator of how much the pump is matching venous return. Suction occurs at the

point just before the derivative reaches zero. Because the goal of the heuristic algorithm is to set the pump speed as high as possible without producing suction, points just above the zero derivative provide a desirable operating range [25]. Another possible suction indicator is detecting the rapid drop in pump flow (MFI) that occurs briefly when suction is produced.

Another method for detecting suction uses multiple indicators to make a “majority rules” decision. A test described in [3] performed 42 *in vivo* experiments on three calves to compare the ability of each suction indicator to classify a pump speed as suction or no suction. The three indices used in this experiment were DRI, MFI, and the pulsatility index. The results of each indicator are shown in Table 5 [3]. The correct classification was made by all three or at least two of the indices 82% of the time, and by at least one 94% of the time. Instead of using just one indicator, a combination of indices can be used to increase the accuracy of the classification [3].

**Table 5: Comparison of different suction indices [3]**

Indices providing correct decision	Nonsuction	Suction	Total
All three indices	197	58	255
Two of the three indices	21	85	106
One of the three indices	7	42	49
None of the three indices	1	26	27
Total	226	211	437

To use a combination of indices to detect suction, an algorithm for making a decision based on several classifications is necessary. An additional classification category, the uncertain classification, is a new possibility for the final decision. The uncertain classification helps the supervisor avoid making incorrect decisions if the data provided does not produce a conclusive classification. In this case, the speed can be varied very little or not at all. If several consecutive uncertain classifications are received, a system may be necessary to force the supervisor to make a decision or set off an alarm. Several possible decision-making schemes have been proposed [26]: fuzzy logic, Dempster-Schafer theory, and an extended certainty-weighted detection system.

The fuzzy logic system converts index values to linguistic variables, which are defined by the fuzzy sets “suction absent” and “suction present.” The measure of uncertainty in the decision is the measure of the extent to which the decision does not belong to either set. This system tends to be responsive to conflicts in the indices.

The Dempster-Schafer decision system is set up as a hypothesis test, with the options being “suction present” and “suction absent.” Probability mass is assigned to each side based on index values. Probability not assigned to either side is a measure of uncertainty. A measure of uncertainty for each indicator is also provided. The Dempster-Schafer decision system is sensitive to multiple indices providing results between suction and no suction.

The extended certainty-weighted system uses certainty functions to provide a definite or uncertain decision. A diagram for the certainty-weighted system is shown in Fig. 27 [27]. The Definite Decision Block (DDB) uses decision rules  $A_1 - A_n$  to compare the measure of features  $y_1 - y_n$  to a local threshold. This comparison produces an output signal  $u_i$  that is weighted by a measure of certainty ( $C_i$ ) in the decision. The certainty reflects ambiguity in the parameter on which the decision is based. If the parameter is between two decisions, the certainty is reduced [29].

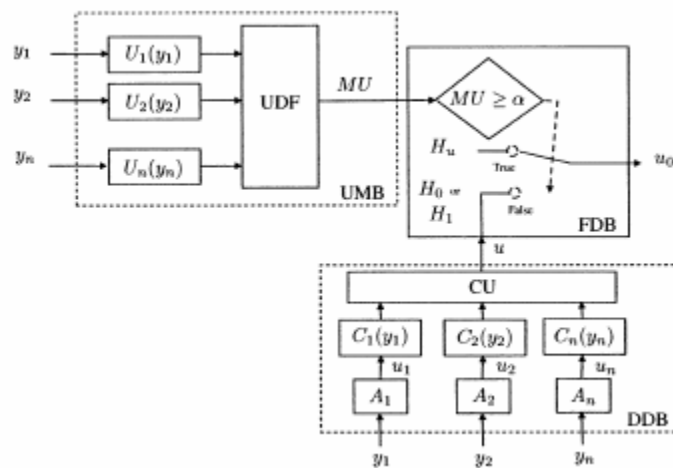
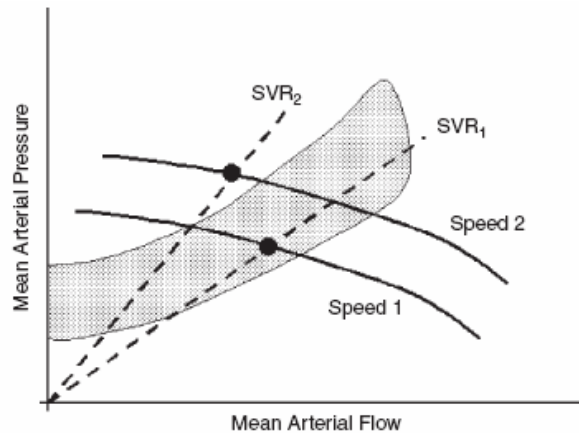


Figure 27: Extended certainty-weighted decision system block diagram [27]

The Uncertainty Measure Block (UMB) consists of uncertainty functions  $u_i$ , defined as  $u_i = 1 - C_i$ . The Uncertainty Data Fusion Block (UDF) combines the  $u_i$ 's to produce a Measure

of Uncertainty (MU), which is an average of the MU of each  $y_i$ . In the Final Decision Block (FDB), the MU is compared to a threshold  $\alpha$ . If  $MU > \alpha$ , the result is an uncertain decision. Otherwise, a definite suction or no suction decision is provided, as decided by the DDB [27].

Using suction indices operates the pump at a speed just below suction, maximizing CO while keeping speed at a safe level. But, by ignoring hemodynamic parameters, the algorithm may adjust the speed as seen in Fig. 28 producing unsafe AP. The shaded area represents a safe arterial flow and pressure range. The two dashed lines are two different values of systemic vascular resistance, and the curved lines represent the pressure-flow characteristics for two different speeds. If the patient's SVR increases from  $SVR_1$  to  $SVR_2$ , the controller will respond to the increase in load resistance by increasing pump speed to speed<sub>2</sub>. This increase in speed may increase AP, causing the pump to operate outside of the desired range. In this case the lower speed may be more desirable [3].



**Figure 28: Normal (gray) and unsafe (outside gray) physiologic operating regions [3]**

### 3.0 MULTIOBJECTIVE OPTIMIZATION

The previous section outlined several methods that can be used to control the speed of an LVAD. It was noted in section 2.7 that increasing the speed to provide more CO may cause an increase in AP, placing the patient in an unsafe operating region as a result of the high blood pressure. It follows that the level of CO is not adequate to determine the best pump speed. Constraints on other hemodynamic parameters must be considered to ensure that the patient is receiving adequate CO while operating at a safe speed.

In this work, the pump speed control problem will be formulated as a multiobjective optimization problem using a penalty function approach. The goal of this approach is to determine a pump speed  $\omega$  that minimizes a set of penalty functions for the hemodynamic parameters CO, AP, and LAP. However, as discussed below, it is impossible to minimize all three penalty functions with one pump speed. Therefore it is necessary to determine a set of noninferior pump speeds, which is referred to as the noninferior set (NIS). This section of the thesis will provide an explanation of the theory used to develop the results of this work.

The three penalty functions provide a measure of the performance of the system (heart plus LVAD). If a pump speed is found that minimizes all three penalty functions, the pump will be operating at an optimal point. The difficulty of an approach using multiple penalty functions is that it is generally impossible to determine a single pump speed that will minimize all three penalty functions simultaneously. A problem whose system performance is dependent on multiple variables is known as a vector-valued minimization problem [25]. In this case, several variables measure the performance of a system. A system  $S_1$  may be superior to a system  $S_2$  for some of the variables while  $S_2$  may be superior to  $S_1$  for the other variables.



The first part of this chapter provides a review of the NIS theory presented by Zadeh [30]. Zadeh’s approach used continuous, convex penalty functions and the results indicate a continuous NIS. Zadeh did not explicitly discuss results using non-convex or discontinuous penalty functions, or the possibility of the NIS containing a discontinuity. However, we found that, when mapping the hemodynamic penalty functions to functions of pump speed, the resulting penalty functions are non-convex. The non-convex penalty functions provided the motivation to investigate the relationship between the penalty functions and NIS. First, the effect of shifting three convex penalty functions was explored. After gaining an understanding of the three convex penalty function situation, one of the three penalty functions was changed to be non-convex. Another test was performed giving one of the penalty functions a discontinuous derivative. All testing was performed by creating three arbitrary penalty functions and simulating them in Matlab. The simulation results are presented and discussed following the review of Zadeh’s theory.

### 3.1 NONINFERIOR SET THEORY

An alternative to searching for one optimal speed is to instead search for a set of the “best” pump speeds, and choose the operating speed from this set. Zadeh refers to such a set of “best solutions” to a system as the noninferior set (NIS) [30]. To define inferiority, let  $\Omega \in \Sigma$  be defined as the feasible set, or set of possible solutions, and  $P(S)$  be the performance index of a system  $S$ . A system  $S_0 \in \Omega$  is noninferior if  $P(S_0) \geq P(S)$  for all  $S \in \Omega$ . A system is inferior if another system can be found that produces a better performance for all performance variables [30].

To find the NIS, let the performance of a system  $S$  be measured by the vector

$$P(\bar{x}) = [p_1(x), p_2(x) \cdots p_n(x)]$$

where  $\mathbf{x} = [x_1, \dots, x_n]$  are the adjustable parameters of S and the  $p_i(x)$ ,  $i = 1, \dots, m$  are their respective performance measures. Zadeh shows that an optimal point for  $\mathbf{P}(\mathbf{x})$  can be found by minimizing the function

$$p(\bar{x}; \bar{\mu}) = \mu_1 p_1(x) + \mu_2 p_2(x) + \dots + \mu_m p_m(x) \quad (8)$$

where  $\mu_i$ ,  $i = 1, \dots, m$  are positive, real-valued weighting factors [30]. The NIS can now be found by minimizing Eq 8 over the entire range of values of  $\mu_i$ . The result will be a set of optimal points corresponding to different values of weights. Each point in the NIS produces different effects on the performance of each entry of the performance vector  $\mathbf{p}(\mathbf{x})$ ; a point with a high value of  $\mu_1$  corresponds to a system with a better performance for  $p_1(\mathbf{x})$ . It is left to the system designer to choose a point in the NIS by determining the importance of each performance measure (that is, by determining the  $\mu_i$ ).

### 3.2 INVESTIGATION OF PENALTY FUNCTIONS

The penalty functions discussed in chapter four (Fig. 38) are results obtained from one group of clinicians. However, these penalty functions may not be ideal for all patients and may need to be adjusted for different patients. The hemodynamic penalty functions used are convex functions, each having a unique minimum. The minima correspond to the physiological values specified by the clinicians and are referred to as set points. Clearly, operating at a set point yields a penalty of zero.

It was found that when mapping the penalties from functions of physiologic variables to functions of speed the resulting penalty functions were not always convex. It was anticipated that the non-convex or discontinuous penalty functions may not provide a continuous NIS due to the possibility of several local minima.

Simulations were performed in Matlab to determine the effects of the penalty function on the NIS. The simulations were performed using Matlab because an analytical expression, other than the two penalty function situation, does not provide a clear understanding of how the NIS

point is affected by the values of the weights. The theory presented by Zadeh did not explicitly discuss the possibility of a discontinuous NIS, so the goal of the simulations is to determine if discontinuities in the NIS are possible and how a “break” in the NIS can be created.

Furthermore, if a discontinuity is created in the NIS, it must be determined if the entire set is useful or, for practical purposes, only a subset of the NIS should be presented to clinicians.

The simulations are arranged in the following manner. First, cases with two and three convex penalty functions are considered, along with the effects of shifting one of the penalty functions. Next, non-convexities were added by simulating a scenario with one penalty function having a discontinuous derivative and another with a continuous, non-convex penalty function.

### 3.2.1 Introduction to the NIS

To illustrate the concept of inferiority, consider the two penalty functions  $f_1(x) = 10(x-3)^2$  and  $f_2(x) = 20(x-6)^2$ , which are plotted in Fig. 29. Let  $x$  be an adjustable parameter of a system  $S$ , and  $f_1(x)$  and  $f_2(x)$  be performance measures of the system. Penalty functions can be used to measure the performance of a system by giving an increasingly higher penalty to a system whose performance moves farther from a desired set point. Clearly, a lower penalty implies a better performance of the system with respect to  $f_1(x)$  or  $f_2(x)$ .

Figure 29 indicates that  $x_1$  is an inferior point. If  $x$  is increased to  $x_2$ , the penalty of both penalty functions decreases, producing a better point. The same trend occurs as  $x_3$  is approached from the right. Moving from  $x_2$  to  $x_3$  produces a lower  $f_2$  penalty at the expense of an increased  $f_1$  penalty. When moving from  $x_3$  to  $x_2$ , the exact opposite occurs. Because one point is not superior to the other in regards to all of the performance variables,  $x_2$  and  $x_3$  are noninferior. For all values of  $x$  such that  $3 \leq x \leq 6$ , no point can be found that has a superior performance to another point with respect to each penalty function.

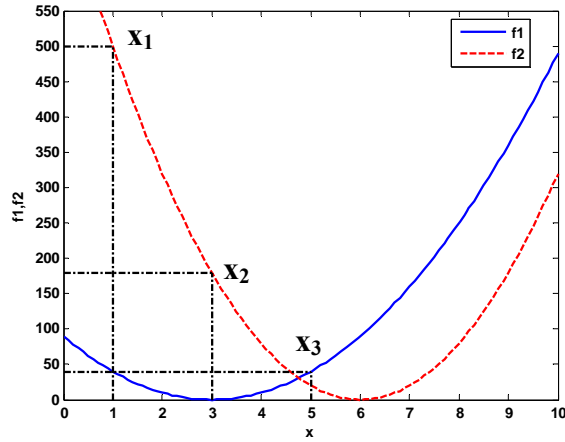


**Figure 29: Illustration of inferior and noninferior points**

In general, if two penalty functions are convex, all of the points between the minima of the two functions are noninferior. This set of solutions is referred to as the NIS and has the property that for any system  $S_o$  outside the non-inferior set, there is a system  $S_i$  inside the set that will decrease one penalty function without increasing another. In other words,  $S_o$  is inferior to  $S_i$ , implying that  $S_i$  is the better system. Clearly, a solution should be chosen from the NIS.

The NIS can also be determined analytically using Eq 8. For a given value of  $\mu$ , an optimal point can be found for the combined penalty function. The NIS will be the set of points that minimizes the combined penalty function  $J$  for all  $0 \leq \mu \leq 1$ .

To show analytically that the NIS spans the range between the minima of the two penalty functions, consider the case of two arbitrary penalty functions  $J_1$  and  $J_2$ . The combined penalty function to be minimized at different values of  $\mu_i$  is  $J = \mu_1 J_1 + \mu_2 J_2$ . The sum of the weights must be equal to one. Therefore in the two penalty function case  $\mu_2 = 1 - \mu_1$ , simplifying Eq 8 to

$$J = \mu_1 J_1 + (1 - \mu_1) J_2. \quad (9)$$

Consider determining the NIS point for  $\mu_1$  or  $\mu_2$  equal to 1. If  $\mu_1 = 1$ ,  $\mu_2 = 1 - \mu_1 = 0$ , reducing Eq 9 to  $J = J_1$  and the problem reduces to the minimization of  $J_1$ . Similarly, if  $\mu_2 = 1$  the minimum of  $J$  is the minimum of  $J_2$ . It follows intuitively that points in the NIS start at the

minimum of one penalty function and move to the minimum of the other penalty function as  $\mu$  is varied, creating a continuous NIS.

Let the weighted sum of the two penalty functions in Fig. 29 be defined as  $J = \mu_1 f_1(x) + \mu_2 f_2(x)$ , where  $\mu_2 = 1 - \mu_1$ . The minimum point of the combined penalty function can be determined analytically by

$$J = 10\mu_1(x - 3)^2 + 20\mu_2(x - 6)^2$$

$$\frac{dJ}{dx} = 20\mu_1(x - 3) + 40\mu_2(x - 6) = 0$$

$$x = \frac{3\mu_1 + 12\mu_2}{\mu_1 + 2\mu_2} \qquad \mu_2 = 1 - \mu_1$$

$$x = \frac{12 - 9\mu_1}{2 - \mu_1}$$

Figure 30a shows the problem graphically, where  $J_1$  (blue) is the solid line,  $J_2$  (red) is the dotted line, and the combined penalty function  $J$  (black) is the dashed line. The minimum of the combined penalty function for  $\mu_1 = 0.6$  and  $\mu_2 = 0.4$  is located at  $x = 4.7$ , agreeing with the analytical solution. Also notice that this point is located between the minima of the two penalty functions ( $x = 3$  and  $x = 6$ ). Repeating this process for all possible values of  $\mu$  produces the NIS as shown in Fig. 30b

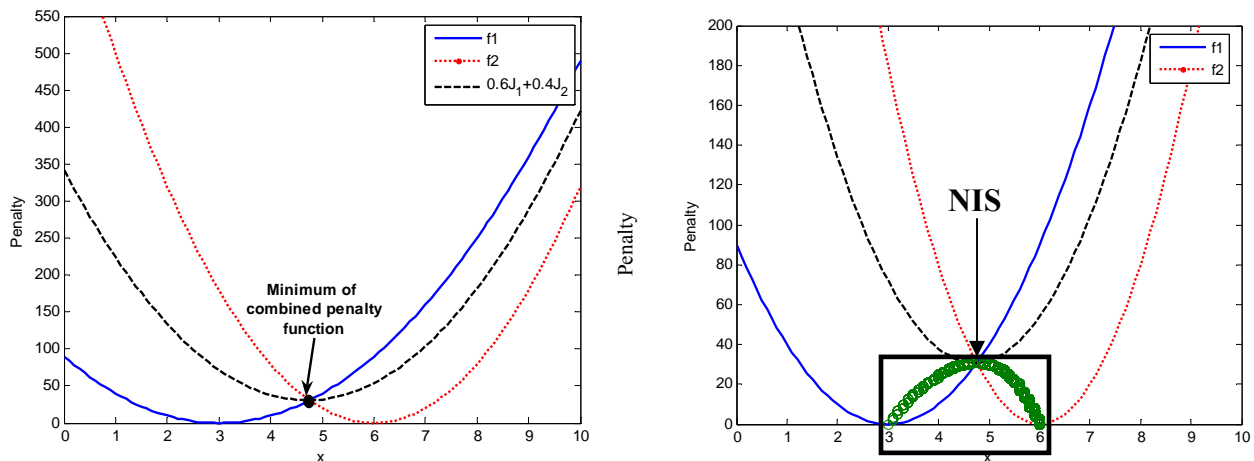


Figure 30: a) Penalty functions, with combined penalty function for  $\alpha_1 = 0.6$  b) Entire NIS

As expected, the NIS in Fig. 30b includes all values of  $x$  between  $x = 3$  ( $\mu = 1$ ) and  $x = 6$  ( $\mu = 0$ ). The blue circles indicate the penalty for different points in the set. In Fig. 30b a step size of  $\mu = 0.01$  was arbitrarily chosen. The NIS is continuous, and any real-valued  $x$  between three and six is a possible solution. It can also be observed that, as expected, no point in the NIS is superior to any other points in the NIS. As the NIS moves from  $x = 6$  to  $x = 3$ , the  $J_1$  penalty decreases while the  $J_2$  penalty increases. These results can be interpreted as indicating that as the desire increases to keep  $J_1$  low (i.e. the weight, or  $\mu_1$  increases), the best value of  $x$  moves towards  $x = 3$ , the minimum of  $J_1$ . The opposite occurs if  $J_2$  is more important than  $J_1$ .

### 3.2.2 Simulations of convex penalty functions

The previous discussion considered the case only of two penalty functions, but the NIS theory can be extended to include three penalty functions, each with their respective weights  $\mu_i$ ,  $i = 1, 2, 3$ . In this case, Eq 8 will not simplify to Eq 9, so the value of two weights must be specified, with the third weight found using the fact that the sum of the three weights must be one. The same method of optimizing a penalty function for different values of  $\mu_i$  is used for the three penalty function case. Because three values of  $\mu_i$  must be varied,  $\mu_3$  was arbitrarily chosen to be held at a constant value while the sum of  $\mu_1$  and  $\mu_2$  was varied from zero to  $1 - \mu_3$ . For the simulations,  $\mu_3$  was varied from zero to one in increments of 0.2. An increment of 0.2 was chosen because it provides a clear view of how penalty changes with changing  $\mu_i$  when plotting the NIS. The result is still a NIS that spans the range between the minima of the penalty functions, however in the case of three penalty functions it is between the two minima that are farthest apart.

To assist in the interpretation of the simulation results the entire NIS can be thought of as several subsets, each corresponding to a particular value of  $\mu_3$ . Within each of these subsets are optimal points corresponding to a combination of the three penalty functions with the same value of  $\mu_3$ , but with values of  $\mu_1$  and  $\mu_2$  varied using the method described above. Let a subset of the NIS for a specific value of  $\mu_3$  be denoted by  $NIS_{\mu_3}$ , where  $\mu_3 = 0, 0.1 \dots 1$ . The NIS consists of the noninferior points for all combinations of the three weights, so it follows that the NIS is the union of all of the subsets, or

$$NIS = \bigcup_{\mu_3=0}^1 NIS_{\mu_3} \quad (10)$$

The location of the penalty function minima with respect to each other is important in the three penalty function case. As the minima of the penalty functions are moved, the size and shape of the NIS are also changed, reflecting the property that the NIS spans the entire range between the two minima that are farthest apart.

To illustrate this point Matlab was used to create a series of simulations to find the NIS of three penalty functions. Two of the penalty functions,  $J_1$  and  $J_2$ , were chosen arbitrarily to maintain a fixed minimum point for all of the tests. The location of the minimum of a third penalty function  $J_3$  was then varied to observe the effects on the NIS. The three penalty functions used in these tests are shown below.

$$J_1 = 20(x - 0.5)^2 + 0.5 \quad (11)$$

$$J_2 = 30(x - 3)^2 + 2 \quad (12)$$

$$J_3 = 40(x - a)^2 + 1 \quad (13)$$

The parameter  $a$  in  $J_3$  is a constant that determines the location of the minimum of  $J_3$ . The minima of these functions, found using the derivative method shown below, are  $x = 0.5$ ,  $3$ , and  $a$  for  $J_1$ ,  $J_2$ , and  $J_3$  respectively.

$$\begin{array}{lll} \frac{dJ_1}{dx} = 40(x - 0.5) = 0 & \frac{dJ_2}{dx} = 60(x - 3) = 0 & \frac{dJ_3}{dx} = 80(x - a) = 0 \\ \therefore x = 0.5 & \therefore x = 3 & \therefore x = a \end{array}$$

The first test performed was for the case when  $a = 8$ , placing  $J_3$  outside the range of the minima of  $J_1$  and  $J_2$ . Figure 31 plots the three penalty functions along with the NIS. The solid blue line corresponds to  $J_1$ , the magenta dashed line  $J_2$ , and the red dotted line  $J_3$ . This convention will be used for the duration of the chapter.

As seen in Fig. 31, the NIS consists of all values of  $x$  between  $x = 0.5$  and  $x = 8$  (the boxed region), the two minima farthest from each other.  $NIS_{\mu_3}$  is plotted for  $\mu_3 = 0, 0.2 \dots 1$  using

a step size  $\mu_3 = 0.2$ . Each set of different colored markers in Fig. 31 corresponds to the penalty value for different  $NIS_{\mu_3}$ . The individual circles in each subset correspond to penalty values at points with different values of  $\mu_1$  and  $\mu_2$ .

Because  $\mu_3 = 0$  in  $NIS_0$  the problem reduces to two penalty functions,  $J_1$  and  $J_2$ . Consequently  $NIS_0$  spans the range from  $x = 0.5$  to  $x = 3$ , the minima of  $J_1$  and  $J_2$ . The range of noninferior values of  $x$  for increasing values of  $\mu_3$  is gradually “drawn” to the minimum of  $J_3$ .  $NIS_1$  reduces the problem to the minimization of one penalty function, so the optimal value of  $x$  is the minimum of  $J_3$  ( $x = 8$ ).

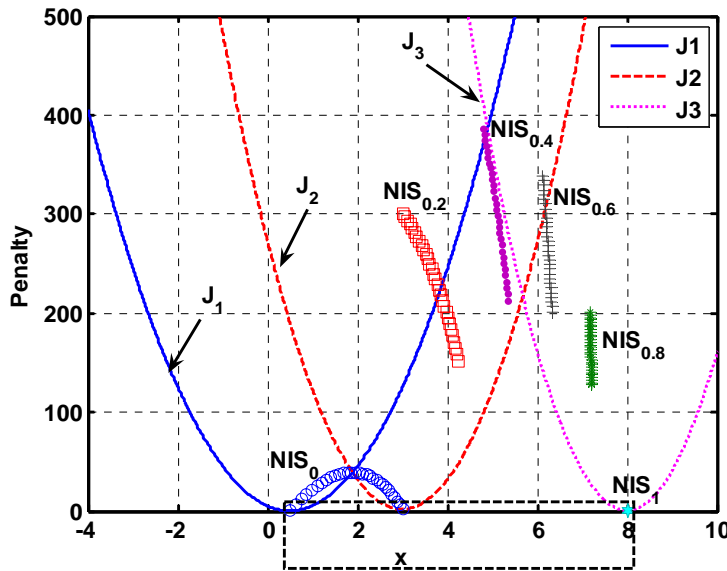


Figure 31:  $NIS_{\mu_3}$  using penalty functions in eqns 11-13,  $a = 8$

As  $\mu_3$  increases, the shape of the subsets in Fig. 31 gradually becomes a straight vertical line, indicating that the range of values of  $x$  in  $NIS_{\mu_3}$  is shrinking.  $NIS_1$  has the smallest range, consisting only of the minimum of  $J_3$ . This shape change has two explanations. First, the size of the range that  $\mu_1$  and  $\mu_2$  vary over is limited by  $\mu_3$ . For example, when  $\mu_3 = 0.2$ , the sum of  $\mu_1$  and  $\mu_2$  varies between zero and 0.8, but at  $\mu_3 = 0.8$ , the sum of  $\mu_1$  and  $\mu_2$  varies only between zero and 0.2. Also, at smaller values of  $\mu_3$  less weight is placed on  $J_3$  so noninferior values of  $x$  tend



to be closer to the minima of  $J_1$  or  $J_2$  depending on the values of  $\mu_1$  and  $\mu_2$ . As the third penalty function becomes more important the noninferior values of  $x$  move closer to  $J_3$ .

If  $J_3$  is not between the minima of the other two penalty functions, the NIS has the same characteristics seen in Fig. 31 regardless of where the minimum of  $J_3$  is. Consider changing the value of  $a$  to four, which is closer to the minimum of  $J_2$  than the previous test. The effects on the penalty value for points in the NIS can be seen in Fig. 32, and the range of values of  $x$  is indicated by the boxed region.  $NIS_0$  is the same as in the previous case and similar to Fig. 31, higher-valued  $NIS_{\mu_3}$  have shorter ranges of noninferior values of  $x$ . Also, the penalty values in Fig. 32 are lower than those in Fig. 31.

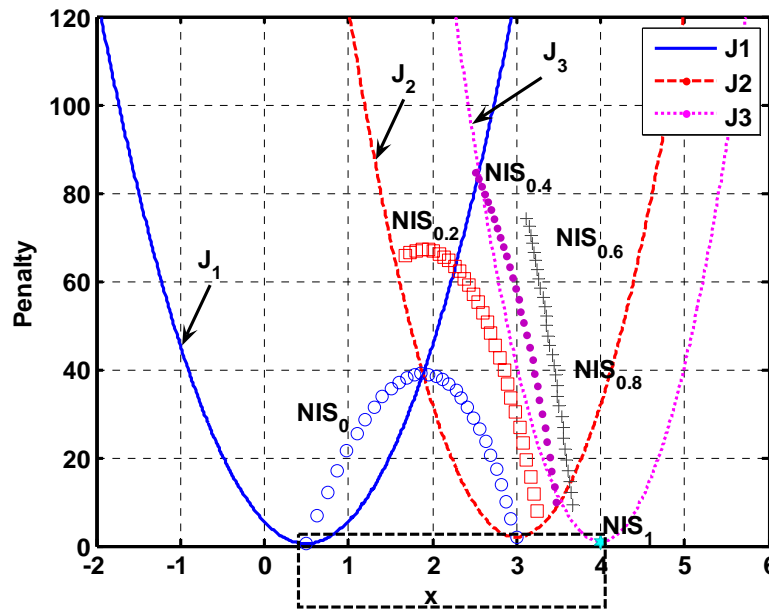


Figure 32:  $NIS_{\mu_3}$  using penalty functions in eqns. 11-13,  $a = 4$

Another penalty function location possibility is to place the minimum of  $J_3$  between the minima of  $J_1$  and  $J_2$ , as in Fig. 33. The NIS in Fig. 33 (indicated by the boxed region) behaves similar to the NIS in Figures 31 and 32. The NIS in Fig. 33 spans the range between the two most distant minima of the penalty functions,  $J_1$  and  $J_2$ . With increasing values of  $\mu_3$  the range of noninferior values of  $x$  and penalty values decreases for the different  $NIS_{\mu_3}$ . Like the examples in figures 31 and 32 the only noninferior value of  $x$  in  $NIS_1$  is the minimum of  $J_3$ .

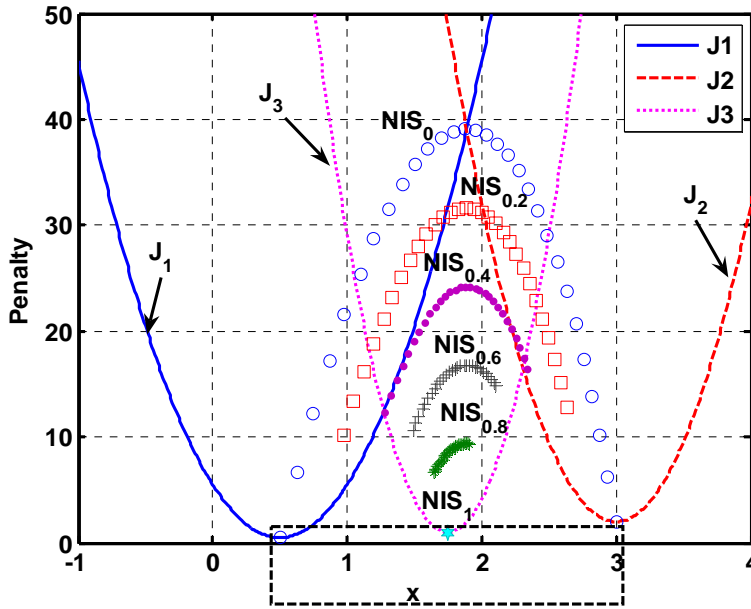


Figure 33:  $NIS_{\mu_3}$  using penalty functions in eqns. 11-13,  $a = 1.75$

The final penalty function location test was the case where two of the penalty functions share a minimum point. The two penalty functions that share a minimum point are scaled differently and shifted on the y-axis to ensure that they are different. Consider the case where  $a = 3$ , causing  $J_3$  to have the same minimum as  $J_2$ . The NIS (range of x values in boxed region) for this case is shown in Fig. 34. The NIS spans the range between the two minima and the range of noninferior values of x shrinks for increasing values of  $\mu_3$ . The penalty value for common values of x in  $NIS_{\mu_3}$  for  $0 \leq \mu_3 \leq 0.6$  increases slightly with increasing  $\mu_3$ . The penalty value for shared values of x in  $NIS_{\mu_3}$  for  $0.8 \leq \mu_3 \leq 1$  are approximately the same for increasing  $\mu_3$ .

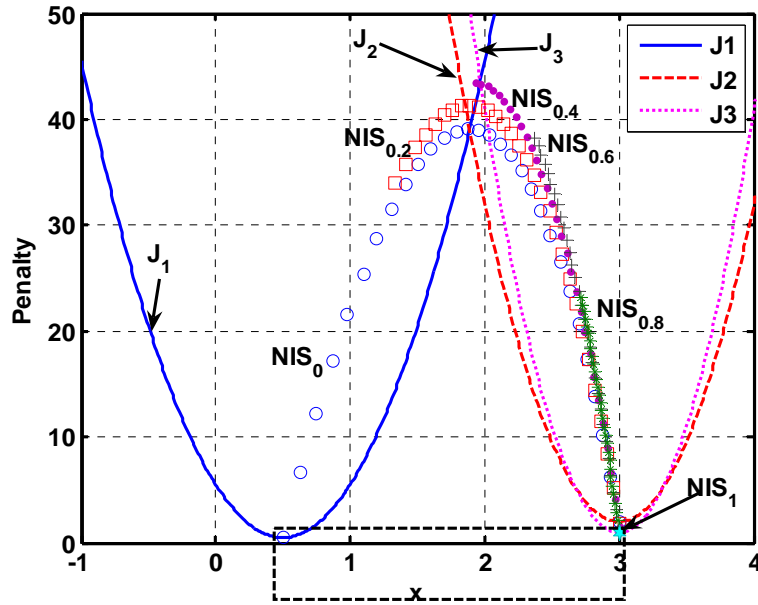


Figure 34:  $NIS_{\mu_3}$  using penalty functions in eqns. 11-13,  $a = 3$

The tests illustrated in Figures 31-34 confirm that for three convex penalty functions the NIS always spans the entire region between the two most distant penalty function minima, regardless of their position. Moving one of the penalty functions closer or farther from the other two penalty functions causes the range of the NIS to become longer or shorter, but it still remains between the two most distant minima. Also, the farther apart the penalty function minima are, the larger the penalty for increasing values of  $\mu_3$ . This is a consequence of the parabolic shape of the penalty functions. Depending on how the penalty functions are scaled the penalty can increase rapidly or slowly as a point moves away from the minimum. It is also concluded that the NIS is continuous when only convex penalty functions are considered.

### 3.2.3 Simulations with a non-convex penalty function

The previous discussion used only convex, continuous penalty functions. The next two simulations were performed to test the effects of a penalty function with a discontinuous derivative and a continuous non-convex penalty function.

Consider the same  $J_1$  and  $J_2$  penalty functions used in the previous examples (eqns. 11 and 12), but let  $J_3$  be defined as

$$J_3 = 20(x - 0.5)^2 - 50|x - 0.7| + 20. \quad (14)$$

The NIS for these three penalty functions was found using the method used to create figures 31-34 and is shown in Fig. 35 (indicated by the boxed region).  $J_3$  is not considered in  $NIS_0$  and the range of noninferior values of  $x$  is continuous. The discontinuous slope in  $J_3$  creates a “break” or discontinuity in the range of noninferior values of  $x$  in  $NIS_{\mu_3}$  for  $\mu_3 > 0$ , indicated by the region labeled  $\delta$ . The  $NIS_{\mu_3}$  points are connected by lines to indicate that the segments outside of the region  $\delta$  are continuous. Similar to figures 31-34 the range of noninferior values of  $x$  in  $NIS_{\mu_3}$  shrinks for increasing  $\mu_3$

In Fig. 35,  $J_3$  has two local minimum points,  $x = -0.75$  and  $x = 1.7$ . The range of  $x$  in  $NIS_{\mu_3}$  shrinks for increasing  $\mu_3$ , moving closer to one of the minima of  $J_3$ . The minimum point that  $NIS_{\mu_3}$  moves towards is determined by the values of  $\mu_1$  and  $\mu_2$ . As  $\mu_2$  increases and  $\mu_1$  decreases, the range of  $x$  is drawn to the minimum at  $x = -0.75$ . Conversely, increasing  $\mu_1$  and decreasing  $\mu_2$  causes a shift towards the minimum at  $x = 1.7$ . The direction of this shift is related to the location of the penalty functions. The minimum of  $J_1$  ( $x = 0.5$ ) is closer to  $J_3$ 's minimum of  $x = -0.75$ , while the minimum of  $J_2$  ( $x = 3$ ) is closer to  $J_3$ 's minimum of  $x = 1.7$ . Therefore, as  $\mu_1$  or  $\mu_2$  is increased, the range of  $x$  tends towards the minimum of the penalty function with the higher weight and in turn shifts towards one of the minima of  $J_3$ .

It is important to note that the NIS still spans the space between the two most distant minima, in this case the  $J_3$  minimum at  $x = -0.75$  and the  $J_2$  minimum at  $x = 3$ . However,  $NIS_{\mu_3}$  for  $\mu_3 > 0$  contain a discontinuity in the region indicated by  $\delta$  in Fig. 35. The “peak” in  $J_3$  creates a slightly higher penalty in a small region ( $\delta$ ), making it more desirable to choose a point outside this region. This discontinuous region in a sense creates a dead zone where noninferior values of  $x$  do not exist for  $\mu_3 \neq 0$ . Smaller increments were tested but no points were found in the region  $\delta$ .

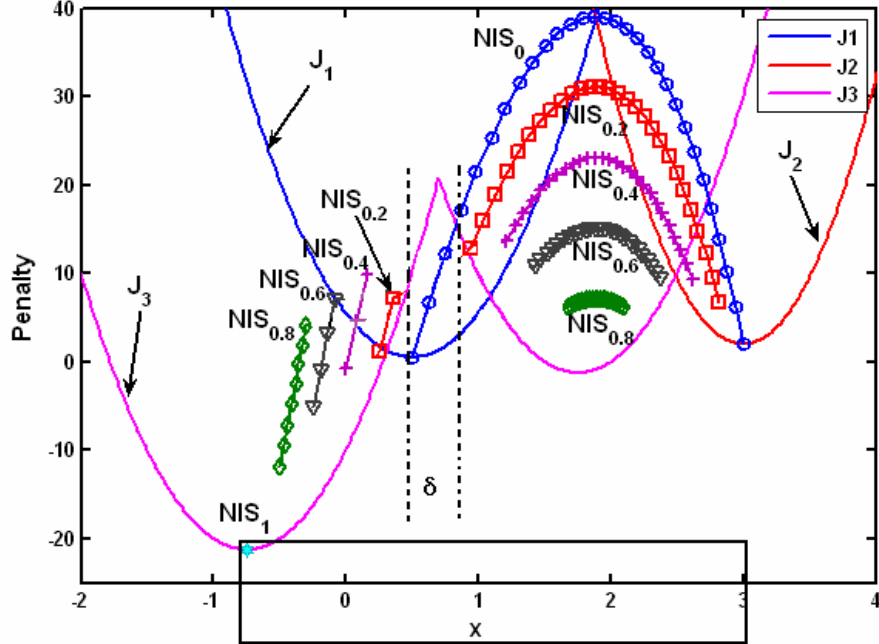


Figure 35: All  $NIS_{\mu_3}$  using penalty functions in eqns. 11, 12, and 14

The previous example used a penalty function with a discontinuous slope; however, a discontinuity can still appear in the NIS even if three continuous penalty functions are used. Consider the three continuous penalty functions given below. Only  $J_2$  and  $J_3$  are convex;  $J_1$  has a concavity, creating two local minima.

$$J_1 = (x - 3.5)^2 - 1.2 \quad (15)$$

$$J_2 = x^2 - 1.2 \quad (16)$$

$$J_3 = \frac{1}{4}x^4 - 3.083x^3 + 10.125x^2 - 4.5x + 1 \quad (17)$$

The three penalty functions are plotted in Fig. 36 with the boxed region indicating the range of the NIS. For any  $NIS_{\mu_3}$  such that  $0 \leq \mu_3 \leq 0.2$ , the range of  $x$  is continuous. For  $NIS_{\mu_3}$  with  $\mu_3 \geq 0.2$ , it can be seen in Fig. 36 that the range of  $x$  is discontinuous due to the concavity in  $J_1$  causing a “break” in the NIS for values of  $x$  between approximately  $x = 2$  and  $x = 4$ . The different colored circles represent penalty values for values of  $x$  in  $NIS_{\mu_3}$ , and Fig. 36 shows that

the range of the  $NIS_{\mu_3}$  for  $\mu_3 \geq 0.2$  includes values of  $x$  on either side of the concavity of  $J_3$ . The points move closer to  $J_1$  or  $J_2$  depending on which penalty function has the higher value of  $\mu$ .

The discontinuity also makes intuitive sense. If a point is chosen in the discontinuous region, an increase in  $J_3$  penalty will result due to the concavity, making these points inferior to the points not in the discontinuous region.

Similar to the case studied in Fig. 35, the NIS still spans the entire range between the two minima of furthest distance. However, the non-convexity causes several of the subsets to have a discontinuous region that arises from the fact that a lower penalty can be found outside of this region. The values of  $x$  not included in  $NIS_{\mu_3}$  for  $\mu_3 \geq 0.2$  are included in  $NIS_{\mu_3}$  for  $\mu_3 < 0.2$  because  $\mu_3$  does not have enough influence on the combined penalty.

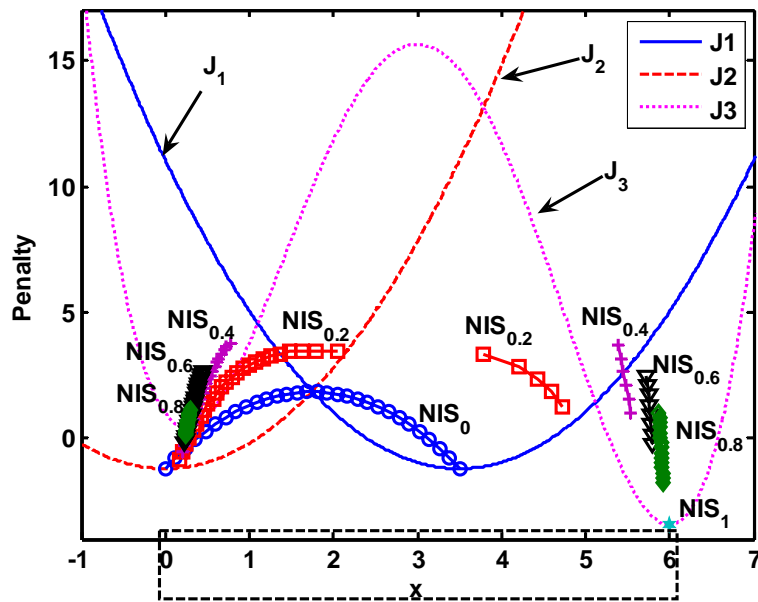


Figure 36: One continuous, non-convex penalty function

The results in Figures 31-36 indicate that the NIS is “drawn” to the minima of a specific penalty function as weighting shifts to that penalty function. Although the complete NIS is continuous in the simulations, subsets can be discontinuous if penalty functions are non-convex.

## 4.0 RESULTS OF APPLICATION TO PUMP SPEED SELECTION

### 4.1 PENALTY FUNCTION ACQUISITION

Choosing an optimal pump speed is not just a matter of selecting the speed that maximizes CO; several criteria must be taken into consideration. The chosen pump speed affects different criteria in different ways. Some criteria may benefit from an increased pump speed while others may deteriorate. A team of clinicians at the University of Pittsburgh Artificial Heart Program was able to provide three constraints for ventricular assistance:

1. CO should be above the minimum value, usually between 3-6 L/min, that is required to support the patient's activity level.
2. LAP should be below approximately 10-15 mmHg and above 0 mmHg.
3. Systolic AP should be maintained between patient-specific limits to limit sensitivity to afterload.

LAP is constrained to be above 0 mmHg to avoid suction and below approximately 10-15mmHg to avoid pulmonary edema. Systolic AP is a patient specific constraint, but the desired range of pressure is chosen to avoid hypertension and hypotension [3].

To determine an optimal speed that meets the three criteria, the penalty function method presented in Chapter Three was used. The AP penalty function should be symmetric about its set point, since pressures that are either too high or too low create a risk to the patient. The penalty functions for LAP and CO are both asymmetric about their set points. The asymmetry of CO and LAP is due to the fact that a higher penalty is assigned to values of LAP and CO below their set points. The higher penalty below the set points is motivated by the need to provide adequate CO and prevent suction, which is produced by negative LAP. Increases in CO and LAP above the set point are acceptable until certain values (10-15 mmHg for LAP, or a CO that cannot be maintained by the current AP) [3, 25]. Consequently, the penalty will increase at a slower rate

for points above the set point. The set points defined by the team of clinicians are CO = 11L/min, AP = 100mmHg, and LAP = 5mmHg.

The above criteria were used in conjunction with several break points for each of the three hemodynamic variables to create a penalty function for each of the three hemodynamic variables. A fourth-order polynomial was fit to the break points using Matlab's least squares algorithm [36]. The resulting penalty function polynomials are given by

$$f_1(x) = -12.09 * 10^{-6} x^4 + 0.0044x^3 - 0.4974x^2 + 15.4466x + 235.8525 \quad (18)$$

$$f_2(y) = -0.0031y^4 + 0.1513y^3 - 1.33724y^2 - 9.3258y + 104.2651 \quad (19)$$

$$f_3(z) = 0.0006z^4 - 0.0365z^3 + 1.0083z^2 - 8.8296z + 24.9008 \quad (20)$$

where  $f_1(x)$ ,  $f_2(y)$ , and  $f_3(z)$  are the penalty functions for AP, CO, and LAP, respectively. The variables  $x$ ,  $y$ , and  $z$  represent values of AP, LAP, and CO, respectively. The resulting curves for each polynomial are shown in Fig. 37.

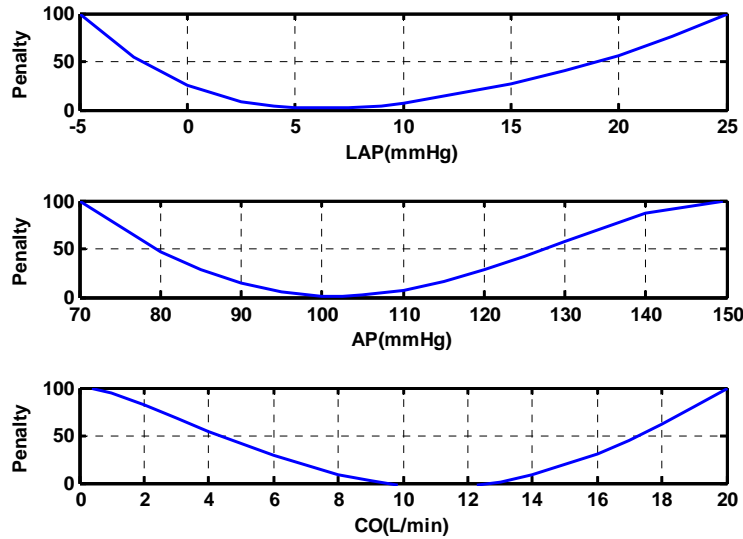


Figure 37: Hemodynamic penalty functions [3]



The penalty functions in Fig. 37 are functions of the three hemodynamic variables, not pump speed. In other words, a penalty is being assigned to values of CO, AP, and LAP. To find the penalty associated with a given pump speed, it is necessary to obtain the penalty functions as functions of pump speed.

The penalty functions with respect to speed could be measured from the patient directly, but this would require a variety of measurements that can potentially harm the patient [3]. In this work, the model in Fig. 13 [28] was used to estimate AP, CO, and LAP for a given speed input. These estimates were used to relate pump speed to the three variables, allowing the creation of the penalty functions as functions of pump speed. The block diagram in Fig. 38 describes the process used to obtain the penalty functions as functions of pump speed.

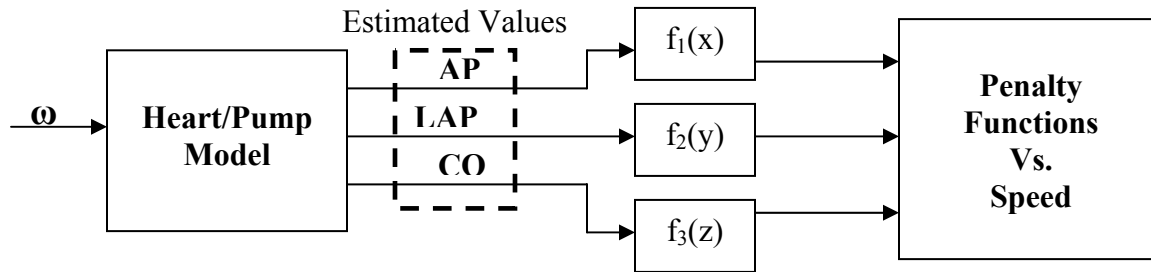
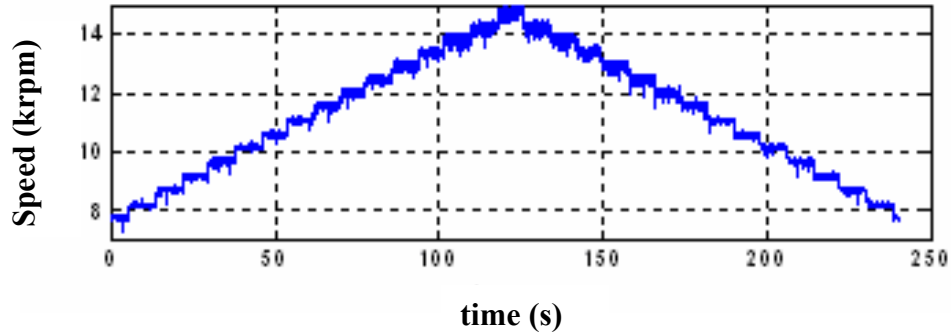


Figure 38: Process to obtain penalty functions as functions of speed

The speed input to the model was taken from a set of *in vivo* experiments using calves implanted with a Nimbus VAD (Nimbus Medical, Rancho Cordova, CA) [34, 35]. The axial flow pump was implanted using two connections: an inflow connection from the apex of the left ventricle to the inflow entrance of the pump and an outflow connection from the outflow point of the pump to the aorta. The animal experimental protocol was approved under the guidelines of the University of Pittsburgh Institutional Care and Use Committee.

The speed input to the model was a step input that increased from 7.7krpm to 15krpm in increments of 0.5krpm, then decreased back to 7.7krpm in decrements of 0.5krpm. The speed input can be seen in Fig. 39. All of the parameter values used in the model were unchanged from the values presented by Choi [28] except  $E_{max}$ , which was changed to 0.8, just under half of the

value for a healthy heart ( $E_{\max} = 2.0$ ). The pump will be given to patients with sick hearts, so the value of 0.8 was chosen so simulations could be performed using a sick heart.



**Figure 39: Speed input used to determine speed penalty functions**

The data provided by the model were the instantaneous AP, LAP, and CO waveforms. Mean values of CO and LAP were taken from these waveforms. Peak values of AP were used because systolic AP, the peak value of the AP waveform, is the pressure of interest for the AP penalty function [3]. All mean and peak data were obtained at every complete cardiac cycle of the model output waveforms.

The penalty functions in Fig. 37 are defined only over the regions shown in their respective plots. Outside of these regions the polynomial fits begin to deteriorate. Consequently, an accurate penalty value cannot be found for values outside the defined range of the original penalty functions. This issue is resolved by making the assumption that because the penalty functions are convex, penalty continues increasing as values move outside the defined range. In these tests it is assumed that any variable that yields a penalty greater than 100, the maximum penalty defined for each penalty function, is highly undesirable and all possible actions would be taken to leave this range. Only speeds that maintain all hemodynamic variables within the defined range of the penalty functions are considered; any speed that drives at least one of the variables out of the defined range is discarded. In the case of Fig. 37, at pump speeds greater than 13krpm AP exceeded 150mmHg, the maximum value defined on its penalty function. Therefore, data associated with speeds in the 13-15krpm range were discarded.

The speed input was increased then decreased, which resulted in two values of each hemodynamic variable at each speed in the test. After discarding invalid speeds, the data was sorted using Matlab's *sort* function. Data was sorted with respect to speed from the lowest speed to the highest. After sorting the data, Matlab's *smooth* command was used to smooth the data using a moving average filter [37]. An example of the data before sorting and smoothing is seen in Fig. 40. The solid lines indicate data for the increasing portion of the speed input and the dashed line the decreasing portion. Fig. 41 shows the sorting and smoothing results.

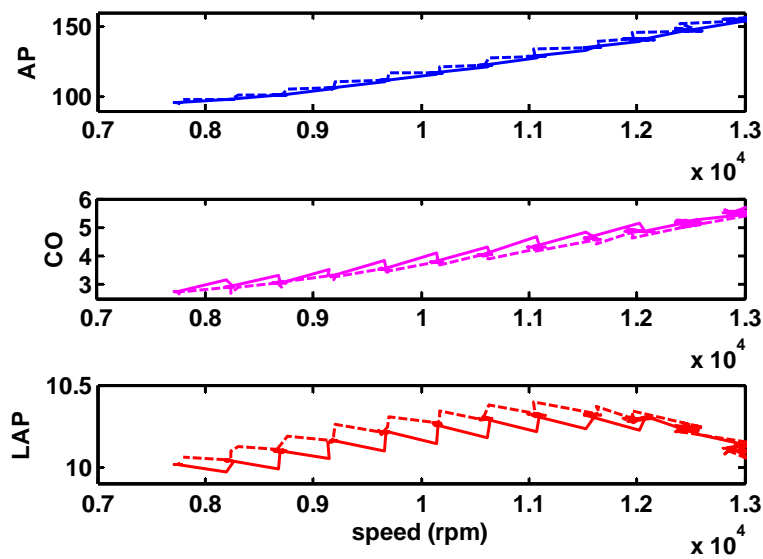


Figure 40: Hemodynamic data before sorting and smoothing

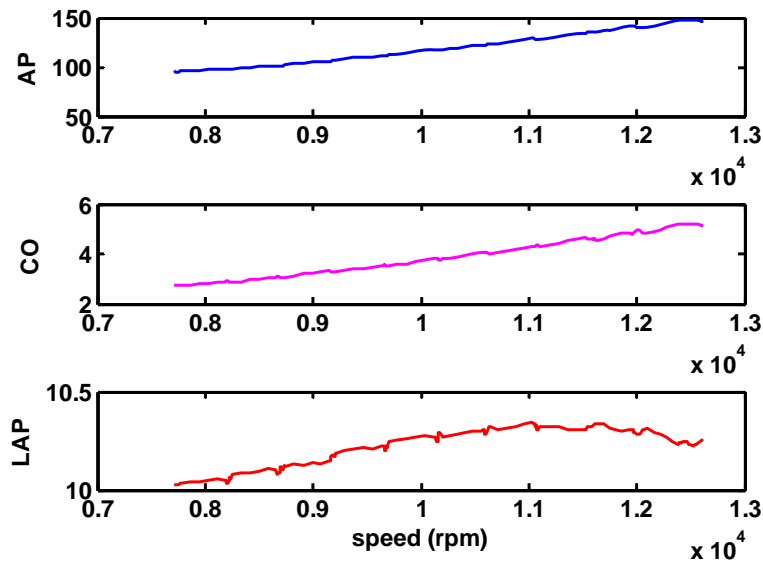


Figure 41: Hemodynamic data after sorting and smoothing

Finally, the speed penalty functions, denoted  $J(\omega)$ , were found by evaluating the penalty function polynomials in Eqs 18, 19, and 20 using the sorted and smoothed data. The resulting penalty functions are shown in Fig. 42. The solid curve (blue) is the AP penalty function,  $J_{AP}$ . The dotted curve (red) is the LAP penalty function,  $J_{LAP}$ . The dash-dot curve (magenta) is the CO penalty function  $J_{CO}$ . The line labeling scheme will be used for the remainder of this work.

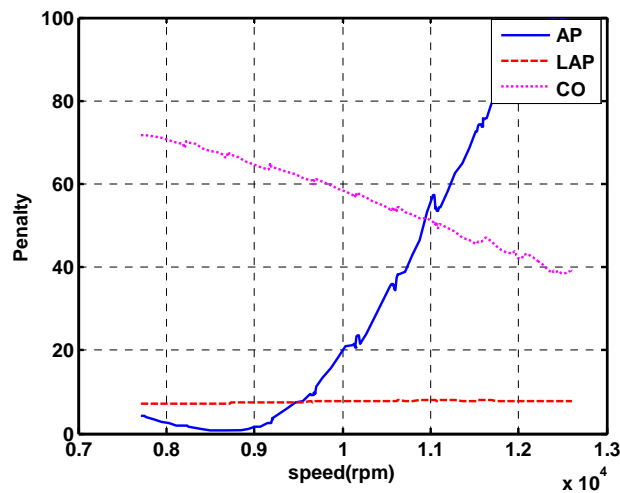
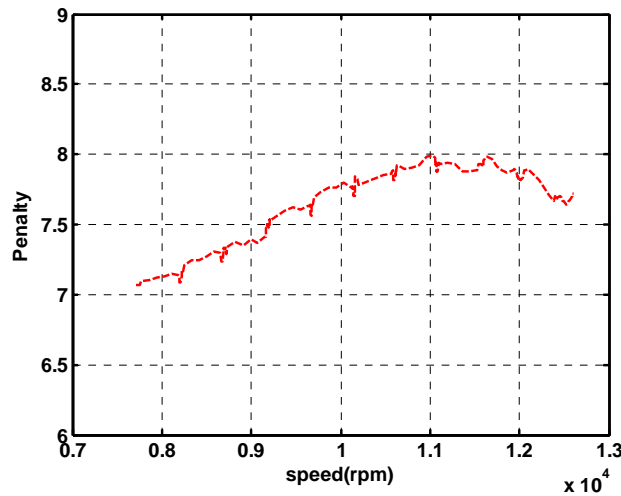


Figure 42: Penalty for each hemodynamic variable with respect to speed

The penalty functions in Fig. 42 illustrate how the penalty changes with speed. For example, increasing speed decreases CO penalty but increases AP penalty. The LAP penalty function is approximately a constant. However, Fig. 43, an expanded plot of  $J_{LAP}(\omega)$ , shows that penalty is changing between penalty values of seven and eight. This nearly constant penalty is due to the fact that the mean value for LAP determined by the model is approximately constant for pump speeds in the 7 to 13krpm range, as seen in Fig. 41.



**Figure 43: Penalty for LAP at varying speeds**

As seen in Fig. 41 CO and AP are monotonically increasing as pump speed is increased. Referring to the hemodynamic penalty functions in Fig. 37, as CO increases from below the set point of 11L/min, the penalty decreases, which is the behavior shown in Fig. 42.

From 7.7krpm to 9krpm,  $J_{AP}$  decreases to a penalty of zero then increases for the remainder of the speed range after 9krpm. This is due to the fact that the AP data is increasing from a pressure that is below the set point of 100mmHg in Fig. 37. As pressure increases to 100mmHg, the penalty decreases, but as the AP data increases past 100mmHg, the penalty begins to increase.

The penalty functions in Fig. 42 are not smooth curves. The small dips create non-convexities in the penalty functions that create the same effects on the NIS observed in figures 36 and 37. To avoid discontinuities in NIS subsets, a least-squares polynomial fit was applied to

the data obtained from evaluating Eqs 18-20 using the sorted and smoothed data. The penalty functions obtained from the polynomial fit are seen in Fig. 44.  $J_{AP}(\omega)$  (blue) is the solid line,  $J_{CO}(\omega)$  (magenta) is the dotted line, and  $J_{LAP}(\omega)$  (red) is the dashed line. A discussion of the effects of the unsmoothed penalty functions on the NIS can be found in appendix A.

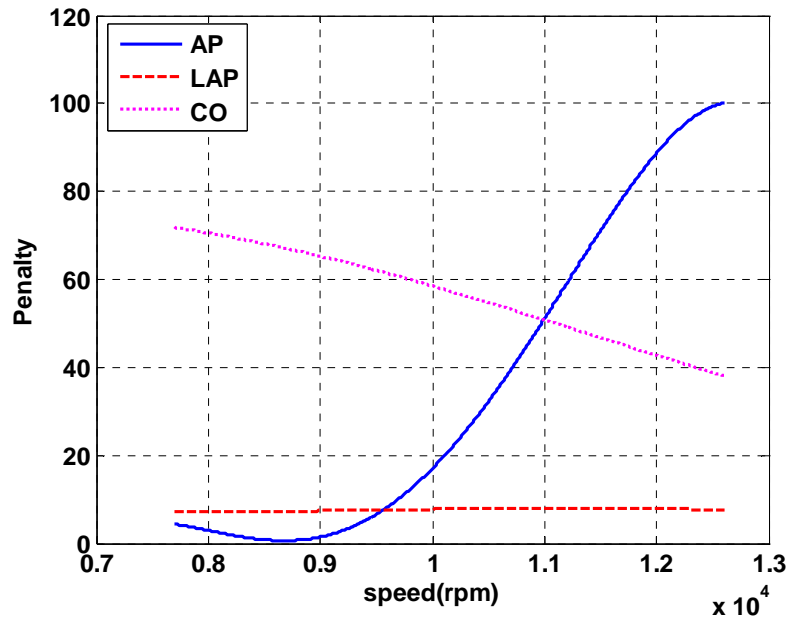


Figure 44: Penalty functions resulting from polynomial fit

## 4.2 NONINFERIOR SET

A performance measure for the system can be defined as  $J(\omega) = [J_{CO}(\omega) J_{AP}(\omega) J_{LAP}(\omega)]$ , where  $\omega$  is the pump speed in revolutions per minute (rpm). Choosing a single pump speed to minimize all three penalty functions in Fig. 40 is not possible and the problem was formulated as the vector-valued minimization problem described in Chapter Three [30]. The solution to the problem is the NIS of pump speeds, which is a set of speeds with the property that given a speed outside the set, a speed inside the set can be found that decreases the penalty for at least one of the penalty functions without increasing the penalty of any others.

The NIS is found by minimizing the combined penalty function

$$J = \mu_{CO}J_{CO} + \mu_{LAP}J_{LAP} + \mu_{AP}J_{AP} \quad (21)$$

at varying values of  $\mu_{CO}$ ,  $\mu_{LAP}$ , and  $\mu_{AP}$ , where  $\mu_{CO}$ ,  $\mu_{LAP}$ , and  $\mu_{AP}$  are real-valued weights for each hemodynamic variable with values  $0 \leq \mu_i \leq 1$ , and must sum to one. Note that increasing the value of a particular  $\mu_i$  increases the “importance” of its corresponding hemodynamic variable. Given a set of weights  $\boldsymbol{\mu} = [\mu_{CO} \ \mu_{LAP} \ \mu_{AP}]$ , the speed that produces the smallest penalty on the corresponding combined penalty function  $J$  is a point in the NIS.

The NIS was found using a procedure similar to the procedure used in the three penalty function examples from chapter 3. The value of  $\mu_{AP}$  was held constant while  $\mu_{CO}$  was varied over the range  $0 \leq \mu_{CO} \leq 1 - \mu_{AP}$ . Subsets of the NIS for different values of  $\mu_{AP}$  are denoted by  $NIS_{\mu_{AP}}$ , where  $\mu_{AP} = 0, 0.1, \dots, 1$ . Because the sum of the three weights must be one,  $\mu_{LAP}$  was determined using the relationship  $\mu_{LAP} = 1 - \mu_{CO} - \mu_{AP}$  for each value of  $\mu_{CO}$  and  $\mu_{AP}$ . This process was repeated for  $0 \leq \mu_{AP} \leq 1$ , with  $\mu_{AP}$  being incremented in steps of 0.1.

Fig. 46 shows the speeds for all combinations of weights in the NIS for a given value of  $\mu_{AP}$ . There are an infinite number of values of  $\mu_{AP}$  from zero to one that can be used, but here (see Fig. 46) only increments of 0.1 are considered. Increments of 0.1 were chosen for practical purposes and clarity; it is probably unreasonable to ask a clinician to make adjustments to  $\mu$  smaller than 0.1. This incremental value also makes the results (i.e. Fig. 46) clearer and easier to follow.

Each combination of weights corresponds to a different combined penalty function  $J$ , where the speed that produces the minimum penalty on  $J$  is a member of the NIS. Therefore, the NIS can be found by minimizing the combined penalty function  $J$  for all values of  $\mu_{CO}$ ,  $\mu_{AP}$ , and  $\mu_{LAP}$ . The NIS for the three penalty functions in Fig. 44 is shown in Fig. 45. Each different colored set of points in Fig. 45 represents a different  $NIS_{\mu_{AP}}$  and each circle represents the penalty value corresponding to a point with specific values of  $\mu_{CO}$  and  $\mu_{LAP}$ . The individual penalty functions are also included on the plot to indicate the penalty each variable incurs for a given point in the NIS.

It was originally believed that using convex hemodynamic penalty functions would map to convex penalty functions as functions of speed. It follows that the NIS was expected to be a continuous set of speeds that span the range of the two most distant minima of the penalty functions. However, the results in Fig. 45 show that the three penalty functions are non-convex. The NIS still includes points in the range that spans the two most distant minima, which are the  $J_{LAP}(\omega)$  minimum at  $\omega = 7.7\text{krpm}$  and the  $J_{CO}(\omega)$  minimum at  $\omega = 12.6\text{krpm}$ . Similar to the penalty function simulations in figures 36 and 37 of Section 3.2.3. the non-convex shape of  $J_{LAP}$  and  $J_{CO}$  cause a “break” in  $NIS_{\mu_{AP}}$  for  $\mu_{AP} \geq 0.1$ . The break is attributed to the concave shape of  $J_{LAP}(\omega)$  (Fig. 43). Similar to the continuous, non-convex penalty function in Fig. 36, the concavity creates slightly higher penalty values, making it more desirable to operate outside of the non-convex region.

It is important to determine how the breaks in the NIS affect the clinician’s speed choices. If the breaks are discontinuities creating a disjoint NIS the boxed regions in Fig. 46 are not included in the NIS and the clinician should not choose a speed in this region. Consequently, the usefulness of the outlier speeds and whether they can be ignored must be considered. If the breaks are a result of the speed discretization, then the NIS is not disjoint, and any speed between the two minima is in the NIS and a possible choice for the clinician. If the breaks are not a result of speed discretization, then the NIS is disjoint and speeds in the boxes are not part of the NIS.



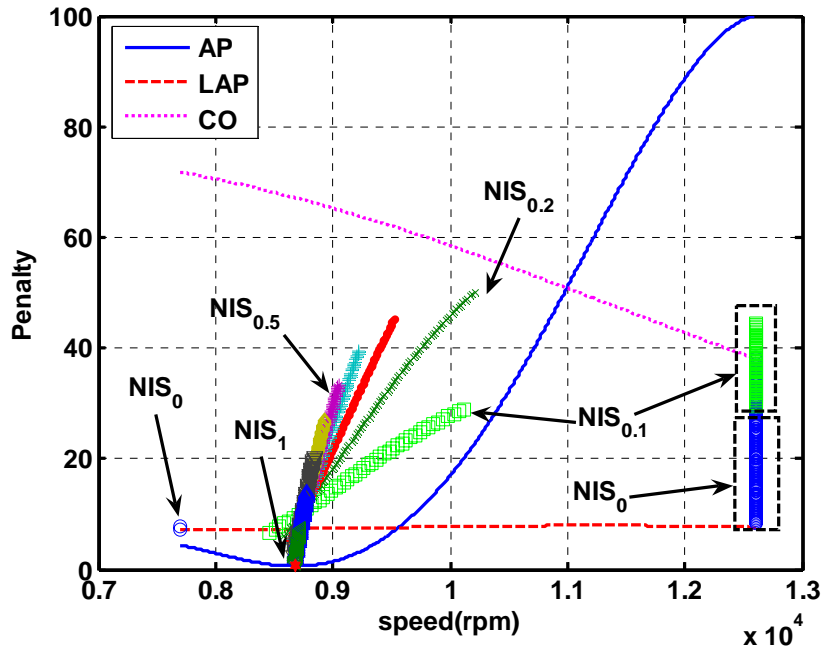


Figure 45: Penalty functions and NIS

$NIS_0$  and  $NIS_{0.1}$  are disjoint, not containing points in the areas inside the boxes in Fig. 46. Outside of the boxed regions the  $NIS_{\mu_{AP}}$  for  $\mu_{AP} > 0.1$  are continuous and represented as lines. The noninferior speeds in  $NIS_0$  are 7.7krpm for values of  $\mu_{LAP}$  greater than 0.985 ( $\mu_{CO} = 0.015$ ) and 12.6krpm for all  $\mu_{LAP} < 0.985$  ( $\mu_{LAP} \geq 0.015$ ). The speed range for  $NIS_{0.1}$  is continuous over the range 8.5-1.1krpm for values of  $\mu_{CO} \leq 0.4$  ( $\mu_{LAP} \geq 0.6$ ) and jumps to 12.6krpm for all  $\mu_{CO} > 0.4$  ( $\mu_{LAP} < 0.6$ ).

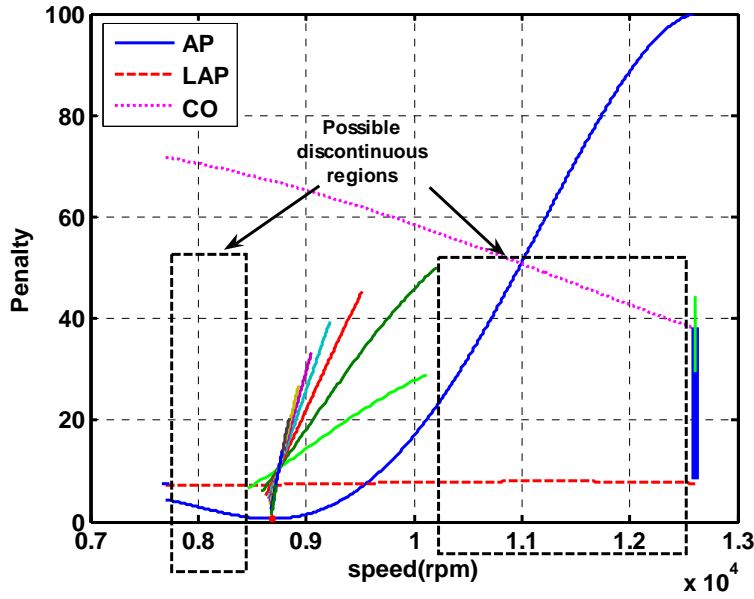


Figure 46: Regions of interest for discontinuity test

Several tests were performed to determine if the two jumps occurring in  $NIS_0$  or  $NIS_{0.1}$  are discontinuities or the result of a speed discretization that is too large. The goal of the tests was to try to select a set of weights  $\mu = [\mu_{CO} \mu_{AP} \mu_{LAP}]$  whose combined penalty function  $J$  has a minimum point that lies in one of the two boxes in Fig. 46. If such a point can be found, it corresponds to a speed in a NIS subset, and consequently the jumps are caused by the speed discretization. If such a point cannot be found, i.e. no set of weights  $\mu$  yields a point in one of the boxed regions, the jumps are discontinuities and the NIS is disjoint.

To find a point in one of the boxed regions in Fig. 46 a “divide and conquer” approach was used to investigate smaller ranges of weights in  $NIS_0$  and  $NIS_{0.1}$ . In exploring each subset the values of  $\mu_{CO}$  and  $\mu_{LAP}$  were incremented in the same manner as before. The values of  $\mu_{CO}$  immediately before and after the jump in speed ( $\mu_{COa}$  and  $\mu_{COb}$ , respectively) were found. Without moving to a new  $NIS_{\mu_{AP}}$ ,  $\mu_{CO}$  was varied between  $\mu_{COa}$  and  $\mu_{COb}$  in smaller increments than those used in the previous search. New values of  $\mu_{CO}$  immediately before and after the jump were again found (new values of  $\mu_{COa}$  and  $\mu_{COb}$ ), and the process was repeated until Matlab’s significant digit limit was reached. The different ranges of  $\mu_{CO}$  for  $NIS_0$  and  $NIS_{0.1}$  tested along with their respective step sizes are shown in Table 6.

**Table 6: Ranges of  $\mu_{CO}$  tested and their respective step sizes**

NIS <sub>0</sub>			NIS <sub>0.1</sub>		
Step size	$\mu_{COa}$	$\mu_{Cob}$	step size	$\mu_{COa}$	$\mu_{Cob}$
10-3	0	1	10-4	0	0.9
10-6	0.015	0.019	10-6	0.4045	0.4048
10-9	0.017242	0.017246	10-9	0.404617	0.40462
10-12	0.017243622	0.017243625	10-12	0.404618103	0.404618106
10-15	0.017243623481	0.017243623484	10-15	0.404618104758	0.404618104761
10-18	0.017243623482657	0.01724362348266	10-18	0.404618104759206	0.404618104759209
	0.017243623482659	0.017243623482659		0.404618104759208	0.404618104759208

As seen in Table 6,  $\mu_{CO}$  was incremented in increments as small as  $10^{-18}$  for NIS<sub>0</sub> and NIS<sub>0.1</sub>. In each case, the NIS <sub>$\mu_{AP}$</sub>  speed jumped from one speed to another, creating the gaps seen in the boxed regions in Fig. 46. No speeds were found in these regions, and it was concluded that the NIS is the disjoint set of speeds  $\omega = \{7.7\text{krpm}, 8.4\text{-}10.2\text{krpm}, 12.6\text{krpm}\}$ .

The discontinuity in NIS<sub>0</sub> is caused by the shape of the combined penalty function for  $\mu_{AP} = 0$ . Fig. 47 shows the combined penalty function using values of  $\mu_{CO}$  immediately before and after the jump in speed.

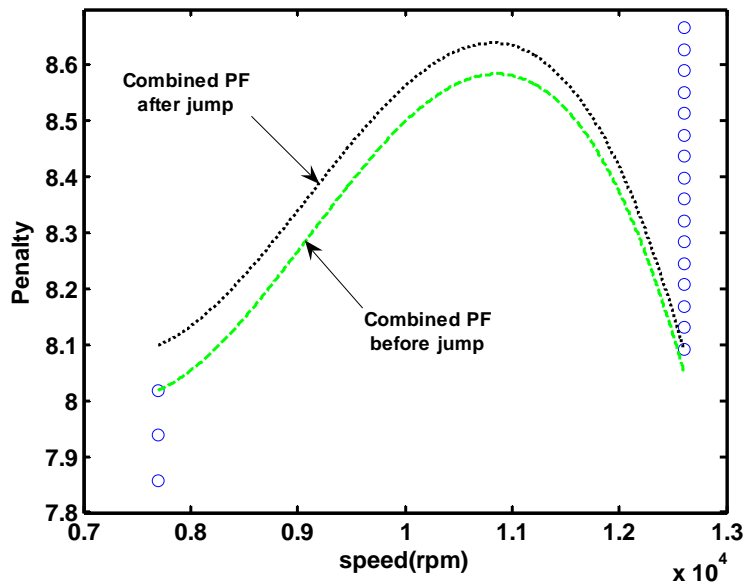


Figure 47: Combined penalty functions immediately before and after NIS<sub>0</sub> speed jump

Figure 47 shows the entire speed range of the NIS (7.7 to 12.6krpm), but zooms in on the penalty range for NIS<sub>0</sub> (penalties of 7.9 to 8.7). The circles represent different penalty values in NIS<sub>0</sub> and the green dashed line and black dotted line represent the combined penalty functions immediately before and after the speed jump, respectively. The different combined penalty functions have the same minimum point until reaching the value of  $\mu_{CO}$  immediately before the jump (green dashed line). When  $\mu_{CO}$  is incremented to the value that causes the discontinuity, the combined penalty function changes its shape from the green line to the dotted black line. This change in shape shifts the minimum point from 7.7krpm to 12.6krpm, creating the observed discontinuities.

In an actual clinical setting, the single outlier speeds at 7.7krpm and 12.6krpm are not practical pump speeds to include in the NIS. The pump must operate at the constant speed of 7.7krpm or 12.6krpm to remain in the NIS; if the speed varies slightly it will no longer operate in the NIS. Also, these speeds correspond to a small range of weights, and it will be difficult for the clinicians to make such small adjustments to the weights. Therefore, in a practical sense the NIS should not include these outliers. The set of pump speeds that does not include outlier points occurring at a single speed will be referred to as the clinical noninferior set, or CNIS. For

the example in Fig. 45, the CNIS is considered to be the continuous range of speeds 8.4krpm to 10.2krpm. The CNIS represents the speeds that a clinician should select from.

Each line in Fig. 46 is finite in length because the weights must sum to unity. For a fixed  $\mu_{AP}$ ,  $\mu_{LAP}$  and  $\mu_{CO}$  are limited to values between zero and  $1-\mu_{AP}$ , limiting the range of noninferior speeds. To illustrate this concept consider  $NIS_{0.2}$ . The highest value  $\mu_{LAP}$  or  $\mu_{CO}$  can be assigned is 0.8, forcing the other weight to be zero. Fig. 48 shows the penalty values for the noninferior range of speeds of  $NIS_{0.2}$  with the combined penalty functions produced by  $\mu_{CO} = 0.8$  and  $\mu_{LAP} = 0$  and vice-versa. The minima of the combined penalty functions for each case correspond to minimum and maximum penalty value in  $NIS_{0.2}$ . The two combined penalty functions create a limit of 8.5 – 10.04krpm on the speed choices.

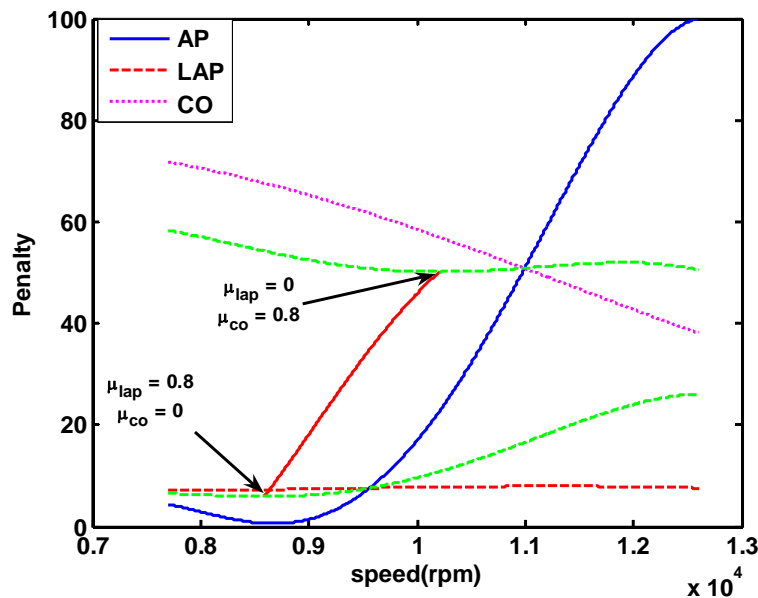
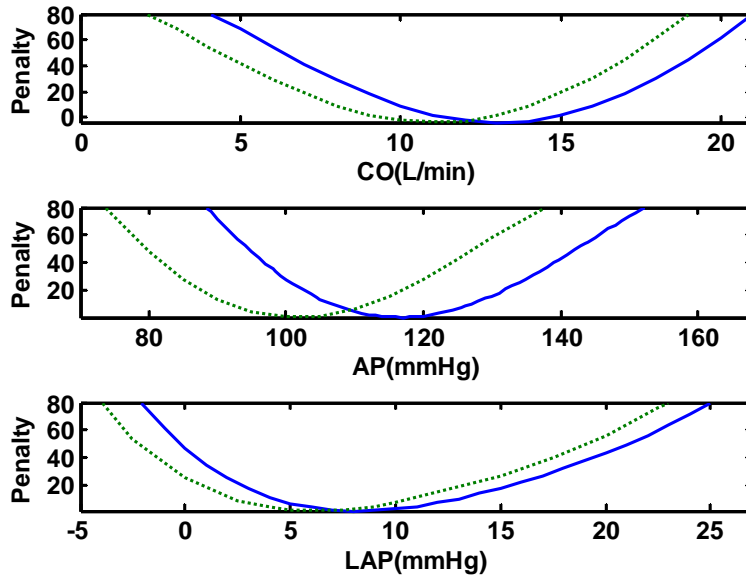


Figure 48: Example of finite size of speed values for  $NIS_{0.2}$

### 4.3 EFFECTS OF SHIFTING PENALTY FUNCTIONS

A shift in the  $J(\omega)$  penalty functions is the result of a change in hemodynamic set points. The original hemodynamic penalty functions in Fig. 37 have set points of  $CO = 11L/min$ ,  $AP = 100mmHg$ , and  $LAP = 5mmHg$ . Changing a set point shifts the minima of a penalty function to

the new set point, consequently shifting the  $J(\omega)$  penalty functions. Fig. 49 shows an example of shifted hemodynamic penalty functions (green dotted lines) with set points of  $CO = 13L/min$ ,  $AP = 115mmHg$ , and  $LAP = 7mmHg$ . The solid blue and dotted green lines in Fig. 49 represent the shifted and original hemodynamic penalty functions, respectively.



**Figure 49: Original and Hemodynamic penalty functions for CO, AP, and LAP set points of 13L/min, 115mmHg, and 7mmHg, respectively**

The penalty functions as functions of pump speed and CNIS for the original and shifted hemodynamic penalty functions in Fig. 49 are shown in Fig. 50. The results from the original penalty functions are on the top and the shifted penalty functions are on the bottom of Fig. 50. Comparing the top and bottom plots in Fig. 50, increasing the AP set point from 110mmHg to 115mmHg shifts the  $J_{AP}$  minimum from 8600krpm to 10.1krpm. Increasing the CO set point shifted the  $J_{CO}$  curve up, changing the minimum penalty from 38 to 65. The minimum penalty for  $J_{CO}$  is at  $\omega = 12.7krpm$  for both cases. The speed that produces the minimum penalty for  $J_{LAP}$ ,  $\omega = 7.7krpm$ , also remains the same; however, the minimum penalty decreases from seven to 2.6. The CNIS, indicated by a dashed-line box in each plot of Fig. 50, shifts from a range of

8.4krpm to 10.2krpm to a new range of 1krpm to 1.109krpm. The range of speeds also shifted from the original 7.7krpm to 12.6krpm to a new range of 7.7krpm to 13.4krpm.

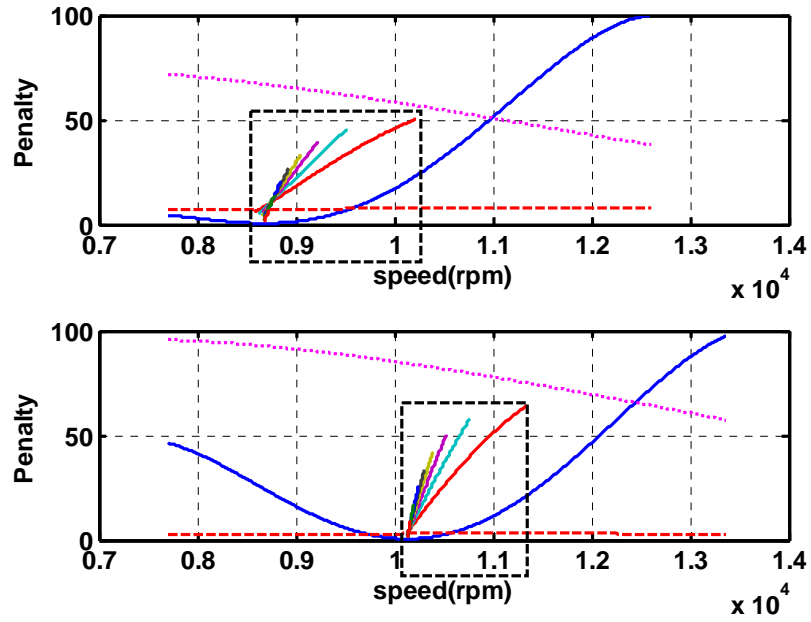


Figure 50: Original (top) and shifted (bottom) penalty functions and CNIS

## 5.0 CLINICIAN DECISION SUPPORT SYSTEM

The CNIS identifies a range of acceptable pump speeds, but the clinician still must select a specific speed within the set. One method of selecting a speed is the Analytical Hierarchy Process (AHP). AHP used the penalty functions to make “expert” comparisons between the three hemodynamic variables at different speeds. An advantage of AHP is that it utilizes clinician input to determine the importance of each hemodynamic variable. Clinician interaction is necessary to choose one pump speed out of a set of best pump speeds. However, it was determined that AHP was not a suitable method for this problem, as discussed in Appendix B.

The need to provide the clinician with assistance in choosing a pump speed motivated the development of a decision support system (DSS) to assist clinicians in choosing a pump speed and exploring the effects of speed on the three hemodynamic variables. The interface summarizes the research performed in this work and provides a convenient means to gain an understanding of trade-offs among penalty functions.

The clinician provides the DSS with set points for each of the three hemodynamic variables and can observe the effects the set points have on the best choice of pump speeds. The clinician can also specify a set of weights and observe each individual penalty function as a function of speed as well as the combined penalty function created from the specified weights. By allowing the clinician to adjust the  $\mu_i$  and view the combined penalty functions the GUI also acts as a tool to familiarize the clinician with the trade-offs of the penalty functions and choosing weights to determine a pump speed.

Fig. 51 shows the graphical user interface (GUI) of the DSS upon startup. The three boxes in the top right corner allow the clinician to enter the desired CO, AP, and LAP set points. This region is indicated by the label “Enter Physiological Set points.” The default set points (displayed upon startup) are CO = 11L/min, AP = 100mmHg, and LAP = 5mmHg. These values were chosen



because they are the set points of the original hemodynamic penalty functions provided by the team of clinicians [3]. The values provided by the clinician simply shift the original penalty functions to the desired set point.

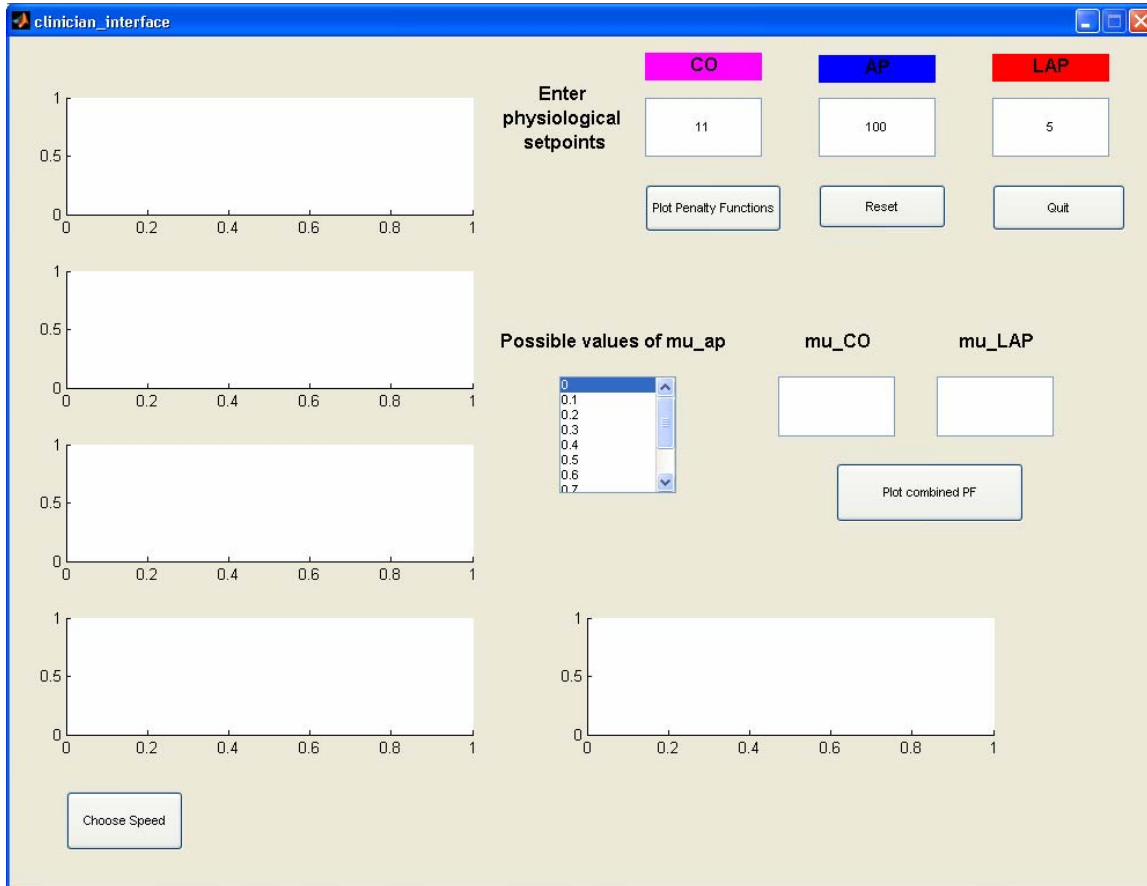


**Figure 51: GUI upon startup**

After entering the desired set points and pressing the “Plot Penalty Functions” button, the physiological data and individual penalty functions obtained using the procedures described in Chapter four are displayed on the four plot windows on the left side of the GUI, as shown on Fig. 52. In the example in Fig. 52 the set points are changed to CO = 13 L/min, AP = 115mmHg, and LAP = 7mmHg, the same set points of the shifted hemodynamic penalty functions in Fig. 49.

On each of the four plots, the range of the CNIS is indicated by two vertical black bars. The CNIS range in Fig. 52 is 1krpm to 1.1krpm, which matches the range seen in the lower plot of Fig. 50. The shape of the individual penalty functions in the lower left plot window also match the shape of the penalty functions in the lower plot in Fig. 50

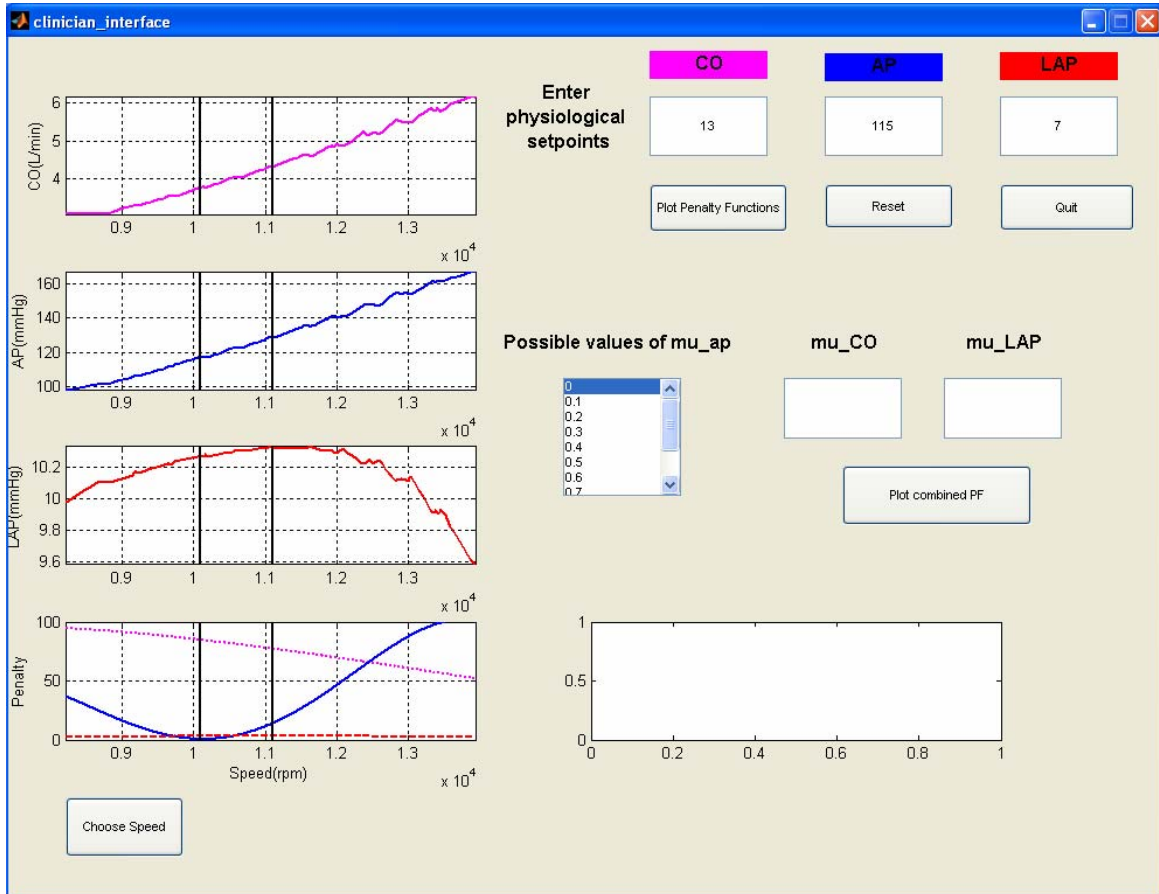


**Figure 52: GUI after changing set points and plotting penalty functions**

After plotting the data and penalty functions, the clinician can immediately enter the weights or choose a speed. A speed is chosen by pressing the “Choose Speed” button in the lower left corner of figures 51 or 52 and clicking the desired speed on the horizontal axis on any of the four plots. Once a speed is chosen, it is displayed to the right of the “Choose Speed” button, and a vertical dotted line is drawn at the speed chosen on each of the four plots.

The GUI was designed to limit the possible values of  $\mu_{AP}$  to  $\mu_{AP} = 0, 0.1, \dots, 1$ . The highest possible value of  $\mu_{AP}$  is one because the three weights must sum to unity. The increments of  $\mu_{AP}$  were chosen because it provides the clinician with a reasonable number of weight values to choose from for a given speed while providing a clear understanding how the penalty varies with speed.

The entire range of  $\mu_{AP}$  is not available at all speeds; for example, at a speed of 1krpm in Fig. 45, only  $\mu_{AP} = 0.1$  and  $\mu_{AP} = 0.2$  have CNIS points. No other values of  $\mu_{AP}$  are possible because at higher values of  $\mu_{AP}$  1krpm is no longer an optimal speed. The feasible set of  $\mu_{AP}$  values is communicated to the user using the “Possible Values of mu\_ap” list box on figures 51 or 52. By default, all possible values of  $\mu_{AP}$  are listed if the clinician does not want to select a speed but only wants to enter weights. After selecting the speed the list box is updated to reflect the feasible values of  $\mu_{AP}$ .

Regardless of whether or not a speed was chosen, a  $\mu_{AP}$  can be chosen from the list box, and values for the other weights entered in the boxes immediately to the right of the list box. Once the desired weights are provided, pressing the “Plot Combined PF” button displays the combined penalty function produced by Eq 21 using the provided weights and individual penalty functions displayed on the bottom left of the GUI. The speed is also indicated by a vertical dotted line.

Figure 53 continues the example from figure 52 by selecting a speed and choosing the weight parameters. As indicated by the label next to the “choose speed” button on Fig. 53 the selected speed is 10189.6rpm and is indicated on all plots on the GUI by the dotted black line. Also note that at 10189.6rpm the only feasible values of  $\mu_{AP}$  are 0.1, 0.2, ..., 0.8, as indicated by the list box. After choosing  $\mu_{AP} = 0.8$  from the box, weights of  $\mu_{CO} = 0.1$  and  $\mu_{LAP} = 0.1$  were entered in their respective text boxes. The resulting combined penalty function, shown beneath the weight text boxes, closely resembles  $J_{AP}(\omega)$  due to the high value chosen for  $\mu_{AP}$ .

In the previous example, the penalty functions as functions of speed are produced by shifting the original hemodynamic penalty functions along their horizontal axes. The drawback of this method is that the shape of the penalty functions cannot be changed, only the set point. It is possible that a clinician may decide that the optimal penalty function for a patient requires modification to the shape of the hemodynamic penalty functions, not just a shift in the set point. If the shape of the penalty functions must be changed it is necessary to modify the code that fits

the hemodynamic penalty functions to the clinician specified break points. No other modification is necessary; after fitting the new penalty functions, the DSS can be operated as usual.

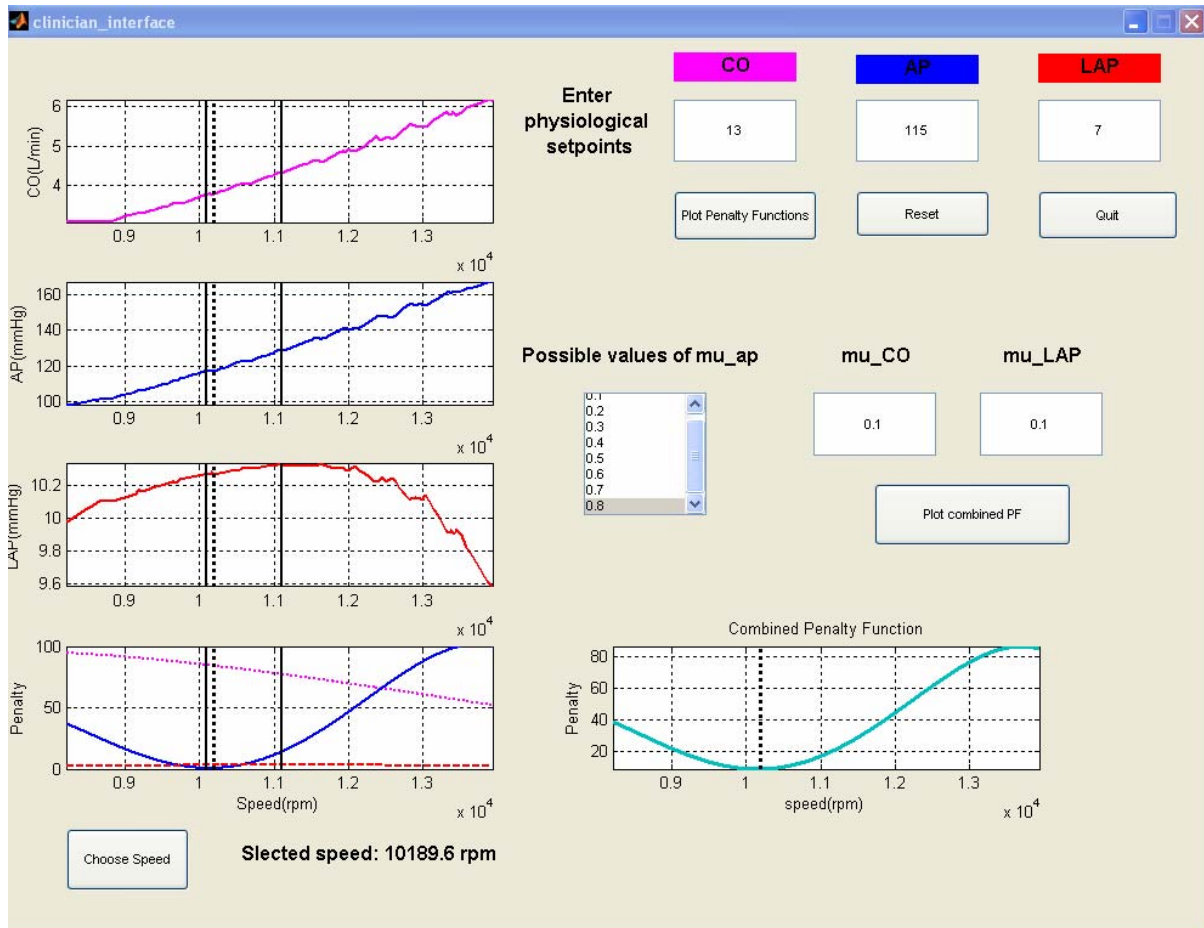


**Figure 53: GUI example from Fig. 52 after selecting a speed and choosing weights**

The user has several options as to his/her next course of action. The combined penalty function plot can be changed by choosing a new  $\mu_{AP}$  from the list box or entering a new  $\mu_{CO}$  or  $\mu_{LAP}$ . A new speed can also be selected, which in turn updates the list box and clears the text boxes. If new physiological set points are desired, the “Reset” button will clear all fields and return them to their default settings, as seen in Fig. 51. Finally, if the user is satisfied with the results, the “Quit” button can be pressed to end the program.

## 6.0 DISCUSSION

In this section the simulation results of the arbitrary penalty functions will be discussed. The NIS will be interpreted and clinical uses described. Reasons for properties of the NIS discovered during testing will be presented. Finally, the limitations and drawbacks of using the NIS method to select the best pump speed are discussed.

### 6.1 PENALTY FUNCTION AND NIS SIMULATIONS

Figures 31-34 illustrated the effects of shifting the penalty functions on the NIS. The NIS shifted along with the minima of the penalty functions but always spanned the range between the two most distant minima of the penalty functions. The magnitude of the penalty changes as the set points of the penalty functions are shifted, but the speed range is always between the two most distant minima.

In all of the simulations performed,  $\mu_3$  was held constant while  $\mu_1$  and  $\mu_2$  varied based on the value of  $\mu_3$ . Consequently, the speed ranges of the subsets  $NIS_{\mu_3}$  for increasing values of  $\mu_3$  decreased until containing only one value, the minimum of  $J_3$ , when  $\mu_3 = 1$ . Each subset has a finite length ranging from  $\mu_1 = 1 - \mu_3, \mu_2 = 0$  to  $\mu_2 = 1 - \mu_3, \mu_1 = 0$ . The reduced speed range is a result of the increased weight on  $J_3$ . A similar effect can be observed if instead of holding  $\mu_3$  constant,  $\mu_1$  or  $\mu_2$  is held constant.

The simulations using multiple continuous, convex penalty functions confirmed Zadeh's results [30] by providing a continuous NIS. However, introducing a discontinuity or non-convexity changes the behavior of the non-inferior set.  $NIS_0$  was still a continuous set of speeds between the minima of  $J_1$  and  $J_2$  due to  $J_3$  dropping out of Eq 8. For values of  $\mu_3 > 0$ , the

different  $NIS_{\mu_3}$  subsets contained a jump or region where points in  $NIS_{\mu_3}$  do not exist. Small increments of  $\mu_1$  and  $\mu_2$  were tested, but no points were found in this region.

The jump is caused by the increase in penalty introduced by the non-convexity (see figures 35 and 36). The non-convexity causes  $J_3$  to no longer increase or decrease in penalty monotonically with increasing or decreasing values of  $x$ . Consequently, the NIS is not continuous, because the discontinuous/non-convex region creates an increase in penalty for a small range of speeds. It should be noted that although a discontinuity exists in the NIS, the NIS still spans the range between the minima of the penalty functions. In the case of a discontinuous/non-convex penalty function with multiple local minima, the absolute minimum will be one of the NIS limits.

The simulations confirmed that three convex penalty functions produced a continuous NIS that spanned the range of the two most distant minima. It was also shown that it is possible to have a discontinuous NIS if the three penalty functions were not convex, continuous functions. The discontinuous NIS had a jump in some region where NIS points did not exist. Although in simulation only one non-convex penalty function was used, it is believed that the simulation results can be extended to two non-convex penalty functions. Because the simulation results are similar to the discontinuous NIS obtained using the penalty functions as functions of speed, it is concluded that it is reasonable to obtain a discontinuous NIS.

## 6.2 HEMODYNAMIC AND $J(\omega)$ PENALTY FUNCTIONS

The three original hemodynamic penalty functions (Fig. 37) were obtained using several clinician-specified break points and a fourth-order polynomial fit. All testing using penalty functions other than the original three was performed using a shifted copy of the original three. The penalty functions were not redefined for different set points.

The hemodynamic penalty functions were convex and continuous for the purpose of formulating the problem as a vector-valued minimization problem [30]. However, evaluating the hemodynamic penalty functions using the model data resulted in two of the three  $J(\omega)$  penalty functions being non-convex. The only convex function was  $J_{AP}$ . The  $J(\omega)$  penalty functions

were also not smooth, containing small non-convexities as described in Appendix A (also see Fig. 42).

The shape of the penalty functions is a result of the data obtained from the model. The convex nature of  $J_{AP}$  is a result of the AP data increasing from a value below the hemodynamic set point (decreasing penalty), and continuing to increase past the set point (increasing penalty). The monotonically decreasing CO penalty function is a result of the CO data increasing monotonically from a value below its set point, and it never reached the set point. The LAP data was nearly constant, resulting in a nearly constant penalty function.

### 6.3 NONINFERIOR SET

As expected, the NIS determined using the original penalty functions included speeds in the 7.7 to 12.6krpm range, which are the two most distant minima. Similar to the penalty function simulations, a higher density of speeds can be found around the  $J_{AP}$  minimum for increasing values of  $\mu_{AP}$ . This is a result of the combined penalty function  $J$  changing its shape to reflect a higher weight on  $J_{AP}$ . As  $\mu_{AP}$  increases, the shape of  $J$  more closely resembles the shape of  $J_{AP}$ . Therefore, when  $\mu_{AP} = 1$ , Eq. 21 reduces to  $J = J_{AP}$ . Minimizing this combined penalty function results in the minimum of  $J_{AP}$ , and because the only feasible values of  $\mu_{CO}$  and  $\mu_{LAP}$  are zero, the only speed in the NIS for  $\mu_{AP} = 1.0$  is the minimum of  $J_{AP}$ .

An unexpected result in the NIS testing was the two discontinuous regions (see Fig. 46). The discontinuities are a result of two of the three penalty functions being non-convex. The smallest increments allowable in Matlab were made to the weight parameters and no NIS points were found in the discontinuous region. This leads to the conclusion that the NIS (for the original hemodynamic penalty functions) is the disjoint set of speeds  $\omega = \{7.7\text{krpm}, 8.4 - 10.2\text{krpm}, 12.6\text{krpm}\}$ .

The two extreme points, 7.7krpm and 12.6krpm, are expected to be part of the NIS. When  $\mu_{LAP} = 1$ , Eq. 21 reduces to  $J = J_{LAP}$ , producing a NIS point at the minimum of  $J_{LAP}$ , which is  $\omega = 7.7\text{krpm}$ . It was expected that each set of weights would produce a unique speed, but  $\omega = 7.7\text{krpm}$  is a NIS point for any  $\mu_{LAP} > 0.985$ . This is a result of the concave shape of  $J_{LAP}$  (see

Fig. 44). As the speed increases, the penalty on LAP increases, causing the NIS to stay at the minimum of  $J_{LAP}$  until enough weight is removed from LAP (i.e.  $\mu_{LAP} < 0.985$ ). The speed then jumps to  $\omega = 12.6\text{krpm}$ , where a NIS point exists for different combinations of weights. This case occurs when little or no weight is given to  $J_{AP}$  ( $\mu_{AP} \leq 0.1$ ) reducing the problem to the minimization of  $J_{LAP}$  and  $J_{CO}$  for a given  $\mu_{LAP}$  and  $\mu_{CO}$ . Because the penalties for  $J_{CO}$  are higher than  $J_{LAP}$ , and  $J_{LAP}$  is nearly a constant value, the problem can further be approximated as minimizing only  $J_{CO}$  (for  $\mu_{LAP} < 0.985$ ). Consequently, for  $\mu_{AP} = 0$  and  $\mu_{LAP} < 0.985$  the NIS points will always be at  $\omega = 12.6\text{krpm}$ , the minimum of  $J_{CO}$ .

The disjoint set was the motivation for identifying the Clinician's Noninferior Set (CNIS), the set of speeds  $\omega = 8.4 - 10.2\text{krpm}$ . It was found in chapter 4.3 that although  $\omega = 7.7\text{krpm}$  and  $\omega = 12.6\text{krpm}$  are part of the NIS, they are optimal for a limited range of values of  $\mu_i$ . Also, the outliers exist at only two speeds;  $\omega = 7.7\text{krpm}$  and  $\omega = 12.6\text{krpm}$ . If the pump speed is set to either of these speeds any deviation from the chosen speed will cause the pump to operate in one of the boxed regions in Fig. 47. If the pump speed operates in one of the boxed regions it is no longer operating at a NIS speed. Therefore for practical reasons, the only range of speeds that should be considered by a clinician is the continuous region  $\omega = 8.4 - 10.2\text{krpm}$ .

When  $\mu_{AP} = 0.1$ , the repeated point still exists at  $\omega = 12.6\text{krpm}$ , but eventually jumps to the CNIS. The repeated points are caused by the reasons indicated above, but  $\mu_{AP} = 0.1$  provides enough weight on  $J_{AP}$  to draw the points to the CNIS.

As expected, shifting the set points of the original hemodynamic penalty functions also shifts the  $J(\omega)$  penalty functions, and consequently the NIS. An increase or decrease in the CO or LAP set point shifts  $J_{CO}$  or  $J_{LAP}$  up or down, respectively. As the AP set point is increased or decreased, the minimum of  $J_{AP}$  is shifted to a higher or lower speed, respectively.

In Fig. 45, the NIS speed ranges for increasing values of  $\mu_{AP}$  decreased and tended to cluster to the minimum of  $J_{AP}$ . The same behavior can be observed when the hemodynamic set points are changed; the NIS speed range shifts along with the minimum of  $J_{AP}$ . As the minima of  $J_{AP}$  and  $J_{CO}$  move farther apart, more values of  $\mu_{AP}$  produce a discontinuous region. The opposite effect is observed when they are moved closer, with the discontinuous region becoming smaller.



## 6.4 CLINICIAN DECISION SUPPORT SYSTEM

In chapter 5 a DSS was presented that allows a clinician to adjust hemodynamic set points and observe the effects of changing the pump speed and values for the  $\mu_i$ . The interface presents the clinician with the hemodynamic variable data, the penalty functions as functions of speed, the range of the CNIS, and the option to either select a speed or change the weights. Entering values for the weights allows the clinician to view the combined penalty function and the penalty incurred by a given pump speed.

An important aspect of the interface is the ability to set the values of the weights. The CNIS is not a complete solution to the pump speed selection problem. A range of pump speeds is provided and clinician input regarding the values of the weights is required before a single pump speed can be chosen. The interface assists the clinician with choosing the weights by allowing him/her to experiment with different weight combinations to observe how the speed changes and ultimately how it effects the patient.

Another advantage of the clinician interface is its usefulness as a training tool. Often, clinicians are not familiar with multiobjective optimization and NIS theory. It may be difficult for some clinicians to consider explicitly three constraints when choosing a pump speed and they may not have familiarity with a penalty function approach. By allowing the clinician to experiment with different speeds and weights, they can develop an understanding of how the theory applies to the pump speed selection problem. The interface allows them to gain experience using the NIS and how the weight values affect the pump speed.

## 6.5 SUMMARY

This work presented a method that can be used to determine an optimal pump speed using multiobjective optimization. By simultaneously minimizing convex penalty functions for AP, LAP, and CO, the NIS of best speeds can be determined. However it was found that the penalty functions as functions of speed were non-convex resulting in a NIS containing jumps. Simulations were performed to show that the jumps in pump speed were discontinuities and the NIS is a disjoint set of pump speeds.

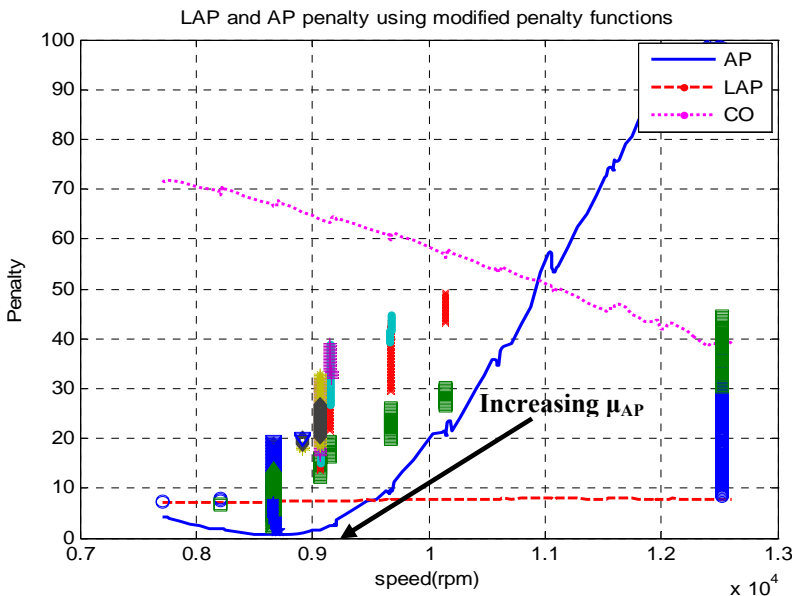
The NIS was narrowed down to the CNIS, providing a practical range of speeds for a clinician to choose from. By ignoring the outliers, the CNIS provides a reasonable range of speeds to choose from. Issues regarding operating the pump precisely at one of the outlier points to prevent operating outside of the NIS are avoided.

A DSS was developed to simplify the speed selection process by allowing the clinician to experiment with different speeds, weights, and set points to gain an understanding of their affect on the patient as well as become familiar with NIS theory. The DSS summarizes the research described in this thesis by starting with the penalty function set points, obtaining the necessary hemodynamic data to map the hemodynamic penalty functions to functions of speed, and finally providing the user with the CNIS. Essentially the DSS performs all of the steps outlined in Chapter Four.

## APPENDIX A

### EFFECTS OF NON-CONVEXITIES ON NIS

Before the penalty function polynomials were evaluated using the data from the model, the data were sorted and smoothed using a Matlab smoothing routine. However, the results still produced the unsmooth penalty functions in Fig. 54. Each of the different colored markers in Fig. 54 represent speeds in the NIS calculated for a given value of  $\mu_{AP}$ . For example, the green squares represent the members of the NIS that are the result of setting  $\mu_{AP} = 0.1$ . The value of  $\mu_{AP}$  for each marker is given in the table in Fig. 54.



$\mu_{AP}$	Marker
0	Blue circle
0.1	Green square
0.2	Red x
0.3	Light blue dot
0.4	Purple plus sign
0.5	Gold star
0.6	Black diamond
0.7	Blue downward triangle
0.8	Green upward triangle
0.9	Red left triangle
1.0	Filled blue star

**Figure 54: NIS of pump speeds using unsmooth penalty functions**

The NIS in Fig. 54 includes speeds in the range 7.7 to 12.5krpm, but there is approximately 500rpm between each point before they cluster around the minimum of  $J_{AP}$ . The cause of the small jumps in the NIS is non-convexities in the combined penalty functions created by the small dips in the penalty functions. A minimum is more likely to occur inside the small dip as opposed to a point nearby due to the dip producing a smaller penalty. Also, the discrete points in the NIS jump from one non-convexity to the next. This is similar to the phenomenon examined in the simulation performed in Fig. 36, where the penalty functions are continuous, but a jump in the NIS is caused by the non-convexity.

The arrow in Fig. 54 indicates the direction of increasing  $\mu_{AP}$  and  $\mu_{LAP}$ , and decreasing  $\mu_{CO}$ . As seen in the figure, as  $\mu_{AP}$  increases, the speeds in the NIS begin to cluster around the minimum of  $J_{AP}$  at 8.6krpm. Eventually, when  $\mu_{AP} = 1.0$ , the only possible speed is 8.6krpm, the minimum of  $J_{AP}$ .

Similarly, as  $\mu_{CO}$  increases (moves in the opposite direction of the arrow in Fig. 54), speeds in the NIS tend towards the minimum of  $J_{CO}$  at 12.5krpm. This is caused by the fact that increasing values of  $\mu_{CO}$  causes  $J$  to more closely resemble  $J_{CO}$ . Like the case for  $\mu_{AP}$ , when  $\mu_{CO} = 1.0$ , Eq. 21 reduces to  $J = J_{CO}$ , and finding the noninferior speed for this set of weights reduces to finding the minimum of  $J_{CO}$ .

As discussed in Section 3.2, to alleviate the issue of unsmooth penalty functions a least-squares polynomial fit was used. The results obtained from evaluating the hemodynamic penalty functions (Eqs 18-20) using the data obtained from the model simulation were used in the polynomial fit. The final penalty functions are shown in figure 44.

## **APPENDIX B**

### **ANALYTICAL HIERARCHY PROCESS (AHP)**

Another approach to finding an appropriate pump speed is the Analytical Hierarchy Process (AHP) [31, 32]. A review of the AHP process is provided, followed by the results of applying AHP to the physiological control problem. It was determined from the inconsistent comparisons that AHP is not suitable for this problem due to the nonlinear penalty functions used to make comparisons.

#### **B.1. OVERVIEW OF AHP**

Often, when making a decision among several alternatives, there are multiple criteria that must be taken into account. Similar to the penalty method, the different criteria affect the decision alternatives differently. One criterion may make an alternative more appealing while another criterion makes it look like a poor decision [31].

AHP is a method developed to aid in decision making with multiple criteria. AHP allows the user to break down the problem into smaller parts and arrange them in a hierarchy. The decision maker is only required to compare two elements at a time. After making all of the comparisons, AHP provides the decision maker with a ranked list of priorities, with the highest priority going to the decision that best satisfies the criteria.

The first step in AHP is to break down the problem into a hierarchy. The hierarchy for the pump speed selection problem is illustrated in Fig. 55. The top of the hierarchy is the objective or goal to be met, which in this case is to choose the best speed to operate the pump. The level below the objective consists of the specifications or criteria of the objective. In other words, this level lists what must be done to meet the overall goal, which is to minimize the penalty for CO, AP, and LAP. The bottom of the hierarchy lists the different decision alternatives that can be chosen to satisfy the overall goal. Here the decision alternatives are six arbitrarily chosen speed ranges that a pump speed can be selected from. Table 7 lists speed range choices that were selected by the author.

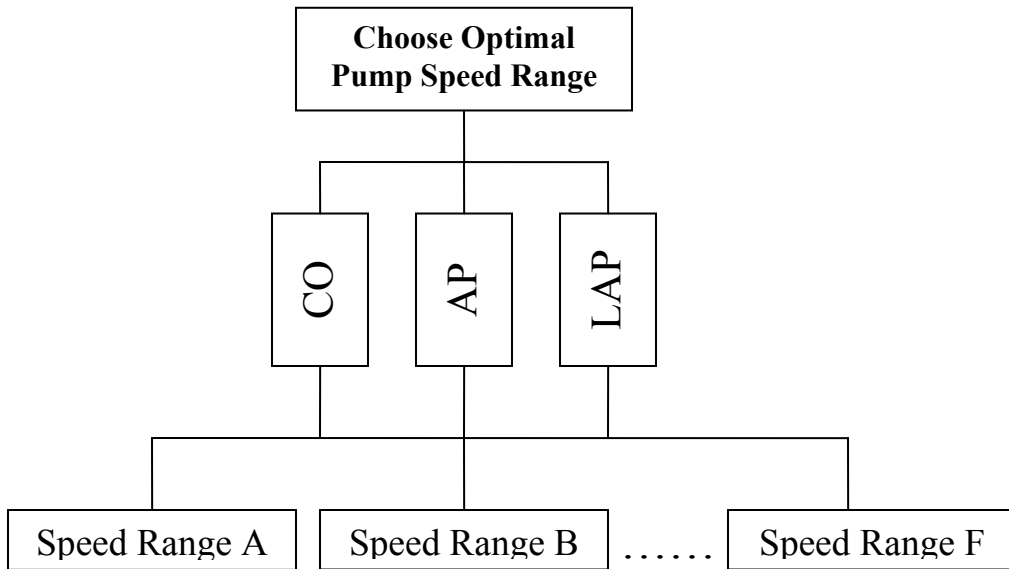


**Figure 55: Example of a hierarchy with n criteria and m decision alternatives**

**Table 7: Speed range alternatives**

Speed Range A	7-8krpm
Speed Range B	8-9krpm
Speed Range C	9-10krpm
Speed Range D	10-11krpm
Speed Range E	11-12krpm
Speed Range F	12-13krpm

It is important to note that in a hierarchy the elements in the level below must be comparable to each other with respect to each element in the preceding level. The purpose of the hierarchy is to compare all elements at a given level with respect to each element in the level above until the top level is reached and a final priority vector has been determined [31]. In the case of Fig. 56, each speed range can be compared with respect to its effects on the three hemodynamic variables, and the hemodynamic variables can be compared based on their relative importance.

After constructing the hierarchy, the next step is to make pairwise comparisons. All of the elements in the lowest level are compared based on their effects on each individual element in the level directly above. The comparisons are made in the form of a pairwise matrix, with each element in the second level receiving its own matrix. The comparisons are made using the rankings in Table 8 [31]. The “Penalty Difference” column was added to the table provided in [31] and will be described below.

**Table 8: Ranking system used in pairwise comparison matrices [31]**

<b>Magnitude of Importance</b>	<b>Qualitative Definition</b>	<b>Penalty Difference</b>
1	Equal Importance	< 1
2	Equal to moderate	1-10
3	Moderately more important	11-20
4	Moderate to essential	21-30
5	Essential importance	31-40
6	Essential to strong	41-50
7	Very strong importance	51-60
8	Very strong to extreme	61-70
9	Extremely important	71+

The pairwise matrices have reciprocal entries, because they have the property that entry  $a_{ji} = 1/a_{ij}$ . One reason for this property is it provides a unique, positive solution. It also makes intuitive sense due to the structure of the pairwise matrix. When making the comparison, the decision maker determines the dominance of the row entry over the column entry. If the row entry is more desirable, an integer value is entered depending on the degree of dominance. However, if the column entry is determined to be more desirable, that entry of the matrix is a

fraction, with the denominator being one of the integers from Table 8. When the comparison is reversed, i.e. comparing B to A instead of A to B, the reciprocal of the other comparison is entered. A value of one is given when comparing an alternative to itself. After comparing the decision alternatives with respect to the criteria in the level above, the criteria in the level above are compared to each other using the same procedure.

When using the penalties to determine the magnitude of importance, the penalty of the column entry is subtracted from the penalty of the row entry. A negative result implies a smaller penalty in the column entry making it more desirable. Therefore, the magnitude of importance integer corresponding to the penalty difference is assigned to the comparison. If the result is positive the row entry has a larger penalty, and the reciprocal of the corresponding magnitude of importance integer is assigned to the comparison.

Upon completing all of the comparisons, the next step is to determine a priority vector for each comparison made. The priority vector of a matrix ranks the importance of each alternative with respect to a given criterion, or, in the case of the criteria comparison matrix, which criteria is the most important. The priority vector can be approximated or determined using eigenvectors [31, 32]. It should also be noted that all priority vectors, regardless of the level of the hierarchy the comparisons are being made, must sum to one.

In this work the approximation method was chosen. The approximation method was selected because only three simple calculations are required, as opposed to finding the eigenvector of a matrix. The priority vector can be determined by normalizing the entries in each column of a matrix, i.e. calculating the sum of each column and dividing the entries of the column by its respective sum. The final step is to take the average across each row, resulting in the priority vector [32].

Finally, using all of the priority vectors, the global priority vector can be determined. The global priority vector is an  $nx1$  vector that provides the results of the process, which is a ranked list of the decision alternatives. First, define an  $nxm$  matrix  $\mathbf{P} = [\mathbf{PV}_1 \mathbf{PV}_2 \dots \mathbf{PV}_m]$ , where the  $\mathbf{PV}_i$  ( $i = 1, 2 \dots m$ ) are the  $nx1$  priority vectors for each of the  $m$  decision alternatives. To obtain the global priority vector, simply multiply  $\mathbf{P}$  by the priority vector of the criteria comparison. The values in the global priority vector are decimal values that indicate how well a given alternative meets the overall objective. Theoretically, the entry with the highest value is the best choice [31, 32].



After obtaining the global priority vector, the consistency of the comparisons must be examined. Whether or not the decision maker made consistent judgments throughout the comparison process has an impact on the global priority vector [32]. Inconsistent judgments lead to selection of a decision alternative that may not be the optimal choice. A feature of the AHP is the consistency ratio (CR), which is a measure of the consistency of the judgments [31, 32]. Similar to the priority vector calculations, CR can be calculated by determining the maximum eigenvalue  $\lambda_{\max}$ , or using an approximation of  $\lambda_{\max}$ . Because the approximation method was chosen to determine the priority vectors, the approximation method is also used here. The first step is to calculate a weighted sum vector, which is obtained by multiplying the comparison matrix by its priority vector and adding the columns. Next the entries of the weighted sum vector are divided by the respective entries of the priority vector, and  $\lambda_{\max}$  is obtained by calculating the average of these values [31].

The next step is to determine the consistency index (CI), which is defined as

$$CI = \frac{\lambda_{\max} - n}{n - 1} \quad (22)$$

where  $n$  is the number of items being compared. Finally, the CR can be calculated by dividing the CI by the random index (RI). The RI is a constant determined by the number of items being compared. Values of RI for different values of  $n$  are found in Table 9 [31, 32].

**Table 9: Values of RI for a given  $n$  [31, 32]**

<b>n</b>	<b>RI</b>
1	0.00
2	0.00
3	0.58
4	0.90
5	1.12
6	1.24
7	1.32
8	1.41

The consistency of the entire hierarchy can also be calculated by

$$CR_H = \frac{PV_2^T * CI_3}{PV_2^T * RI_n * \underline{1}} \quad (23)$$

where  $PV_2$  and  $CI_3$  are the priority vectors and consistency indices, respectively, for the speed comparison matrices.  $RI_n$  is a constant value from table 9.

If the CR is less than 0.10, the judgments are considered to be consistent and no revision is necessary. A value of CR greater than 0.10 indicates that it is likely there are inconsistencies in the judgments. If this occurs, the decision maker should consider making adjustments to the judgments made in the pairwise matrices. If this still does not improve consistency, it may be necessary to change the structure of the problem [31, 32].

## **B.2. RESULTS OF AHP**

The first step was to develop the pairwise comparison matrices using the average value of each hemodynamic variable produced by each speed range. Comparisons were made using the original hemodynamic penalty functions. The penalty for each speed range with respect to a given hemodynamic variable is assigned based on the penalty of the variable within the speed range. Because a range of speeds produces a range of variable values, the value that produces the lowest penalty in the range was used. The data used to determine the average values can be found in Fig. 42 of the results section. Table 10 provides the ranges of values of the hemodynamic variables in each speed range.

**Table 10: Data used to create pairwise comparison matrices**

	AP (mmHg)	LAP (mmHg)	CO (L/min)
<b>Speed Range A</b>	90-98	10.02-10.05	2.735-2.827
<b>Speed Range B</b>	98-105	10.05-10.14	.827-3.214
<b>Speed Range C</b>	105-117	10.14-10.27	3.214-3.74
<b>Speed Range D</b>	117-128	10.27-10.33	3.214-4.303
<b>Speed Range E</b>	128-140	10.33-10.3	4.303-4.894
<b>Speed Range F</b>	140-150	10.3-10.25	4.894-5.153

Table 11 shows the pairwise comparison matrix for the three hemodynamic variables. Entries in this matrix, like the selection of  $\mu_i$ , are made at the discretion of the clinician. In the case of Table 11, values were chosen arbitrarily. A property of the priority vector is that, again similar to the three  $\mu_i$  weights, the entries must sum to one. According to the priority vector in Table 11, the most important variable is CO.

**Table 11: Hemodynamic variable comparison matrix**

<b>Selection Criteria</b>	CO	LAP	AP	Priority Vector
CO	1	5	6	0.7066
LAP	1/5	1	3	0.2013
AP	1/6	1/3	1	0.0921

Tables 12 and 13 show the pairwise comparison matrices for each of the speed ranges in table 7 with respect to CO and AP, respectively. The LAP comparison is not included because it is a matrix of ones. This is due to the fact that the LAP data has such a small change between the different speed ranges that the penalty difference is less than one. The priority vector for each

case is also provided in the last column of each table. According to the priority vectors, the speed range that best meets CO and AP requirements is speed range B.

**Table 12: CO comparison matrix**

CO	Speed Range A	Speed Range B	Speed Range C	Speed Range D	Speed Range E	Speed Range F	Priority Vector
Speed Range A	1	1/2	¼	1/5	1/7	1/8	0.2527
Speed Range B	2	1	1/3	¼	1/6	1/7	0.4134
Speed Range C	4	3	1	1/3	1/4	1/5	0.0303
Speed Range D	5	4	3	1	1/3	1/4	0.0498
Speed Range E	7	6	4	3	1	1/2	0.0945
Speed Range F	8	7	5	4	2	1	0.1594

**Table 13: AP comparison matrix**

AP	Speed Range A	Speed Range B	Speed Range C	Speed Range D	Speed Range E	Speed Range F	Priority Vector
Speed Range A	1	1/3	2	7	9	9	0.2400
Speed Range B	3	1	3	8	9	9	0.3971
Speed Range C	1/2	1/3	1	7	9	9	0.1967
Speed Range D	1/7	1/8	1/7	1	8	9	0.0971
Speed Range E	1/9	1/9	1/9	1/8	1	7	0.0479
Speed Range F	1/9	1/9	1/9	1/9	1/7	1	0.0212

The final step is to determine the global priority vector. This is obtained by multiplying the matrix of the priority vectors of the speed range comparisons with the priority vector obtained from comparing the three hemodynamic variables. The calculation is shown below.

$$\begin{bmatrix} 0.0324 & 0.2400 & 0.1667 \\ 0.0468 & 0.3971 & 0.1667 \\ 0.0923 & 0.1967 & 0.1667 \\ 0.1507 & 0.0971 & 0.1667 \\ 0.2761 & 0.0479 & 0.1667 \\ 0.4017 & 0.0212 & 0.1667 \end{bmatrix} * \begin{bmatrix} 0.7066 \\ 0.2013 \\ 0.0921 \end{bmatrix} = \begin{bmatrix} 0.0866 \\ 0.1284 \\ 0.1201 \\ 0.1414 \\ 0.2201 \\ 0.3034 \end{bmatrix} \quad (24)$$

The first entry in the global priority vector is speed range A, the second is speed range B, up to speed range F. The global priority vector obtained here indicates that using the set of hemodynamic weights in the criteria priority vector, the best speed range is speed range F, 12krpm to 13krpm.

The final step of AHP was to determine the consistency of the comparisons made, or the CR. In this work, because there are six decision alternatives (speed ranges),  $n = 6$ , and from table 9  $RI = 1.24$ . Note that the second level of the hierarchy, the hemodynamic variables, has only three items being compared, so  $n = 3$  and  $RI = 0.58$ . After calculating the CI for each of the four comparison matrices using Eq 22, each CI was divided by the proper RI to provide the CRs shown in Table 14. The  $CR_{criteria}$  entry corresponds to the comparisons made in Table 11 and  $CR_H$  is the consistency of the entire hierarchy. According to Table 14 the consistency for AP is at an unacceptable level and the overall hierarchy consistency is slightly above the suggested maximum CR of 0.1.

**Table 14: CR for each pairwise comparison matrix**

$CR_{criteria}$	0.046
$CR_{CO}$	0.046
$CR_{LAP}$	0.000
$CO_{AP}$	0.265
$CR_H$	0.1058

To improve the consistency of the AP comparisons, the AP penalty function was assumed to be monotonically increasing instead of the convex shape seen in Fig. 45. Modifying only the speed comparison matrix for AP and using the hemodynamic variable comparisons in Table 11, the new values of CR are shown in table 15. Assuming the linear AP penalty function, all CRs are at acceptable values.

**Table 15: CRs for using linear AP penalty function**

$CR_{\text{criteria}}$	0.046
$CR_{\text{CO}}$	0.046
$CR_{\text{LAP}}$	0.000
$CR_{\text{AP}}$	0.0995
$CR_{\text{H}}$	0.0408

### **B.3 DISCUSSION OF AHP RESULTS**

An unexpected result encountered with AHP is that its results disagree with the NIS results. The two methods always gave consistent results when either CO or AP was heavily weighted. This drove the NIS point corresponding to weights using the hemodynamic priority vector entries close to the minimum of CO or AP, which lay in speed ranges F and B, respectively. If the weights were distributed more evenly, the NIS point corresponding to  $\mu$  values using the priority vector entries fell in the range of the CNIS, and changed as expected as the priority vector changed. Conversely, the AHP suggestion was speed range B or F regardless of changes made to the hemodynamic priority vector.

Another unexpected result was the high CR for AP. The convex shape of  $J_{\text{AP}}$  caused the unacceptable CR. When comparing the speed ranges with respect to AP, speed ranges A and C had higher penalties than speed range B. The operations performed using AHP are all linear, so the conclusion was reached that because the penalty function are nonlinear, i.e. monotonically increasing or decreasing, AHP produces results that are inconsistent.

## BIBLIOGRAPHY

- [1] Marieb, Elaine, *Human Anatomy and Physiology*. San Francisco, CA: Pearson Education, 1994.
- [2] Silverthorn, Dee Unglaub, *Human Physiology: An integrated approach, 2<sup>nd</sup> Edition*. Benjamin-Cummings Publishing Company, 2000.
- [3] J. R. Boston, J. F. Antaki, and M.A. Simaan, "Hierarchical Control of Heart-Assist Devices," *IEEE Robotics & Automation Magazine*. Vol. 10, pp. 54 - 64, 2003
- [4] Darryl Breitenstein, "Electric Analog Models of the Cardiovascular System," Master of Science thesis, Dept. Elect. Eng., Univ. of Pittsburgh, Pittsburgh, PA, 1992.
- [5] Berne, Robert M. and Levy, Matthew N., *Cardiovascular Physiology: Seventh Edition*. St. Louis, MO: Mosby-Year Book, Inc., 1997.
- [6] <http://www.cvphysiology.com/Heart%20Disease/HD002.htm>
- [7] [http://www.anaesthesiamcq.com/downloads/pv\\_loop.pdf](http://www.anaesthesiamcq.com/downloads/pv_loop.pdf)
- [8] Yih-Choung Yu, J.R. Boston, M.A. Simaan, J.F. Antaki, "Estimation of systemic vascular bed parameters for artificial heart control," *IEEE Trans. Automat. Contr.*, vol. 43, pp. 765 – 778, 1998.
- [9] T. Kitamura, K. Matsuda, and H. Akashi, "Adaptive Control Technique for Artificial Hearts," *IEEE Trans. Biomedical Engineering*, vol. BME-33, pp. 839 - 844, 1986.
- [10] K. Djabella, C. Medigue, and M. Sorine, "A Differential Model of the Baroreflex Control of the Cardiovascular System During a Tilt Test," *44<sup>th</sup> IEEE Conf. Processor. Decisions and Control*. December 12-15, 2005.
- [11] Reeve, E.B., and Arthur C. Guyton, Physical Bases of Circulatory Transport: Regulation and Exchange, "Long-Term Regulation of the Circulation: Interrelationships with Body Fluid Volumes by Arthur C. Guyton and Thomas G. Coleman," Philadelphia, W.B. Saunders Company, 1967, pp. 179-201

- [12] A.S. Ferreira, J.B. Filho, M.N. Souza, "Comparison of Segmental Arterial Compliance Determined With Three and Four Element Windkessel Models," *Engineering in Medicine and Biology Society Proc. 25th Annual International Conference of the IEEE*, vol. 4, pp. 3161 – 3164, 2003.
- [13] N. Stergiopoulos, B.E. Westerhof, J.-J. Meister, N. Westerhof, "The Four Element Windkessel Model," *Engineering in Medicine and Biology Society Proc. 18th Annual International Conference of the IEEE*, vol. 4, pp. 1715 – 1716, 1996.
- [14] D.S. Berger and J.K.-J. Li, "Temporal relationship between left ventricular and Arterial System Elastances," *IEEE Trans. Biomed. Eng.*, vol. 39, pp. 404 – 410, 1992.
- [15] B.C. McInnis, Z.-W. Guo, Pe Chien Lu, and J.-C. Wang, "Adaptive Control of Left Ventricular Bypass Assist Devices," *IEEE Transactions on automatic control*, Vol. AC-30, pp. 322-329, 1985.
- [16] M. Ursino, M. Antonucci, and E. Belardinelli, "Role of Active Changes in Venous Capacity by the Carotid Baroreflex: Analysis With a Mathematical Model," *Am. J. Physiol. 267(Heart Circ. Physiol. 36)*, pp. H2531-H2546, 1994.
- [17] G. Avanzolini, P. Barbini, A. Cappello, et. al, "Electrical Analogs for Monitoring Vascular Properties in Artificial Heart Studies," *IEEE Trans. Biomedical Engineering*, vol. 36, no. 4, pp. 462-470, April 1989.
- [18] W. Welkowitz, and J. K.-J. Li, "Control Aspects of Intraaortic Balloon Pumping: An Overview," *Proc IEEE*, VOL. 76, PP 1210-1217, 1988.
- [19] Goldstein, Daniel and Oz, Mehmet, *Cardiac Assist Devices*. Armonk, NY: Futura Publishing Company, Inc, 1999.
- [20] J.M. Ahn, J.H. Lee, S.W. Choi, W.E. Kim, Y.S. Omn, S.K. Park, W.G. Kim, J.R. Roh, and B.G. Min, "Implantable Control, Telemetry, and Solar Energy System in the Moving Actuator Type Toatl Artificial Heart," *Artif. Organs*, vol. 22, pp. 250-259, 1998.
- [21] H. Schima, W. Trubel, A. Moritz, G. Wieselthaler, H.G. Stohr, H. Thoma, U. Losert, and E. Wolner, "Noninvasive Monitoring of Rotary Blood Pumps: Necessity, Possibilities, and Limitations," *Artif. Organs*, vol. 6, ppp. 195-202, 1992.
- [22] Zhengyou Zhang, "Extended Kalman Filter,"  
<<http://www-sop.inria.fr/robotvis/personnel/z Zhang/Publis/Tutorial-Estim/node16.html>>
- [23] Yih-Choung Yu; J.R. Boston, M.A. Simaan, J.F. Antaki, "Sensitivity analysis of cardiovascular models for minimally invasive estimation of systemic vascular parameters," *American Control Conference proc.*, vol. 5, pp. 3392 – 3396, 1999.



- [24] Yih-Choung Yu; J.R. Boston, M.A. Simaan, J.F. Antaki, "Control Issues in Rotary Heart Assist Devices," *American Control Conference proc.*, vol. 5, pp. 3473 – 3477, 2000.
- [25] Yih-Choung Yu; J.R. Boston, M.A. Simaan, J.F. Antaki, "Intelligent Control Design for Heart Assist Devices," *Intl. Symposium Intelligent Control (ISIC) proc.*, pp. 497 – 502, 1998.
- [26] L.A. Baloa, J.R. Boston, M.A. Simaan, "A Certainty-Weighted Decision Model for the Detection of Suction in VADs," *Control Applications Proc. of IEEE Intl. Conference*, pp. 696 – 701, 2001.
- [27] L.A. Baloa, J.R. Boston, M.A. Simaan, "Performance of an Extended Certainty-Weighted Detection Model," *Systems, Man and Cybernetics IEEE Trans.* vol. 33, pp. 12 – 22, 2003.
- [28] Seongjin Choi, "Modeling and Control of Left Ventricular Assist System," PhD thesis, Dept. Elect. Eng., Univ. of Pittsburgh, Pittsburgh, PA, 1998.
- [29] <http://www.furthereducationlessontrader.co.uk/health>
- [30] Zadeh, L. A., "Optimality and Non-Scalar-Valued Performance Criteria," *IEEE Trans. On Automatic Control*, 1963, pp. 59-60
- [31] Saaty, Thomas L, "Priority Setting in Complex Problems," *IEEE Trans. On Engineering Management*, 1983, Vol. EM-30, pp. 140-155.
- [32] Anderson, David, Sweeney, Dennis, and Williams, Thomas, "*Quantitative Methods for Business, Third Edition*," New York, NY: West Publishing Company, 1980.
- [33] Saaty, Thomas, "How to Make a Decision: The Analytic Hierarchy Process," *Interfaces*, 6 November – December 24, pp. 19-43.
- [34] Butler, K. C., Development of an Innovative Ventricular Assist System, (Technical Proposal, Pittsburgh, PA: Nimbus Inc. in collaboration with University of Pittsburgh, 1994, unpublished).
- [35] Baloa, Leonardo, "Certainty-Weighted System for the Detection of Suction in Ventricular Assist Devices," Ph.D. thesis, Dept. Elect. Eng., Univ. of Pittsburgh, Pittsburgh, PA, 2001.
- [36] Chong, Edwin and Zak, Stanislaw, *An Introduction to Optimization, second edition*, New York, NY: John Wiley & Sons, Inc, 2001.
- [37] Matlab v7, The Math Works, 1994-2007
- [38] National Kidney foundation, <http://www.kidney.org/atoz/atozItem.cfm?id=158>